CARDIFF UNIVERSITY

Conductivity Studies of Single Protein Molecules

by

Athraa J Zaki

A thesis submitted in partial fulfillment for the
degree of Doctor of Philosophy

in the
College of Physical Sciences and Engineering
School of Physics and Astronomy

October 2016

Declaration of Authorship

This work has not been submitted in substance for any other degree or award at this or any other university or place of learning, nor is being submitted concurrently in candidature for any degree or other award.

Signed ....(candidate) Date ....

STATEMENT 1: This thesis is being submitted in partial fulfillment of the requirements for the degree of PhD.

Signed ....(candidate) Date ....

STATEMENT 2: This thesis is the result of my own independent work/investigation, except where otherwise stated, and the thesis has not been edited by a third party beyond what is permitted by Cardiff University's Policy on the Use of Third Party Editors by Research Degree Students. Other sources are acknowledged by explicit references. The views expressed are my own.

Signed ....(candidate) Date ....

STATEMENT 3: I hereby give consent for my thesis, if accepted, to be available online in the University's Open Access repository and for inter-library loan, and for the title and summary to be made available to outside organisations.

Signed ....(candidate) Date ....

STATEMENT 4: I hereby give consent for my thesis, if accepted, to be available online in the University's Open Access repository and for inter-library loans after expiry of a bar on access previously approved by the Academic Standards and Quality Committee.

Signed ....(candidate) Date ....

“Love and Do What You Like.”

Saint Augustine

Abstract

A fundamental step for future uses of biomolecules in electronics is the study of the bonding, orientation and conductance of a single molecule attached to a conductive substrate, which is the building block of electronic materials and devices based on molecular conduction. This work provides an in-depth examination of morphology and electrical properties of different molecules anchored to Au(111) and to sustainable carbon materials (graphite and graphene). Cytochrome b_{562} (Cyt b_{562}), TEM beta-lactamase and the superfolded green fluorescent protein engineered with phenyl azide were exposed to UV irradiation to transform the azide compound into the nitrene radical, which enabled successful molecule linking to graphene. The UV-based approach was tested on the above molecules to ascertain its robustness against the specificity of the protein used. The efficiency of the procedure was inspected by imaging via atomic force microscopy (AFM) and scanning tunnelling microscopy (STM). By repeated sample preparation and imaging, we established suitable protein concentrations to enable single-molecule measurements on the resulting samples (e.g., the concentration range optimal for cyt b_{562} on gold was 0.025-0.5 μM). We used a home-built environmental cell in combination with STM to study the conductance of differently engineered cyt b_{562} proteins on Au(111), as well as the conductance of oligothiophene on gold, under different humidity and temperature conditions. We found that the conductance of cyt b_{562} is smaller at lower relative humidity and further decreased when also temperature is reduced. Measuring the conductance as a function of the tip-substrate distance in both tip approaching and retracting modes revealed the occurrence of hysteresis. The engineered cyt b_{562} with two thiols in the long axis led to less hysteresis in the conductance and larger protein height on gold (from AFM) compared to the protein with thiols in the short axis. Our results stress the importance of protein engineering to control the electrical properties of functionalized surfaces. This study meets the growing demand for achieving more efficient molecule linking to conductive substrates, and studying environmental effects on the electrical response of functionalized surfaces (which is relevant, e.g., to sensing applications).

Acknowledgements

I wish to thank in a special way my supervisors Dr. Martin Elliott, Prof. Emyr Macdonald and Dr. Dafydd Jones for their invaluable guidance, supervision and support throughout the period of my research. I also thank them for their human support over the years of my stay in Cardiff.

A very special thank to Dr. Andriy Moskalenko, who has helped me and guided me throughout my work. A big thank to the group at the School of Bioscience for preparing all the engineered protein samples. A big thank to the group at Liverpool University for providing the oligothiophene samples. A great thank to Dr. Agostino Migliore for useful discussions and advices.

I would like to thank Mr. Rob Tucker and Mr. Andrew Harrison from the electronic workshop for providing the electronics for the environmental cell. Big thanks go to the mechanical workshop for their work on the environmental cell chambers. A big thank to all the staff of the School of Physics and Astronomy at Cardiff University. I would like to express my gratitude to the Kurdistan Regional Government and Ministry of Higher education in Kurdistan Region of Iraq for their indispensable sponsoring and financial support.

I would like to express my gratitude to my friends from the Nanophysics group, for the very friendly environment that they offered to me. I remember all your encouraging words in difficult times and all of the shared happy moments. I will always remember them: Rangeen, Adam, Isam, Watheq, Ellis and Suzan: thanks to all of you! Also, I would like to thank my friends in the Bioscience group: Sam, Andrew, Adam, Harley and Raphael. A great thank to all of my friends in Cardiff and London and in St. Peters Parish in Cardiff. A big and special thank goes to Dr. Luqman Dosky for his help. A big and special thank goes to my dear friends Naseem Salim and Wassfi Sulaiman, for all their help and human support. A big thank to my dear friends in Dahuk and Erbil, and especially Ligia, Sirod, Zahra, Sania, Sheren, Dhabiyaa, Maha, Rana, Wassan, Dr. Shamil and family, Mr. Khalid and Mrs Karema. A big thank to all friends at Zakho University.

A very special thank to my Family in Iraq: baba Jaji, mamma Amena, Raed, Raeda, Haifaa, Rabii, Fadi, Fidaa, Rawaa, Hana and Rita, all of my brothers and sisters in law and my lovely nephews. I appreciated so much your great help and support in all ways despite your hard situation. I love you all! Another very special thank to my family in Italy: babbo Michele, mamma Caterina and Leonardo: thanks a lot for everything, I love you all! Finally, the greatest thanks go to the person who enlightened my life since I met him, Agostino. Thank you for your love, support, patience. Without you I would not have overcome all the difficult times, and without you I would not have enjoyed the happy times the same. Love you forever.

List of Publications

1. Andrew M. Hartley, Athraa J Zaki, Adam R. McGarrity, Cecile Robert-Ansart, Andriy V. Moskalenko, Gareth F. Jones, Monica F. Craciun, Saverio Russo, Martin Elliott, J Emyr Macdonald, and D. Dafydd Jones. Functional modulation and directed assembly of an enzyme through designed non-natural post-translation modification. Chem. Sci., 2015, 6, 3712-3717.
2. Athraa J Zaki, Andrew M Hartley, Samuel C Reddington, Andriy Moskalenko, Monica F Craciun, J Emyr Macdonald, D Dafydd Jones, and Martin Elliott. Defined covalent assembly of protein molecules on graphene using a genetically encoded photochemical reaction handle, in preparation.
3. Athraa J Zaki, Andriy Moskalenko, Samuel C Reddington, J Emyr Macdonald, D Dafydd Jones, and Martin Elliott. Cyt b_{562} Conductance under different environmental conditions, in preparation.
4. Athraa J Zaki, Andriy Moskalenko, Andrew M Hartley, Samuel C Reddington, J Emyr Macdonald, D Dafydd Jones, and Martin Elliott. Study of single protein molecules on graphite, in preparation.

Contents

List of Figures

List of Tables

Abbreviations

SPMs	Scanning probe Microscopies
AFM	Atomic Force Microscopy
STM	Scanning Tunnelling Microscopy
SAMs	Self-assembled monolayers
ET	Electron transfer
Cyt $\mathbf{b}_{562}$	Cytochrome b_{562}
sfGFP	Superfolder Green Fluorescent protein
HOPG	Highly ordered pyrolytic graphite
SH-LA	Long axis variant of cytochrome b_{562} .
SH-SA	Short axis variant of cytochrome b_{562}
$\mathbf{G}_0$	Conductance quantum
PKA	protein kinase A
azF	p-azido-L-phenylalanine
SPAAC	strain-promoted azide-alkyne cycloaddition
CUAAC	Copper-promoted azide-alkyne cycloaddition
DBCO	dibenzylcyclooctyne
I-z	Current versus distance
z	Vertical displacement (of probe tip)
RH	Relative humidity
DNA	Deoxyribonucleic acid
RNA	Ribonucleic acid

I would like to dedicate this thesis to: Agostino, My family, My best friends.

Chapter 1

Introduction

1.1 Introduction to Molecular Elctronics

This study aims to describe the structure, morphology and conductive properties of electrode surfaces functionalised with biomolecules, under different environmental (namely, humidity and temperature) conditions, using scanning probe microscopies (SPMs) such as atomic force microscopy (AFM) and scanning tunnelling microscopy (STM). This work offers a large body of measurements and pertinent analysis that range from the visualization of functionalized surfaces to the characterization of the conduction through single biomolecules of different types adsorbed on diverse substrates such as Au(111) and sustainable carbon materials (graphite and graphene). The mentioned imaging techniques also provided information about our successful implementation of a strategy based on matter-radiation interaction that enables efficient adsorption of different classes of molecules on graphene.

Despite many discouraging attempts to fabricate molecular devices with stable and reproducible behaviour along the lines of standard electronics, recent years have witnessed a renewed and widespread interest in the subject of this work and, more generally, in the scientific investigation at the nanometre scale, where quantum effects play an evident role and nature organizes biological functions at a molecular level. In fact, growing research areas define the evolution of Nanoscience in directions that go well beyond the expectations at its early stages and that have significant implications on technological development, and thus on the quality of our life. These research areas include but are not limited to: Nanometre scale electronic components, such as, molecular switches [7, 8]. Organic materials and devices for solar energy harvesting [9–11] and optoelectronics [12, 13]. Strategies to harness electrons produced and consumed by enzymatic reactions at the chemically modified electrodes of enzymatic (or microbial) biofuel cells [14]. Chemical sensing [15–17] and signalling (with particular interest in devices that translate biological signaling into typical electronic signaling [18]. Spintronics [19, 20]. Information processing and quantum computing [13, 21]. Functionalized materials for biomedical electronics , including cell-chip connections, cyborg cells [22], and prosthetics.

Technological development in these branches of modern science still demands wide investigation of structural dynamics, charge and energy conduction at organic/inorganic interfaces. In fact, biology offers a broad variety of efficient functional molecules and molecular materials. The biological function critically depends on charge transfer reactions and their connections to molecular topology, sequence of atomic groups (such as the amino acids in proteins), and structural dynamics. The rich conductive properties of molecules can be exploited for the fabrication of electronic devices at the nanometre scale [23]. However, the functions of single molecules and molecular assemblies may be far from being guaranteed and optimized in the contexts of technological application. In addition, the contact of molecules with solid-state materials impose chemical and physical constraints that need to be explored (especially in terms of structural stability and interfacial charge transfer) in order to design working functional materials and devices.

The state of art of the substantially redefined and broadened field of molecular electronics (which, in fact, combines features that pertain to biophysics, biochemistry, chemistry of materials, energy and environmental sciences, biomedicine, quantum information and computing) emphasizes the need for novel ways and strategies to implement molecular-operation devices. To achieve this goal, we need (a) to explore ways to exploit the advantages of using single molecules with advanced and specific functionalities, rather than conventional inorganic materials of standard electronics; (b) but also to understand what kind and degree of stability should be demanded from molecular devices in relation to what molecular function is to be exploited.

Improving on the fabrication of devices with self-assembled monolayers (SAMs), apart from exploiting the propensity of molecules to self-assemble and the resulting polarization properties [21], has been seen as a solution to issues such as, e.g., the great variability in the conductance through single molecules [24]; but this solution should be pursued without losing the nanoscale operation and intrinsic functionalities of molecules compared to solid-state materials for standard electronics, that is the purpose of molecular electronic devices. Perhaps a solution to this problem consists in requiring only an appropriate statistical operation of a set of molecules rather than the systematic operation that is typical of standard microelectronics. At any rate, a fundamental step in this search for a working implementation scheme is studying the bonding, orientation and conduction of a single molecule on an electrode surface, which sets the limiting size (the building block) and the electrical behaviour of the basic unit of any molecule-based electronic material [25, 26].

Within the above general context, this study provides an in-depth examination of structural and conductive properties of the building block of molecular materials and devices: a single molecule attached to a conductive substrate. To achieve this goal, tests during the preparation of the samples, prior to our conduction measurements, aimed to obtain functionalized substrate surfaces with protein densities sufficiently low to enable tip-single molecule contact.

Redox proteins are good candidates for nanoelectronics by virtue of their charge transfer function in nature. Redox molecules are characterized by at least two different charging states (oxidation states) which are long-lived enough for their observation, and reversible transitions can occur between such oxidation states.

In the biological context, redox molecules participate in oxidation-reduction reactions, where a molecule is oxidized by losing an electron initially localized in its active site (redox center), while another molecule takes the electron and its redox center is thus reduced. In the molecular electronic context, an electrode can take an electron initially localized in the molecular redox center or supply an electron to this center. The properties of the redox molecule will generally depend on its oxidation state. Using redox molecules in nanoelectronics requires their contact with electrode materials. The firm anchoring of the proteins to the electrodes is a necessary condition to produce working devices. However, even when this condition is satisfied, electron transfer (ET) from proteins to electrodes is unnatural, and interposing a molecular species that acts as an ET mediator is sometimes the solution [14]. Small redox molecules in direct contact with the substrate may enable sufficiently efficient interfacial ET, but molecular motion and conformational changes that depend on the environmental conditions may strongly impair the efficiency of the charge conduction at the interface. Efficiency is clearly improved if the molecule can be suitably immobilized and oriented on the surface. This can be achieved by protein engineering, mutating the molecule at a specific position so as to enable site-specific immobilization on the support electrode [27–29]. However, in a molecular junction, the presence of two molecular anchoring sites is required to enable stable contacts to both electrodes, and this can be achieved by molecular engineering [4, 30]. In the STM setup, once the substrate electrode is functionalized with a protein molecule, due to the molecular motion, the tip might touch the protein in such a way not to bind to the other anchoring site. However, for example, considering the typical dimensions of gold tips and the capability of thiols to attach to Au(111), one may expect a good probability that the tip meets the second thiol group and gets attached to the molecule through this thiol, especially if the two thiol groups were located in opposite positions on the surface of the protein. Moreover, measuring the conduction through engineered double-mutant proteins with anchoring groups along different axes [30] is a valuable tool to investigate the optimal orientation of the molecule on the substrate in building molecular junctions. In fact, the extensive measurements of this research allowed us to clearly observe differences in the conductive properties of redox proteins doubly mutated along different (short and long) axes [30] (see chapter 5).

Cyt b_{562} is a small protein with a redox cofactor (which can therefore closely approach the surface of a substrate), has a relatively robust structure and is thus amenable to engineering without losing its native structure, and its ET properties can be coupled to other processes [31–33]. Based on the above discussion, all these properties make cyt b_{562} variants good candidates for bio-nano-electronic devices. In fact, engineered cyt b_{562} proteins were vastly studied in this work. However, our investigation was also extended to other biomolecules. In fact, the study of different molecules allowed us to investigate general aspects of anchoring techniques that can go beyond the specificity of the protein employed. In particular, in this research project we developed a method, based on UV irradiation, to attach proteins to graphene, and this method that was successfully applied to different proteins: cyt b_{562}, TEM beta-lactamases, and the superfolded green fluorescent protein (sfGFP). Linking proteins to graphene surfaces offers an attractive prospect for the development of molecular electronics, especially if the molecular linkers can be inserted at suitable positions of the proteins without affecting their functionality. Local charge rearrangement around the molecular anchoring point and electrostatic changes in the protein can be used to gate the electronic properties of the graphene material, with potential applications such as sensing at single-molecule resolution [34, 35].

Developing sensors, as well as other future nanoelectronic devices demand to understand the influence of environmental conditions on the electrical response of molecule-electrode interfaces. Studying the effect of changing temperature on the conductive properties of the adsorbed molecules is important because one expects that the bio-electronic device will be exposed to a thermal range during its life and operation. Considering that in nature biomolecules generally work in a solvated or at least humid environment, it is also important to find out the humidity level for the optimal operation of biomolecule-solid interfaces or, more generally (for example, in biological and environmental sensing applications) the influence of humidity on the conductive properties of biomolecule-electrode interfaces. This implies studies of the electrical conduction at such interfaces under different humidity conditions. A system for controlling low/high humidity during structural and electrical characterization of the functionalized surfaces is thus desirable, and this system was built in our laboratory (see below) and used in this work thesis.

1.2 Dissertation Outline

For all systems studied in this work, prior to conduction measurements we performed imaging of the proteins on the Au(111) or graphene substrates via AFM and STM, in order to ascertain the effectiveness of the protein anchoring and to explore the suitability of the functionalized surface for single-molecule electrical measurements. After that, we measured the current through protein-electrode interfaces in STM setup as a function of the distance between the tip and the substrate. These measurements were performed in air as well as under different conditions of temperature and humidity. To this purpose, a special system (environmental cell) was built in our laboratory. The use of the home-built STM inside the environmental cell enabled the control of the temperature and humidity during the experiments, and thus to study the effect of these parameters on the conductance of the STM junction. The different types of substrate and engineered proteins used in our investigations, and the functional groups used for protein anchoring to the substrate are summarized in Table 1.1.

The thesis is organized as follows. Chapter 2 contains an introduction to the background theory useful to interpret the conduction measurements, and an overview of the protein systems used in this study and the reasons for their choice. Chapter 3 describes the scanning probe microscopy techniques and the environmental cell system used to carry out the imaging of the surfaces before and after the adsorption of the proteins, and the conductance measurements at different conditions of humidity and temperature. Chapter 4 describe the new approach (based on the use of the pyrene functional group and of UV irradiation) that was developed in this study for linking proteins to graphene surfaces. The linking was proved by

Proteins List			
Chapter	Substrate	Protein	Functional group
Chapter 4	HOPG	TEM105	Pyrene
	HOPG	sfGFP204	Pyrene
	HOPG	Cyt b_{562}	Pyrene
	HOPG	PKA	Pyrene
	Graphene	TEM105	Pyrene
	Graphene	TEM165	Pyrene
	Graphene	Cyt b_{562}	Short-linker pyrene
	Graphene	TEM105	azF
	Graphene	TEM165	azF
	Graphene	sfGFP204	azF
	Graphene	Cyt b_{562}	azF
Chapter 5	Au (111)	Cyt b_{562} holo SH-LA	Double thiols
	Au(111)	Cyt b_{562} holo SH-SA	Double thiols
	Au(111)	Cyt b_{562} apo SH-LA	Double thiols
	Au(111)	Cyt b_{562} apo D5C	Single thiol

Table 1.1: List of proteins used in this work

Raman and resistance measurements, and also demonstrated by imaging of the functionalized surfaces. Moreover, the chapter provides a first study of the UV effects on the conductance of proteins on graphene.

Chapter 5 presents a vast investigation of the electrical properties of different (and differently engineered) single cytochrome proteins on Au(111). The focus is on the study of the conductance as function of the tip-substrate distance under different environmental conditions, as obtained using the home-built environmental cell. The conductance of oligothiophene on Au(111) in ambient conditions, as under different conditions of humidity and temperature, is described in Chapter 6. Finally, Chapter 7 summarizes the main findings of this work and suggests future research aimed to its further development towards nanoelectronics applications.

As shown by the above table, we carried out measurements on a broad set of differently engineered molecules and molecule-substrate combinations. The experiments aimed to study the morphology and conductivity of the functionalized surfaces and were carried out under diverse conditions of tip-substrate distance (also inspecting the occurrence of hysteresis in the conductive response of the system for tip approach and retraction), temperature and humidity (which are physical parameters of clear relevance to the operation of biomolecular systems). We believe that our vast body of measurements and their analysis provide useful information on limitations and values of the rich biochemical, physical and engineering context offered by hybrid interfaces that involve redox biomolecules.

Chapter 2

Background Theory

Redox proteins and molecular wires are good candidates for the development of new electronics, by virtue of their charge transfer function in nature and (regarding redox molecules) because of their ability to operate in different charging states. Using these molecules in nanoelectronics requires their operation at the interface with electrode materials. In this context, it is important to understand how the redox centre can engage in ET with non-biological partners such as the tip and substrate of an STM setup, and how the ET steps are related to the observed conductance. In this chapter, we first introduce theoretical models for studying ET and charge transport at molecule-electrode interfaces. Then, we introduce the biomolecules used in this thesis and the reasons for their choice.

2.1 Marcus Electron Transfer Theory

In this section we will outline some fundamental concepts in the Marcus theory for homogeneous and heterogeneous ET. Homogeneous ET refers to the charge transfer between biological redox partners, which are both biomolecules. Heterogeneous ET refers to the charge transfer between an organic component (the molecule) and an inorganic component, such as a metal electrode. Nowadays, electrodes made of sustainable carbon materials (graphite, graphene, carbon nanotubes) are also used. Yet, the structural and conductive properties of these materials well distinguish them from the strong asymmetry and charge localization properties of (redox) molecules, thus leading again to the concept of heterogeneous ET.

2.1.1 Homogeneous Electron Transfer

Marcus expression for the ET rate constant is essentially a matter of energy balance in a redox system, and ultimately relies upon the simple consideration that electrons are much lighter than nuclei, thus being accordingly faster. This leads to the Born-Oppenheimer approximation that separates the motions of the electronic and nuclear degrees of freedom: nuclei can be seen as clamped in fixed positions in the time scale characteristic of electron motion; conversely, the electronic wave function is capable to adjust itself quasi-statically to the nuclear motion. As a consequence, while the atoms of a molecule move, at each nuclear configuration they see a well-defined electronic charge density (as given by the square modulus of the electronic wave function) which is at equilibrium with that nuclear configuration and that determines an effective potential energy for the same nuclear motion [36]. Hence, the energy of an electronic state can be defined and represented as a function of the nuclear coordinates, which allows us to draws diagrams such as those in Figures 2.1 and 2.3 (see below. In analytical terms, the electronic wave function is obtained at fixed nuclear coordinates, and then the corresponding energy works as an effective potential for the nuclear motion [36].

Consider two biological redox partners, that is, two biomolecules that engage in an ET reaction, one of which works as the electron donor and the other as the electron acceptor. At the simplest and most common level of approximation, one can use a single reaction (nuclear) coordinate to define the stage of the reaction, that is, the collective nuclear coordinate Q in Figure 2.1 When the electron is localized on the donor, the electronic energy as a function of Q, which is the effective potential energy for the nuclear motion, is represented by curve I in Figure 2.1

Here I stands for the initial localized or diabatic electronic state. Similarly, F represent the electronic energy as a function of Q for the final (after the transition) diabatic electronic state, with the charge on the acceptor biomolecule. Indeed, the I and F curves represent free energy profiles, since they also include an entropic contribution, and, under simplifying assumptions, they are two parabolas [37–41]. In this circumstance, one can set a simple expression for the ET activation free energy, which is the free energy that must be afforded in order for the ET reaction to occur (see Figure 2.1) and on which the ET rate constant depends exponentially [39]:

$$k = \kappa v e^{-\Delta G^{\ddagger}/k_B T} \tag{2.1}$$

where the activation free energy is

$$\Delta G^{\ddagger} = \frac{(\lambda + \Delta G^0)^2}{4\lambda} \tag{2.2}$$

In equation 2.1, κ is the electronic transmission coefficient, v is an effective frequency for the nuclear motion along the reaction coordinate, λ is the reorganization energy, and ΔG^0 is the reaction free energy. As anticipated above, the meaning of equation 2.1 can be easily understood in terms of energy balance. Before the ET, the system is in the electronic state I. A is system representative point in Figure 2.1, and Q $_0$(I) is the equilibrium collective nuclear coordinate of the system when the charge is localized in the donor (represented as a sphere with charge q=1 in suitable units in the left-top corner of Figure 2.2). At this coordinate, a polar environment (for example, surrounding water) would orient so as to achieve the minimum energy, which corresponds to the maximum negative electrostatic interaction energy. If the electronic charge could jump directly (that is, from the initial equilibrium nuclear coordinates) to the acceptor, it would occur on a timescale in which the environment could not rearrange (a vertical arrow represents this electronic state transition at fixed nuclear coordinate Q in Figure 2.1). The nuclear configuration would no longer be the most stable one, and the system energy would increase because of the charge transition (point B in Figure 2.1). Such a transition could happen only in the presence of an external energy source. For example, the energy could be supplied by the absorption of a photon. Then, the system would relax to the equilibrium configuration of state C, releasing a free energy that is the reorganization energy associated with the occurred charge transfer process. In the absence of an external energy source, this transition would violate energy conservation, and thus it cannot occur.

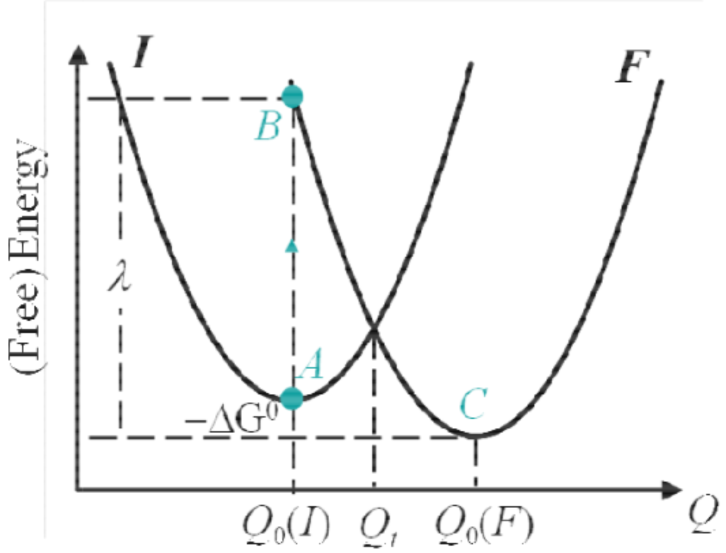

FIGURE 2.1: Free energy (or effective potential energy) profile for the initial (I) and final (F) localized (or diabatic) electronic stats of a typical ET reaction. Q is the nuclear reaction coordinate, and its equilibrium values in the two electronic states are indicate. Q_t is the transition state coordinate, corresponding to the lowest energy on the crossing seam surface. λ is the reorganization energy and ΔG^0 the reaction free energy. A denotes the initial state. B is an excited state with the electronic charge distributed as in the final electronic state, but nuclei still at the equilibrium coordinates of the initial electronic state. C is the final state, which can be achieved starting from B by release the reorganization energy. Starting from state A; state B could be achieved, e.g., by absorption of a photon. This is a vertical electronic transition with nuclei fixed at the equilibrium coordinates for the electronic state A, in accordance with the Franck-Condon principle. The (free) energy released by means of the nuclear rearrangements that lead from B to C is the reorganization energy.

Another forbidden transition is the one directly from state A to state C, because, as it is stated by the Franck-Condon principle and assumed in the Born-Oppenheimer approach, the nuclei are clamped in fixed positions during the electron transition. Therefore, where only thermal energy is available, the nuclear system needs to rearrange (step 1 in Figure 2.2) so as to achieve a configuration (the transition state coordinate Q_t) at which the initial and final electronic charge localizations have the same energy (namely, the two parabolas in Figure 2.1 cross each other). Step 2 of Figure 2.2 can take place between these two configurations, and then step 3 can occur by nuclear relaxation to the optimal geometry for minimizing the energy in the final electronic state. In Figure 2.1, this relaxation corresponds to a motion downhill on the F curve until the achievement of state C, and the released free energy is part of the reorganization energy.

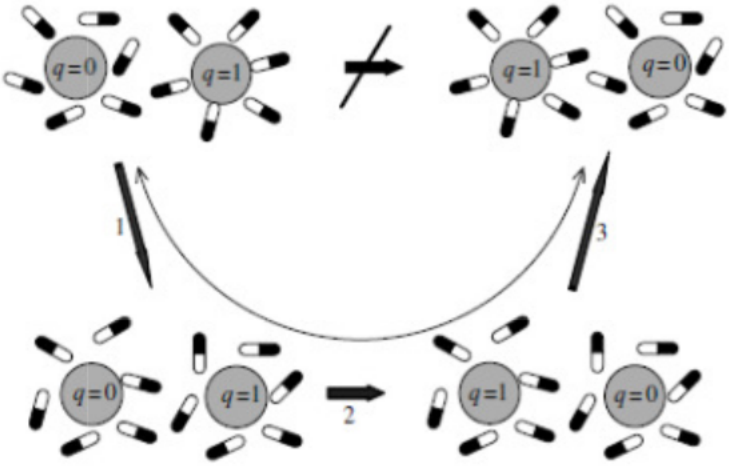

FIGURE 2.2: The Marcus picture of electron transfer reactions. The two upper diagrams describe the initial (left) and final (right) states of the reaction. The solvent is oriented so as to minimize the energy when the charge is localized on either the charge donor (initial state) or acceptor (final state). The direct transition between the two states is prohibited, because the solvent should simultaneously rearrange in the time scale of the electron transition. Instead, the reaction proceeds through step 1 (preparation of a suitable configuration of the nuclear environment for which the initial and final electronic states have the equal energy), step 2 (electron transfer while the nuclei remain at this given configuration), and step 3 (nuclei rearrange so as to minimize the energy of the system with the electron on the acceptor). Figure reprinted from ref. [1]. Copyright 2007 Oxford University Press.

The activation barrier for the ET is measured by the difference in energy between the initial state and the state at $Q = Q_t$ and correlates with the value of the reorganization energy, as analytically expressed by equation (2.2). It can be easily seen that the value of the reorganization energy is strictly related to the curvatures of the parabolas in Figure 2.1 [1, 42]. The larger the reorganization energy, the smaller the ET rate constant. In particular, for electron self-exchange (when donor and acceptor are molecules of the same type, so that the initial and final states are characterized by the same free energy), the reaction free energy is zero and the reorganization energy is the only determinant of the activation energy that appears in the ET rate constant.

The reorganization energy comprises an inner sphere contribution, which is associated with the redox centres and their ligands, and an outer sphere contribution that results from the reorganization of the surrounding environment. For example, for solvated redox proteins, the small redox cofactor essentially contributes to the inner-sphere reorganization energy, while the surrounding protein matrix and the solvent contribute to the outer-sphere reorganization energy. The solvent has an important role in determining the value of the latter. Clearly, following a charge transfer process, the solvent reorganization energy is much larger for a polar solvent than for an apolar one (where dipole moments can only be induced ones) and tends to zero as the density of the solvent is decreased in some way. Reducing the density of the solvent around a biomolecule has also the effect of changing its structural properties (since molecular folding is generally related to the presence of the solvent), thus determining a change in the protein contribution to the reorganization energy but also a different medium for the electron in the region between the donor and acceptor redox sites.

The change in the ET medium will affect the electronic coupling between the donor and acceptor, which is the other physical ingredient that enters the expression for the ET rate constant through the electronic transmission coefficient.

Equation 2.1 and Figure 2.1 do not show an important fact that occur around $Q = Q_t$. About this coordinate, the Born-Oppenheimer approximation does not hold, and the nuclear and electronic degrees of freedom cannot be decoupled. This circumstance removes the degeneracy of the I and F states at $Q = Q_t$ (avoided crossing), producing the (free) energy landscape in Figure 2.3. In this landscape, one can distinguish an adiabatic ground state and an adiabatic first excited state, which can be written as linear combinations of the diabatic states and have a minimum separation equal to double the effective electronic coupling or ET matrix element U_{IF} between states I and F.

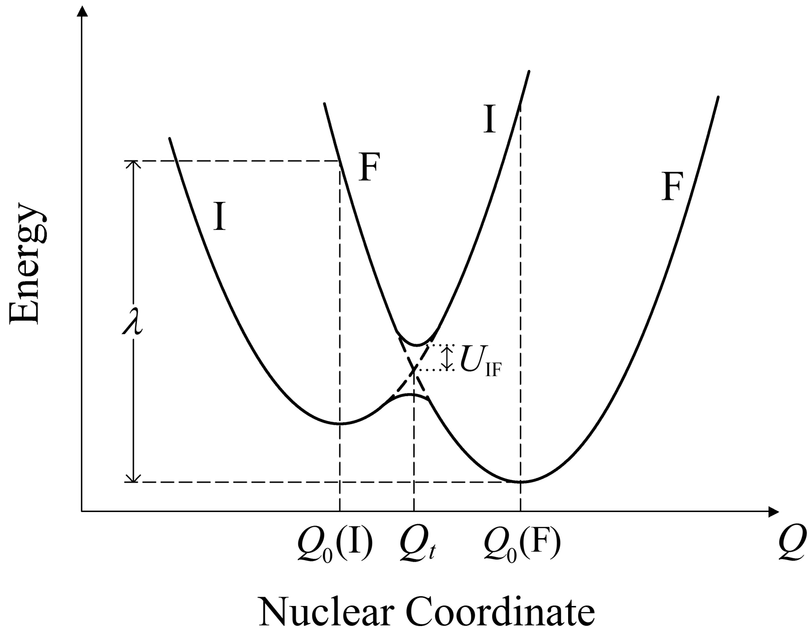

FIGURE 2.3: Free energy (or effective potential energy) profile for the initial (I) and final (F) electronic stats of a typical ET reaction, with introduction of the electronic coupling U_{IF} between the two electronic states. The diabatic states are represented by dashed lines, while the two adiabatic states that results from their linear combinations are represented by solid lines. The minimum splitting of the adiabatic state energies is $2U_{IF}$. Figure reprinted from ref. [2]. Copyright 2006 AIP Publishing.

Elaborating on the coupling of the electronic dynamics (as determined by U_{IF}) and of the nuclear dynamics around the avoided crossing, Landau and Zener [1, 38, 42, 43] elaborated an expression for the electronic transmission coefficient that depends on both V_{IF} and the nuclear motion, as characterized by the reorganization energy and the temperature. In the limit of suitably small [1, 38, 42] electronic coupling between donor and acceptor, which is typical of proteins, the Landau-Zener approach leads to an electronic transmission coefficient that is proportional to $|U_{IF}|^2$. Once the Landau-Zener analysis is combined with the Marcus free energy factor, the expression for the ET rate constant becomes [39]

$$k_{ET} = \sqrt{\frac{\pi}{\lambda k_B T}} \frac{|U_{IF}|^2}{\hbar} exp \left[-\frac{(\Delta G^0 + \lambda)^2}{4\lambda k_B T} \right] \tag{2.3}$$

The donor-acceptor electronic coupling is responsible for the electron tunnelling between the two redox centres once the nuclear coordinates rearrange so as to approach Q_t , but the expression for the electronic transmission coefficient in equation 2.3 results from the coupling of the tunnelling event with the nuclear dynamics at a given temperature, and in fact this coefficient contains not only $|U_{IF}|^2$ but also the nuclear reorganization energy and the temperature. As we will see below, the presence of $|U_{IF}|^2$, with its role in the electron tunnelling event, introduces an exponential dependence of the ET rate on the donor-acceptor distance.

2.1.2 Heterogeneous Electron Transfer at Molecule-Electrode Interfaces

When a redox molecule is adsorbed on a solid-state component such as a metal electrode, the ET rate constant for the interfacial ET process changes in some important ways. A main difference arise from the diverse electronic structures of molecules and metals or other conductive materials with periodic structure and a huge number of electronic levels available for conduction. A number (which is essentially infinite for a metal) of electronic states will be coupled to the molecular electronic state, and the availability of electrode electronic states for the ET with the molecule will depend on the direction of the ET, on the temperature and on the potential difference applied between electrode and molecule. Consider, for example, Figure 2.4. At zero temperature, all electronic energy levels in the metal until the Fermi level (μ , represented by a yellow dash in the figure) are occupied, while all levels above are empty. In fact, the occupancy of the electronic levels is described by a step-wise Fermi-Dirac distribution, which is represented by the green curve in Figure 2.4. If an occupied molecular level (blue dash) is below the metal Fermi level, the molecule cannot deliver the electron to the metal unless the temperature is raised (so that the distribution of level occupancy is described by the black curve and levels with non-zero probability of occupation are available at the energy of the electronic state localized on the molecule) and/or a metal-molecule potential difference is applied, so as to shift up the molecular level with respect to the metal levels.

Another important difference between homogeneous intermolecular ET and heterogeneous ET at a molecule-electrode interface lies in the reorganization energy associated with the ET process. While the localization of the excess charge in the molecule causes a suitable rearrangement of the surrounding nuclear environment (for example, solvent molecules will suitably orient their permanent electric dipole moments), the electronic charge is not spatially localized in the metal, where it spreads throughout (and it is immediately swept away under applied bias voltage) on a time scale fast relative to the atomic motion. The consequence is that only the molecular system contributes to the reorganization energy. To get a rough estimate of the resulting reorganization energy, one can consider that: (a) when two similar molecular redox centres are far enough from each other, their similar contributions to the reorganization energy are approximately additive; (b) one of the two molecules involved in the ET is replaced by the electrode in the interfacial process. Based on these two considerations, the reorganization energy associated for the ET is roughly half of that for the molecular electron self-exchange reaction [1].

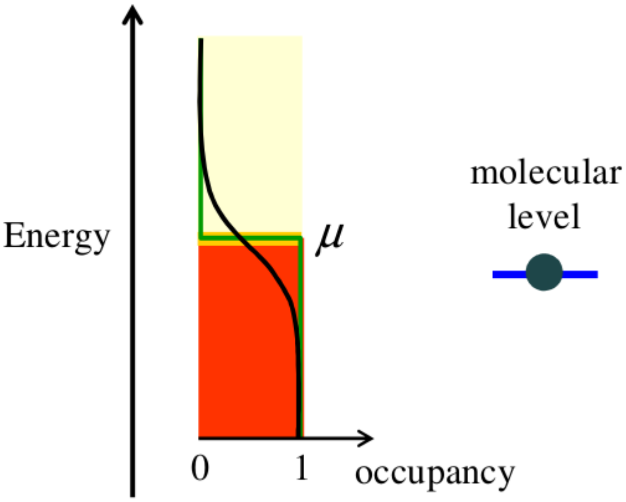

FIGURE 2.4: Representation of the energy bands, Fermi function and Fermi level (μ, dark yellow dash) in a metal (left), and the energy level of the molecular system that interacts with the metal. The green step function represents the Fermi function at zero temperature. The black curve is the Fermi function at nonzero temperature.

With the above differences in mind, the rate for the interfacial ET process is obtained by integrating the Marcus-like rate constant for an ET process (between the molecular level and a level in the metal) over the density of states in the electrode and the distribution of their occupancy: the Fermi distribution $f(\varepsilon)$ if the electron has to be delivered by an occupied level in the metal to the molecule; the complementary Fermi distribution 1-$f(\varepsilon)$ if the electron has to be transferred from the molecule to an empty metal level. The resulting expressions for the interfacial ET rate constants are [1, 44, 45].

$$k_{metal \rightarrow molecule}(V_{interface}) = \frac{1}{2\sqrt{\pi k_B T \lambda}} \int_{-\infty}^{\infty} d\varepsilon f(\varepsilon)\Gamma(\varepsilon) exp\left(-\frac{[\varepsilon - \lambda - \Delta E(V_{interface})]^2}{4\lambda k_B T}\right) \tag{2.4}$$

and

$$k_{molecule \to metal}(V_{interface}) = \frac{1}{2\sqrt{\pi k_B T \lambda}} \int_{-\infty}^{\infty} d\varepsilon [1 - f(\varepsilon)] \Gamma(\varepsilon) exp \left(- \frac{[\varepsilon + \lambda - \Delta E(V_{interface})]^2}{4 \lambda k_B T} \right) \tag{2.5}$$

In equations 2.4 and 2.5, λ is the reorganization energy associated with the (possibly solvated) molecular system. $f(\varepsilon)$ is the Fermi function describing the occupation probability of the single-electron state with energy ε :

$$f(\varepsilon) = \frac{1}{e^{\varepsilon - \varepsilon_F/(k_B T)} + 1} \tag{2.6}$$

$\Gamma(\varepsilon)$ is the metal-molecule coupling strength, which is proportional to the density of metal electronic states of energy ε, $\rho(\varepsilon)$, and to the average squared electronic coupling between such states and the electronic state localized in the molecule, $< |U_{metalmol}(\varepsilon)|^2 >$:

$$\Gamma(\varepsilon) = \frac{2\pi}{\hbar} < |U_{metalmol}(\varepsilon)|^2 > \rho(\varepsilon) \tag{2.7}$$

$\Delta E(V_{interface)})$ is the potential difference-dependent reaction (free) energy for the interfacial ET:

$$\Delta E(V) = E_{mol^-}(Q_{mol^-}) - [E_{mol}(Q_{mol}) + \mu - eV_{interface}] \tag{2.8}$$

where μ is the metal chemical potential relative to vacuum (the inverse of the metal work function), $E_{mol^-}(Q_{mol^-})$ is the (free) energy of the reduced molecule at its equilibrium nuclear coordinates Q_{mol^-}, $E_{mol}(Q_{mol})$ is the analogous quantity for the oxidized molecule at its equilibrium coordinates Q_{mol}, e is the elementary charge, and $V_{interface}$ is the potential difference between molecule and electrode.

If the (solvated) molecule is inserted between two electrodes, four ET rate constants are involved, as shown in Figure 2.5. For example, this is the case for a redox molecule inserted between the substrate and tip of an STM system. Under sufficiently high bias voltage only the forward ET rate constants (namely, the rate constants for ET in the preferential direction established by the sign of the voltage) are effective. Series expansions on analytical functions of the rates in equations 2.4 and 2.5 were recently provided [46–48]. Approximations to these series show [47] that the threshold interfacial potential differences for getting significant values of the forward ET rates, and thus for enabling the corresponding ET processes, are $\lambda + \Delta E(0) = \lambda + E_{mol^-}(Q_{mol^-}) - E_{mol}(Q_{mol}) - \mu$ for the metal-to-molecule ET and $\lambda - \Delta E(0)$ for the molecule-to-metal ET. In a molecular junction, the larger of these two values, that is, $\lambda + |\Delta E(0)|$ determines the minimum interfacial potential drops to get appreciable current through a molecular junction via charge hopping (see Section 2.4).

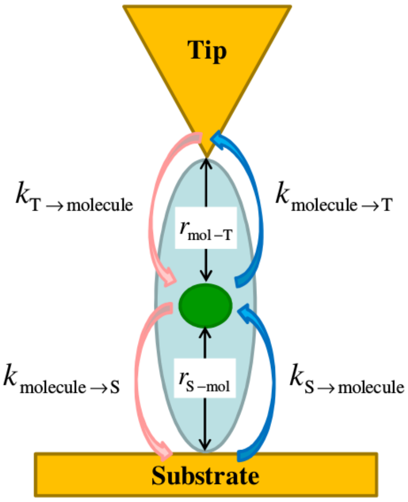

FIGURE 2.5: Molecular junction in STM setup. For brevity of notation, in the subscripts of the electron transfer rate constants, the substrate is denoted by S and the Tip by T. The redox centre of the molecule is represented as a green circle. The distances of this redox centre from S and T, as well as the pertinent ET rate constants are indicated. If a sufficiently high potential difference is applied between S and T, with higher potential at the tip, the forward ET rate constants (that is, the S-to-molecule and molecule-to-tip ET rates; ET jumps represented by blue arrows) determine the current in a charge hopping model of the junction conduction, while the backward ET processes (pink arrows) occur with negligible rates.

If the molecule per se is a monovalent cation, in the above expressions mol represents the cation and mol^- stands for the neutral species. The presence of polar solvent around the molecule stabilizes the molecular cation (and, in general, the charged molecular species). Therefore, if $E_{mol^-}(Q_{mol^-}) - [E_{mol}(Q_{mol}) + \mu] < 0$, the presence of the polar solvent will reduce $|\Delta E(0)|$, and hence $\lambda + |\Delta E(0)|$. In other words, in this case, the solvent will increase the junction current at a given bias voltage across the molecular bridge or at given voltage set point and tip-sample distance. Before concluding this section, let us notice that, assuming that $\rho(-\varepsilon) = \rho(\varepsilon)$ all around the metal Fermi level and that the states with the transferring electronic charge spread over the metal are similarly coupled to the state with charge localization around the molecular redox centre, one can simply write the interfacial ET rate constants as

$$k_{metal \to molecule}(V_{interface}) = |U_{metalmol}|^2 A(V_{interface}) exp\left[-\frac{\Delta E(V_{interface})}{K_B T}\right] \tag{2.9}$$

and

$$k_{moleculel \to metal}(V_{interface}) = |U_{metalmol}|^2 A(V_{interface}) \tag{2.10}$$

with

$$A(V_{interface}) = \sqrt{\frac{\pi}{\hbar^2 \lambda K_B T}} exp\left[\frac{\Delta E(V_{interface}) - \lambda/2}{2k_B T}\right]$$
$$\times \int_{-\infty}^{\infty} d\varepsilon \rho(\varepsilon) f(\varepsilon) exp\left(-\frac{[\varepsilon - \Delta E(V_{interface})]^2}{4\lambda k_B T} + \frac{\varepsilon}{2k_B T}\right) \tag{2.11}$$

The two ET rate constants satisfy the detailed balance principle and are proportional to the electronic coupling, which causes exponential decays of such rates with the distance of the molecular redox centre from the surface (see next section).

2.2 (Direct) Tunnelling and Resonant Tunnelling

(Quantum) Tunnelling occurs when a particle is found outside a confining potential that could not be surmounted classically. The electronic wave function does not vanish abruptly at a potential energy barrier higher than the electron quantum-mechanical average energy. If the met barrier is thin enough, the wave function, and thus the probability to find the electron on the other side of the barrier, is non zero. In general, the non-zero probability of tunnelling through a potential energy barrier can be explained in terms of the non-zero coupling of electronic states that, in a one- dimensional picture, are mainly localized on opposite sides of the barrier (for example, see Figure 2.6a). On the one hand, from analysis of the two-state dynamical problem in the short-time limit (in which the probability of reverse transitions is still negligible), one can show that the electron transmission coefficient or tunnelling probability is proportional to the square electronic coupling between the two electronic states [43, 49]. On the other hand, the Gamow approach [49] leads to an approximately exponential dependence of the tunnelling probability on the width of the barrier, with a decay factor of this probability that is determined by the height of the barrier relative to the energy of the incident particle. In fact, for a simple rectangular potential energy barrier of height U_0 and width a (Figure 2.6b), the tunnelling probability is approximately given by [43, 49].

$$\tau \approx exp\left[-\frac{2a}{\hbar}\sqrt{2m_e(U_0 - E)}\right] \tag{2.12}$$

In general, the transmission coefficient has, approximately, an exponential decay with the tunnelling distance and one can write

$$\tau \sim |U_{12}|^2 \sim exp(-\beta a) \tag{2.13}$$

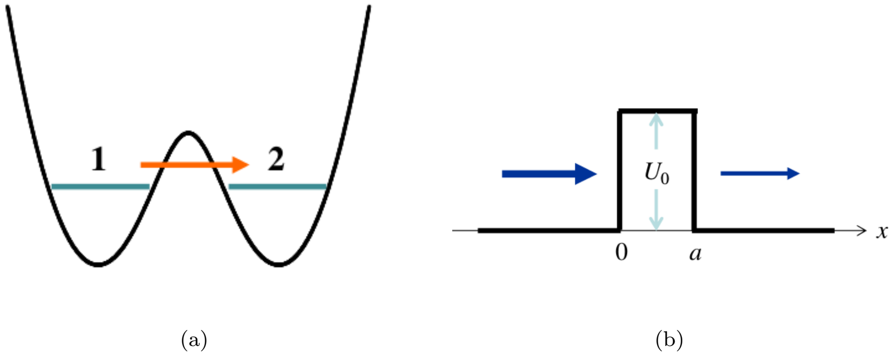

(a)

(b)

Figure 2.6: (a) Representation of a double potential energy well in which tunnelling can take place. A quantum particle can tunnel from a state localized in a well (e.g., state 1) to a state localized in the other well (state 2), although its (average) quantum-mechanical energy is lower than the top of the potential energy barrier between the two wells. (b) Simplest potential model (rectangular potential barrier) for calculating the transmission coefficient or tunnelling probability. U_0 is the height of the barrier and a is its width. .

The gap between tip and substrate of an STM setup poses a potential barrier for the electron flux between the two conductors, even when molecules are in between. However, the height of this barrier is reduced by inserting a molecular medium. Applying the above to the STM junction one has to consider that an essentially continuous manifold of electronic states are available in each metal and that the application of a bias between tip and substrate will translate the electronic energy levels of one metal compared to those of the other (see Figure 2.7). At zero temperature and zero bias, the Fermi functions for the two electrodes are a step functions with the same Fermi energy, so that no net tunnelling current is observed. Under a bias voltage, the relative shift of the two Fermi function makes in such a way that electrons from one electrode can tunnel through the tip-substrate gap and occupy empty levels of the other electrode. The direction of the tunnelling current will clearly depend on the sign of the bias voltage difference.

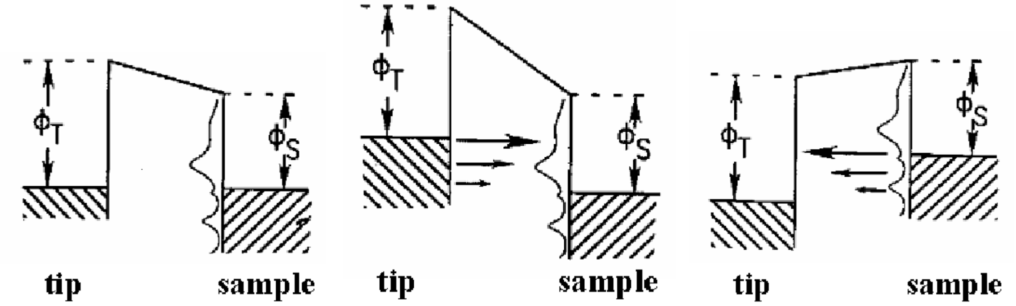

FIGURE 2.7: Energy scheme of tip and sample for different bias voltages, the left figure shows Thermal equilibrium, zero bias, the middle figure, Positive bias, tunnelling into empty sample states, the right figure, Negative bias, tunnelling from occupied sample states. Figure reproduced from. [3]

A very important quantum-mechanical phenomenon can take place and support conduction when a structured medium such as a biomolecule is inserted between substrate and tip. The inhomogeneous environment of the protein medium between substrate and tip can create a potential well, and thus a double potential barrier, for the transferring charge(s), as schematically represented in Figure 2.8 When the energy of the incoming particle is the same as (in resonance with) a bound energy level in the potential well, the particle can tunnel through the double-barrier region with unit probability, rather than experiencing the probability exponential drop of equation 2.13 [1, 43]. In the case of resonance tunnelling (or resonant tunnelling), the transmission coefficient for the incoming particle of energy ε is

$$\tau(\varepsilon; z) = \frac{\mathit{\Gamma}_S \mathit{\Gamma}_T(z)}{(\varepsilon - \varepsilon_0)^2 + [\mathit{\Gamma}_S + \mathit{\Gamma}_T(z)]^2/4} \tag{2.14}$$

where ε_0 is an effective [1] energy of the level in the well, $\mathit{\Gamma}_S$ and $\mathit{\Gamma}_T$(z) are the coupling strengths of the molecule to substrate and tip, respectively. The effect of changing z on the substrate-molecule coupling strength was neglected in equation 2.14, but the transmission coefficient maintains the same expression when this approximation is not satisfied. $\mathit{\Gamma}_T$ depends on the distance z of the tip from the substrate because z determines the tip-molecule distance. As one can easily see from equation 2.14, the maximum value of $\tau(\varepsilon)$ is achieved under the resonance condition $\varepsilon = \varepsilon_0$, and this value is unity only if $\mathit{\Gamma}_S = \mathit{\Gamma}_T(z)$ at some z .

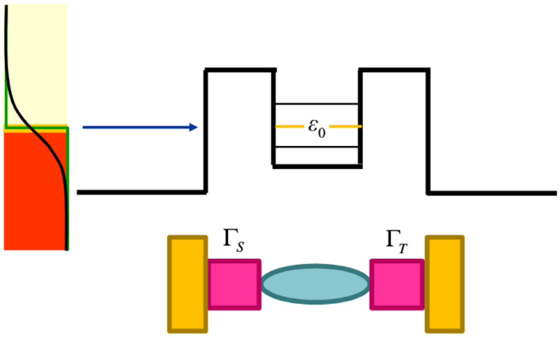

FIGURE 2.8: Schematic representation of resonant tunnelling. The potential well between the two barriers has some bound levels. When the energy of the incident particle is in resonance with a bound level in the well, the transmission coefficient is unity for a symmetric double barrier. The two barriers and the well can represent the potential profile seen by an electron across a molecule which is interfaced to two electrodes in a junction. The constant potential regions grossly represent parts of the molecular bridge with different structural properties. If metal electrodes are involved, the Fermi function characterizes the injection energy levels, and is here described similarly to Figure 2.4. Two discrete levels in the potential well are resonant with electronic levels of the substrate, and one of them (which is named ε_0 in the figure) is resonant with the substrate Fermi level.

2.3 Charge Transport (Current) Mechanisms.

2.3.1 Charge Transport via Coherent Tunnelling

For relatively small molecules, and especially (but not only [50]) in the absence of redox centres, resonance tunnelling can be the charge transport mechanism at play, although some incoherence is present due to thermal motion of the molecular system. In this regime of conduction, the current at given bias voltage V and substrate-tip distance z is written, within the Landauer-Büttiker formalism [1, 51], as

$$I(V;z) = \frac{2e}{h}\int_{-\infty}^{\infty} d\varepsilon \tau_{total}(\varepsilon;z)\left[f_s(\varepsilon;V) - f_T(\varepsilon;V\right] \tag{2.15}$$

τ_{total} is the so-called all-to-all transmission coefficient, which counts all the initial and final electronic states of the transmission process that can be distinguished perpendicularly to the transmission process. In equation 2.15, $f_s(\varepsilon;V)$ and $f_T(\varepsilon;V)$ denote the Fermi functions for the substrate and tip, respectively, when V is the substrate-tip bias. At zero V, the two Fermi functions are identical and the current is zero, as expected. The temperature dependence of the current is limited to the appearance of T in these functions. This dependence disappears at low enough biases. In fact, it can be shown [1] that, when the potential drops at the two molecule-metal interfaces are much smaller than k_BT, the current is approximately

$$I(V;z) = G_0 \tau_{total}(\mu;z)V \tag{2.16}$$

where the transmission coefficient is taken at the Fermi energy and G_0 is the quantum of conductance:

$$G_0 = \frac{2e^2}{h} = 77.5\mu S \tag{2.17}$$

According to equation 2.16, the conductance is given by

$$\frac{G(z)}{G_0} = \tau_{total}(\mu;z) \tag{2.18}$$

and equals the quantum of conductance when τ_{total} is unity. Using equations 2.7, 2.13, and 2.14, neglecting constant terms in the right-hand side of equation 2.16, and taking the logarithm of both sides of the equation, one can write

$$lnG(z) \sim lnG_0 - \beta z \tag{2.19}$$

β is an average beta factor for the tunnelling barriers in Figure 2.8. Equation 2.19 was correctly used in this thesis to estimate β values. This equation generally leads to strong underestimation of tip distances from the substrate when β is assumed and specific z values are calculated from it. Yet, relative values of z estimated through equation 2.19 for similar systems may be compared.

2.3.2 Charge Transport via Hopping

Resonant tunnelling is a coherent quantum-mechanical process, and molecular thermal motion generally does not allow for the exclusive occurrence of this pure mechanism. Indeed, incoherence is, in general, introduced in the charge transport between the substrate and the tip by thermal motion of the intervening medium. Another physical mechanism can support conduction when relatively large redox molecules are adsorbed on the substrate and coherence throughout the extent of the molecular bridge is unachievable. The redox site in the molecule represents a potential (free) energy well for the transferring electron. Substrate-molecule and molecule-tip ET processes can occur through the combined nuclear dynamics-electron tunnelling mechanism that was described in Section 2.2, with ET rate constants described by equations 2.9 and 2.10. Let us assume that the junction is biased with higher electrostatic potential at the tip, so that the electrons flow from the substrate to the tip, while the reverse flow is negligible. Exploiting equation 2.13, one can rewrite equation 2.9 for the substrate-to-redox site ET and equation 2.10 for the redox site-to-tip ET as follows:

$$k_{S\rightarrow molecule}(V_{S-mol}) \cong |U_0|^2\, exp(-\beta_{S-mol} r_{S-mol}) A(V_{S-mol}) exp\left[-\frac{\Delta E(V_{S-mol})}{K_B T}\right] \tag{2.20}$$

$$k_{molecule\rightarrow T}(V_{mol-T}) \cong |U_0|^2\, exp(-\beta_{mol-T} r_{mol-T}) A(V_{mol-T}) \tag{2.21}$$

or, in compact form and with evident meaning of the symbols,

$$k_{S\rightarrow molecule}(V_{S-mol}) \cong k_S^0(V_{S-mol})exp(-\beta_{S-mol}r_{S-mol}) \tag{2.22}$$

$$k_{molecule\rightarrow T}(V_{mol-T}) \cong k_T^0(V_{mol-T})exp(-\beta_{mol-T}r_{mol-T}) \tag{2.23}$$

where U_0 is an extrapolated zero-distance electronic coupling,$r_{metal-mol}$ is an effective distance between the molecular redox site and the indicated metal, and $\beta_{metal-mol}$ is an effective decay factor (beta decay factor) for the intervening medium. Clearly, $V = V_{S-mol} + V_{mol-T}$. During I-z measurements, the beta factors and distances in the above equations, as well as the repartition of the tip-substrate potential drop between the two sides of the redox centre, are functions of the tip- substrate distance z, although this dependence is not explicitly indicated in equations (2.20-2.23) to simplify notation. For example, if the tip is retracted, r_{mol-T} increases, and also β_{mol-T} becomes larger because an increasing portion of the gap between redox centre and tip is not occupied by the molecule. Therefore, at a certain distance, $k_{molecule\rightarrow T}$ is surely the rate-limiting step in the charge transport through the STM system. Moreover, if the molecule also links to the tip (e.g., with the help of a second thiol) and is pulled, to some extent, during the retraction, then also r_{S-mol} and β_{S-mol} can be a little changed.

In the charge-hopping mechanism for conduction, there is full incoherence between the two ET steps, which can be independently described by the above equations. For example, once the (solvated) molecule receives an electron from the substrate, its nuclei rearrange to the equilibrium coordinates in the presence of the excess electron on a time scale that is much faster than the average time required for the next ET to the tip (that is, $1/k_{molecule\rightarrow T}$). Note that in this mechanism, differently from resonant tunnelling, one can define charging states of the molecule between the different ET steps. For the STM system in Figure 2.5 under sufficiently high bias, the current can then be written as [47].

$$I \cong e\frac{k_{S\rightarrow molecule}k_{molecule\rightarrow T}}{k_{S\rightarrow molecule} + k_{molecule\rightarrow T}} \tag{2.24}$$

Over a range of z values for which the protein can bridge substrate and tip, and the two ET processes are characterized by similar values of r ($\approx z/2$) and similar beta decay factor characteristic of the protein medium ($\beta \approx \beta_{S-mol}$), it is

$$I \cong I_{protein} \sim exp(-\beta r) \tag{2.25}$$

When z increases enough that $k_{molecule \to T}$ becomes much smaller than $k_{S \to molecule}$, it is

$$I \cong \frac{k_{S \to molecule} k_{molecule \to T}}{k_{S \to molecule}} = ek_{molecule \to T} \sim exp(-\beta_{mol-T} r_{mol-T}) << I_{protein} \tag{2.26}$$

The last two equations can essentially explain the step seen in the current during the tip retraction.

Equations 2.25 and 2.26 characterize the dependence of the current on the length of the rate-limiting ET step in the presence of a single redox centre in the molecule. Considering a sequence of polymeric molecular bridges of different lengths, with a number of hopping sites proportional to the length of the bridge, the current will approximately scale down as the inverse length of the bridge (namely, with the inverse of the number of hopping sites) [1] or even more slowly if the bridge can be populated by multiple charges.

2.4 Proteins and their use in bionanoelectronics

Protein are large biomolecules that consist of a defined sequence of amino acid residues and perform a large number of functions in living organisms. Proteins are important constituents of which they define shape, construction, molecular transport and identification properties. Proteins engage in the catalysis of metabolic reactions and in DNA replication. 20 different amino acids are the building blocks of proteins. Different amino acid sequences generally lead to different protein folding into a three-dimensional structure with specific chemical properties and biological activity. The information which are needed to form the different types of proteins are saved in DNA and carried by RNA, which are akin chains of nucleotides [52]. One can define four levels of structure for a protein. The primary structure is just the sequence of amino acids. The secondary structure is the set of local structures that are mainly stabilized by hydrogen bonds. The most common features of secondary structure are α helixes, and β sheets and β-turns, At the next level of structural organisation, the secondary structure components arrange themselves to form a three dimensional folded structure that is the tertiary structure. At the next higher level of structure organisation, folded polypeptide chains come together in a specific arrangement that is called the quaternary structure. Two classes of proteins can generally be distinguished; globular proteins and fibrous proteins (which have an elongated shape) [52, 53].

Many organic molecules seem to be good candidates for use in nano-scale devices. Several studies have investigated the possibility of using organic molecules such as DNAs or proteins in future devices, so as to replace silicon-based nano electronics and transit to bionanoelectronics [54, 55]. In this area of investigation, the most ambitious goal is achieving control of single biomolecules as active elements in bionanoelectronics applications. At the nanoscale typical of protein molecules, the electrical current can be described in terms of individual electron transfer (ET) processes. Protein functions generally involve charge transfer processes. Thus, the idea is to exploit the rich charge dynamics involved in the normal operation of biomolecules for designing nanodevices with novel functions and high-density integrated circuitry. However, the practical implementation of this idea requires to preserve and control the biomolecular structure and function in a non-natural context, at the interface with inorganic components. While several difficulties have hampered the development of bionanoelectronics according to the lines of standard electronics, a huge amount of recent research confirms the potential of the general idea in different ways, with application that range from pure electronics to biomedicine [56–58], from information transfer [59, 60] to chemical sensing

[15, 17, 61], from enzymatic biofuel cells [14] to organic solar cells [9, 10]. Within this context, ET proteins such as cytochrome cyt b_{562} [62] and the green fluorescent protein (GFP) have attracted significant attention as promising candidates in nanobioelectronics applications. Moreover, the fluorescence characteristics of GFP determine its selective response to irradiation and its potential use in optoelectronics applications [55, 63]. Among other proteins of use (and of interest to this thesis work), we mention protein kinase A (PKA) and TEM beta Lactamase (TEM).

Critical factors in combining molecules with inorganic solids are the stability of the molecular anchoring and prevalent orientation of molecules. These are critical factors in order to preserve the biological activity of the molecular component and to ensure a stable, reproducible and efficient behaviour of the heterogeneous system (as an example, see Ref. [16], where immobilization strategies to develop enzymatic biosensors are discussed). Tilting of a redox molecule on the solid substrate can change the distance between the redox centre and the surface of the substrate, as well as the local polarization of the surface, and these facts have also been exploited in implementing sensing strategies at the nanoscale [64].a

So far, gold has been the most used substrate material for protein immobilization. This noble metal is chemically inert to biomolecules, and proteins can be bonded with high stability to gold through thiol groups. Mechanisms to control the strength of thiol-gold contacts have been studied until recently, showing the possibility to bind the thiol to the Au surface so strongly that retraction of the STM tip determines breaking of Au-Au bonds near the thiol binding site and extraction of thiolate bound to gold atoms. Thiol groups can be inserted in biomolecules, via introduction of cysteine residues. This can be achieved by genetic engineering of proteins to get the cysteine residues at the desired positions. In this way, one can obtain direct self-assembly of proteins on to gold surface [62]. The chemical modification of proteins at appropriate positions on their surfaces enables covalent bonding to the substrate and help to define a preferential orientations of the immobilized molecules [65]. One of the proteins that are amenable to this kind of engineering in the above way is cyt b_{562}. Despite some previous measurements of the electrical properties of this molecule absorbed on gold [62], further investigations are necessary, in order to provide more information on the I-z characteristic and study the effects of environmental conditions such as temperature and humidity on the structural and electrical properties of the functionalized surfaces.

Chemical functionalization of substrate surfaces can also be achieved by means of chemical groups other than thiols. One of these functional groups is pyrene, which is amenable to pi-stacking to the substrates such as graphite and graphene [66]. Graphene and graphite are carbon materials with unique structural and electronic properties that have, attracted a lot of attention since their discovery, especially for potential applications in electronics, including the ambitious goal to replace silicon in some future electronics. Moreover, these are sustainable carbon materials which can also be employed in novel devices for clean energy production (e.g., see Ref. [67]).

2.5 Proteins used in this project

2.5.1 Cytochrome $\mathbf{b_{562}}$($\mathbf{Cytb_{562}}$)

Cytochrome b_{562} is a small soluble protein (12.3 kDa) that can be produced by Escherichia coli (E coli). It is a four-helix protein with 106 amino acids which non-covalently binds a heme (redox) cofactor [68]. Cyt b_{562} is an ET protein. The presence of the redox haem cofactor and the natural ET function of this protein led to consider cyt b_{562} a good candidate for the realization of functionalized metal surfaces to be used in hybrid electronic devices. [28, 68].

Site-directed mutagenesis was used to generate different variants of cyt $\mathrm{b_{562}}$. In all variants, the protein was engineered to introduce a thiol-linking groups (via insertion of a cysteine residues) at suitable a positions for proteins anchoring and assembling on the Au(111). In particular, the single-mutant D5C was engineered by replacing the aspartate residue at position 5 with cysteine, to produce the D5C variant of the protein. Double mutants were also produced to define different orientations of the attached molecules on the surface. To this purpose, two cysteine residues were substituted on opposite sides of the protein, along two directions that approximately define the dimensions of the molecule. In the long-axis configuration (SH-LA), aspartates at positions 21 and 50 are substituted with cysteines. In the short axis configuration (SH-SA), the aspartate residue at position 5 and the lysine residue at position 104 are replaced by cysteine residues [28, 30]. The LA and SA variants result in different configurations on the substrate (see Figure 2.9), with expected heights of about 5.2 nm and 2.4 nm on the surface, respectively. This accordingly causes different distances between the molecular redox center and the surface.

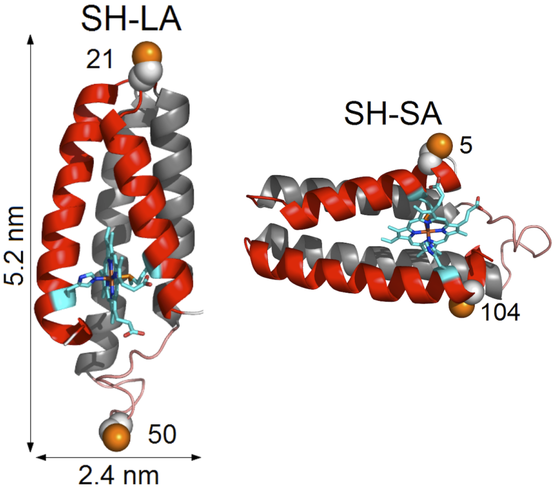

FIGURE 2.9: Double-mutant variants SH-LA and SH-SA of cyt b_{562} . The red and grey structures represent α helices. The molecular framework of the redox center is shown in cyan. The orange spheres represent the thiol groups that are introduced at the indicated positions and are used to link the biomolecule to the gold surfaces [4].

2.5.2 Green fluorescent protein(GFP)

The green fluorescent protein (GFP) is a 26 kDa fluorescent protein that was first isolated from the jellyfish Aequorea Victoria. The molecule is composed of 236 amino acids and has a cylindrical shape, as determined by an 11-strands β-sheet arranged in a beta barrel and there is an α-helix runs inside the beta barrel. The chromophore in GFP forms from the covalent rearrangement of 3 contiguous amino acids in the heart of the barrel structure. The shape of this protein is illustrated in Figure 2.10 [69]. GFP is a light-emitting protein whose chromophore is formed post-translationally from the sequence Ser65-Tyr66-Gly67 by an oxidative reaction. GFP has become an invaluable tool as a tag for monitoring gene expression and protein dynamics *invitro*. The fluorescence spectrum has a peak at 509 nm with a shoulder at 540 nm [63]. The optical properties of GFP offer considerable scope for its utilization as a non-invasive marker in cells. In this work, we used the superfolder GFP (sfGFP) variant (very robustly folded version of GFP), with the p -azidophenylalanine (azF) introduced into the protein through chemical modification [70] to be used to link the proteins directly to carbon allotrope materials or to be linked to pyrene by click chemistry-based strain-promoted azide-alkyne cycloaddition (SPAAC) approach [5].

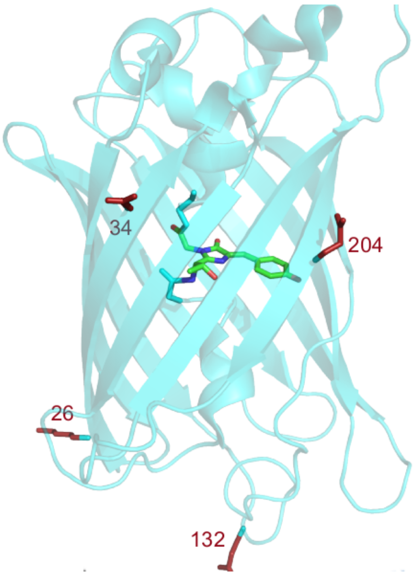

FIGURE 2.10: Engineered sfGFP molecule. The light blue structures represent helices. The chromophore is shown as the green part in the middle. The positions where the pyrene is bound (so as to link the protein to the carbon surface) are indicated in red. Figure donated by Reddington, Hartley from the Jones group.

2.5.3 Protein Kinase A(PKA)

The protein kinase A (PKA) enzyme belongs to the large family of protein kinases. The structure of PKA is shown in Figure 2.11. The chemical function of this protein consists in phosphorylating other proteins. Protein kinases do not work only as catalysts, but also as scaffolds, with the function to bind to other proteins. This function depends on the cell type and it is been studied [71]. Because of its chemical and mechanical properties, PKA is exploited in regulatory and signalling mechanisms of cells, thus suggesting its potential use in electronic devices. Recently, GFP-based biosensors were used to study the activity of protein kinases such as PKA in living cells, and in particular the function of this family of enzymes in cancer and drug discovery [72].

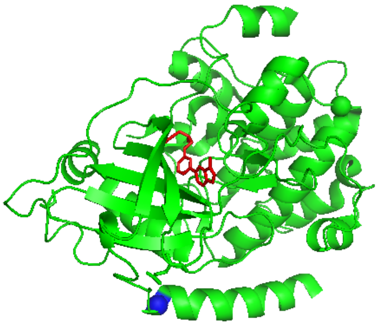

FIGURE 2.11: Structure of Protein Kinase A (PKA). The green structures represent α helices, while the flat arrows represent the β sheets. The active site is shown in red. Figure donated by Reddington, Hartley from the Jones group.

2.5.4 TEM beta-lactamases (TEM) Proteins

TEM beta-lactamase is a member of a wide bacterial enzymes family. These enzymes are produced by bacteria that show multiple resistance to beta-lactamase antibiotics. The structure of the TEM protein is shown in Figure 2.12. It is consists of a α domain, which contains six α helices, and a beta domain. Functionalization of TEM beta-lactamase with azF and by using click chemistry, linking small molecular groups that introduce new properties in the biomolecule can be achieved. Click chemistry has become a flourishing approach to bioconjugation in that enhance biomolecular functionalities.

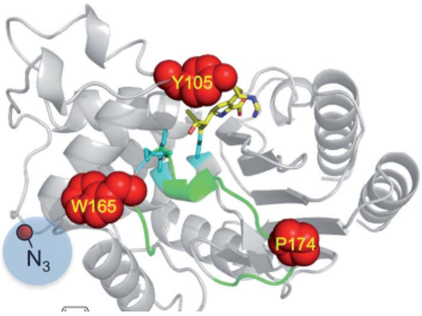

FIGURE 2.12: Engineered TEM β-lactamase. The light grey structures represent α helices. The regions in red represent positions for azF insertion. This insertion serves to link the protein to pyrene, which is used to bind the protein to the carbon surface. In this figure the azF is linked to position 165 [5].

In the molecular engineering, the unnatural amino acid p-azido-L-phenylalanine (azF) was inserted in the proteins. This amino acid was used because its chemical properties makes it a good candidate for controlling proteins post transnationally. It is an analogue of phenylalanine, with an azide functional group (N3) at the para position of the benzene group (a phenyl azide). It is the azide, or more precisely the phenyl azide group that makes this amino acid particularly useful to implement new non-native chemistry in proteins.

Phenyl azides are particularly sensitive to UV light. This feature can be used to modulate the behaviour of the engineered protein in response to irradiation. During irradiation with light below 310 nm [73], phenyl azide loses the N2 group and transform into a reactive nitrene species with two lone pairs of electrons. This nitrene radical can follow various reaction routes depending on its immediate environment [74]. The reaction pathways include insertion reactions with both N-H and C-H bonds and addition reactions with C=C double bonds (see Figure 2.13 [6]). The photosensitivity and reactivity of azF have been employed in the past for studying protein-protein and protein-ligand interactions [75]. Also, the crosslinking feature of azF has been used to help the functional analysis of native proteins, by immobilizing proteins on surfaces for surface plasmon resonance analysis [76].

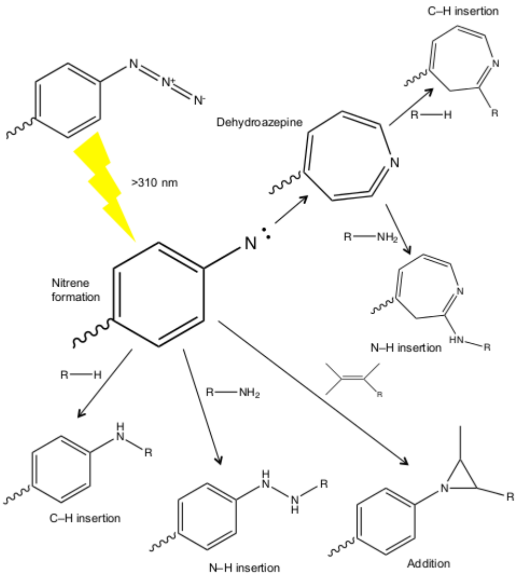

FIGURE 2.13: Activation of Phenyl-azide. Irradiation using light below 310 nm leads to the formation of the nitrene radical caused by the loss of molecular nitrogen. This species can then go down several reaction pathways [6].

2.5.4.1 Long-linker Pyrene

The SPAAC was used to covalently attach the azF residue, which was genetically encoded in TEM proteins, to a dibenzylcyclooctyne-pyrene (DBCO-pyrene) linker. This strategy enabled π-π binding of TEM proteins to carbon surfaces such as highly ordered pyrolytic graphite (HOPG) and graphene [5]. This protein deposition results in single proteins molecules decorating the carbon surface when appropriate protein concentrations and incubation times are used. The DBCO-pyrene complex consists of two connected aromatic structures with four rings each, and because of its size it is called the long linker here.

Two variants of TEM β-lactamase, i.e., TEM105azF and TEM165azF, engineered with pyrene were used to bind to graphene. Cyt b_{562}, sfGFP204 and PKA proteins were similarly engineered to exploit pyrene for bonding to carbon surfaces. With regard to the systems studied in this work, click chemistry was applied to modify the TEM protein, so as to have pyrene at positions 105 and 165, and also for pyrene linking to sfGFP and PKA at positions 204 and 31, respectively. Pyrene represents a good linker for protein anchoring to surfaces such as graphite or graphene. The protein samples and the figures of protein structures in this chapter were prepared by Dafydd Jones and his group in the Bioscience Department.

2.5.4.2 Short-linker Pyrene

Another strategy for attaching the azF residue to pyrene was used, which consisted in using copper-promoted azide-alkyne cycloaddition (CuAAC) method to link the pyrene moiety to the azF residue. Thus, there is no need for the DBCO interface between the protein and the pyrene linker, that is why we use the name short-linker. This type of linking to pyrene was used for cyt b_{562} , and also enabled the study of the single molecule properties on graphene.

In this Type copper-promoted azide-alkyne cycloaddition CuAAC was used to link the pyrene to the azF residue, this method allows direct coupling to the azido-group of azF in the protein in which there is no need to the DBCO as interface between the protein and the pyrene linke but copper in needed for this interaction to catalyse it, that is why we can call it short-linker.

Chapter 3

Scanning Probe Microscopies and Environmental Cell

3.1 Introduction

STM is one of the most important tools to gain knowledge and control on the nanoworld. Recent years have witnessed big changes in scientific research aimed to get control on the nanoscale and to exploit molecules with refined functions in non-natural contexts. Nanoscience and nanotechnology have developed tools to face the difficulties resulting from the small size of the systems investigated, the limits imposed by quantum mechanics principles, and the daring goal to combine the properties of molecules and solid-state components. Among such tools, extremely important are scanning probe microscopies (SPM) such as Atomic Force Microscopy (AFM) and Scanning Tunnelling Microscopy (STM). These techniques have played vital roles in investigating the properties of nano-structured materials, since their invention in the early 1980s. The applicability of STM and AFM to the nanoscale is strictly related to the tiny dimensions of the scanning component: the tip. This is the key component to approach and investigate nano-structured organic and inorganic materials, in both air and aqueous environment, and to enable measurements on single molecules. These microscopies are the most widely used in ambient conditions and require minimum sample preparation. They can give information on the topography of the surface, providing two-dimensional and three-dimensional images as well. The data provided by both investigation systems span a length scale from angstroms to microns, and give information on physical parameters such as height, shape, roughness, and surface morphology, as well as distribution and conductance of the molecules adsorbed on a surface [77]. Consequently, these techniques opened the door to discover the world of bio-nanostructured materials and understand the essential processes at play in such materials. To perform the measurements in this project we used STM and AFM systems. We also used home-built STM, which was designed and constructed in the School of Physics and Astronomy at Cardiff University and allows for high-resolution measurements [28].

Environmental conditions can influence STM measurements. In fact, physical conditions such as humidity have effect on the electron transfer processes through the molecules and across the molecule-electrode interfaces [78, 79]. Biomolecules with charge-transfer functions are often used in modern nanoelectronic applications [54, 80, 81], with the aim to exploit their refined functionalities in future nanodevices. Even in contexts very different from their natural environment, interstitial and environmental water can influence the structural properties of these molecules, and therefore their charge-transfer function. For example the effect of interstitial water on electron self exchange reactions between azurin molecules was demonstrated [78, 79]. The presence of water can also affect other properties of the experimental setup. For example, the effect of the relative humidity on the potential barrier height between a Pt/Ir STM tip and a gold surface was measured [82]. Pan *et al.* have designed and developed an STM setup that also operates at low temperature, in order to study the effect of temperature on the STM measurements [83].

These studies inspired us to build a system for providing control of both temperature and humidity on the STM setup. Hence, we placed the home-built STM inside the control system to perform our STM imaging and measurements at different values of temperature and humidity, and thus to study the effects of these physical variables on the structural and conductive behaviours of biomolecules and metal-biomolecule interfaces.

In this chapter, we describe the design and construction of a control environmental system that enables the operation of STM under different conditions of temperature and humidity. We will explain the structure of the system and the software used to control the temperature and humidity in the environmental chamber. In order to make our description self-contained, we first summarize the working principles of scanning probe microscopies (SPMs) such as Atomic force microscopy (AFM) and scanning tunnelling microscopy (STM).

3.2 Scanning Probe Microscopies

3.2.1 Scanning Tunnelling Microscopy (STM)

Scanning tunnelling microscopy (STM) was invented in the early 1980s by Gerd Binnig and Heinrich Rohre [77]. STM is based on the tunnelling of electrons between two solid-state components: the tip and the sample. The tip of the STM has to be sharp and made of a conductive material. Then, current can flow through the sample when a bias voltage is applied between the tip and the substrate. A sketch of the STM setup is shown in Figure 3.1. Electrons from the sample tunnel into the tip or vice versa (according to the sign of the bias voltage) when the tip is close enough to or in contact with the sample or directly with the substrate. A 3D scanner with an electronic feedback loop is used for raster scanning across the sample, so as to monitor the tunnelling current and to obtain a topographical image of the surface. The tunnelling current changes with the distance between the sample and the tip, so this signal is used to perform the STM image of the surface [84]. An important feature of STM is the possibility to carry out local tunnelling spectroscopy, by measuring the current between tip and substrate as a function of the gap voltage, at a fixed position of the tip. This kind of measurements can give information about the local electronic structure of the sample. The properties of the tip play a very important role in producing the STM measurements. Two factors mainly impact the measurements: the shape and the chemical structure of the tip. The material of the tip can affect the STM measurements. Mostly, metallic tips are used. A common tip material is platinum iridium(Pt-Ir), which can be used under ambient conditions because the platinum is inert to oxidation, while the iridium is added to increase the stiffness of the tip. A sharp tip can be obtained by cutting a Pt-Ir wire. This type of tip was used in the present work. Scanning with the STM system can be performed in two modes:

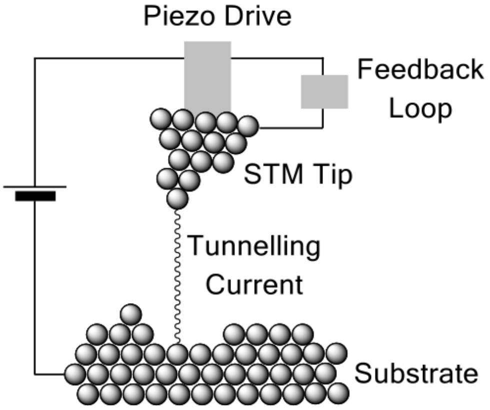

Figure 3.1: Schematic diagram of an STM.

3.2.1.1 Constant-Height Mode

This mode maintains the height of the STM tip above the surface at a constant value. The tunnelling current will change according to the topography and the electronic properties of the surface, thus producing the image of the sample.

3.2.1.2 Constant-Current Mode

The tunnelling current is kept constant in this mode, which is achieved by controlling the height of the scanner at every point measured on the surface until the established set point current is reached. The vertical position of the tip at each data point is used to form the topographic image of the surface.

3.2.2 Atomic Force Microscopy

Atomic force microscopy is one of the techniques commonly used to perform measurements in nanotechnology, including nanoscale material science, modern biophysics, etc. This microscopy was invented in 1986 by G. Binnig, C.F Quate and Ch. Gerber [85]. The main idea behind this technique is that, a sharp tip at the free end of a cantilever interacts with the surface to be raster-scanned, while the deflection of the cantilever is monitored by the reflection of a laser beam onto a position-sensitive detector. Therefore, the surface-dependent deflection of the cantilever is finally measured by a detector during the scan. Using the deflection data, a computer software produces an image for the surface topography. AFM is used to study both insulators and conductors unlike the STM, which can be used to measure just conducting surfaces. There are three AFM techniques for imaging; contact, non contact and intermediate contact AFM [85–87].

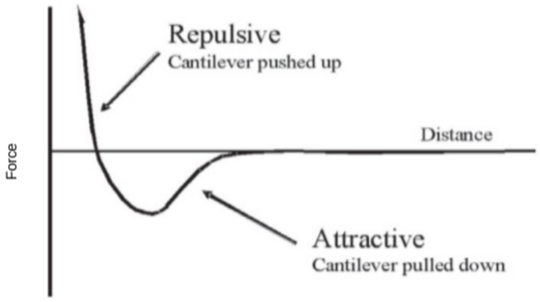

FIGURE 3.2: Interatomic force vs. distance for an AFM probe-sample system. Two regimes are highlighted: the contact regime and the non-contact regime. In the contact regime, the cantilever is held very close to the sample surface (a few Angstroms apart) and the interatomic force between the cantilever and the sample is repulsive. In the non-contact regime, the cantilever is held far from the surface (that is, tens to hundreds of Angstroms) and the interatomic force is attractive.

Figure 3.2 shows the potential energy between the AFM probe and the surface. The layer of contamination on the surface causes the attractive forces. The repulsive forces at short distance cause the cantilever to bend up and they increase rapidly as the probe begins to contact the surface. Two methods can be used for establishing the forces between AFM probe and sample. In contact mode the deviation of the cantilever is measured, while in tapping mode the changes in amplitude and frequency are used to measure the force [87].

3.2.2.1 Contact-Mode AFM

In contact-AFM mode or repulsive mode, the tip makes contact with the surface of the sample. During the scanning, the scanner controls the movement between the tip and the sample. Therefore, the contact force causes cantilever bending to suit the change in topography. From the cantilever deflection, the AFM can produce the topographic data set and then the pertinent image of the scanned surface. The contact-AFM can operate in constant-height mode or constant-force mode. In the constant-height mode, the height of the scanner is set and this mode is used for atomistic scale imaging of substrates. In the constant-force mode, the cantilever deflection is constant, which means that the force on the surface is a constant, and the scanner motion produces the image. This mode can be used to provide real-time images of changing surfaces.

3.2.2.2 Non Contact-Mode AFM

Non-contact AFM is one of many oscillating cantilever techniques. It is preferable to other techniques because it can measure the surface topography without contact between the sample and the tip, and hence without damaging the sample. The strength of the interaction force is very low. Therefore, this mode can be used to measure soft samples. In addition, the sample will not be contaminated as there is no contact between the tip and the substrate. In non-contact mode, one makes the cantilever to oscillate near its resonant frequency, and the resonant frequency or the oscillating amplitude is used as the feedback parameter in the feedback loop. Changes in the height can be used to produce the image of the sample topography.

3.2.2.3 Intermittent Contact-Mode AFM (Tapping Mode)

In the contact mode, the force on the sample is large when imaging biological samples, so intermittent contact AFM, also called tapping mode AFM, is an important methodology for analysing surfaces that contain biological samples [53, 87]. Similarly to the non-contact AFM, the cantilever oscillates close to its resonance frequency. However, here the tip is pushed closer to the surface and taps it. The amplitude of the cantilever vibration changes according to the sample-tip gap, and thus an image that reflects the surface topography is obtained depending on this change. The intermittent contact mode and the non contact-mode are desirable approaches to study functionalized surfaces, because they do not damage the sample since the cantilever does not touch the surface but just the bottom swing of the cantilever can touch the surface.

3.3 Environmental Cell Design

The system consists of two parts; One is the humidity mixing chamber, which provides the humid nitrogen gas. This chamber is encased in an aluminium box. Inside, a smaller box containing deionised water though which nitrogen gas is bubbled. The outlet humid gas is then mixed with dry nitrogen gas in a mixing chamber to control the humidity of the mixed gas. The humidity generating chamber was built in the project including this work but not used. The other part of the environmental cell, is the STM chamber (see Figure 3.4), which is connected to the humidity chamber through a plastic pipe. The STM chamber is also a box made of aluminium, with a baseplate of 200 × 230 mm, and is coated with two insulating layers, each layer being 25 mm thick. We were able to reduce the humidity in the STM chamber compared to the ambient conditions (so as to carry out measurements at different humidities) by pumping dry nitrogen inside. Future use of the humidity chamber will allow us to increase the humidity in the STM chamber with respect to the ambient.

The home-built STM is placed at the centre of the STM chamber. Peltier elements RS 4901373 are placed on opposite sides of the chamber for heating and cooling purposes. Peltier elements are very good for controlling the temperature in the environment of the STM, because these elements are vibration-free. In addition, they have small size and weight. Heat sinks beside the peltier elements can cool them down by air convection only, without any fan to exclude extra vibrations. The chamber has two pairs of peltier elements and heat sinks, placed on opposite sides. The cooling power depends on temperature difference (the difference between the ambient temperature and the desired temperature), hot plate cooling, and drive current. At 4 K difference, infinite hot plate cooling, and 3 A, a cooling power of 23.6 Watt was measured. The metal chambers were produced in the mechanical workshop. The chamber includes two sets of thermometers and humidity meters placed beside the sample and on the top part of the chamber. All the wires for the STM and for the controlling sensors are placed underneath the base. The sensors were controlled by a Python program which was written by Dr. Martin Elliott. Andriy Moskalenko assembled and tested the system, and produced Figure 3.3. Andrew Harrison from the electronic workshop provided the system electronics.

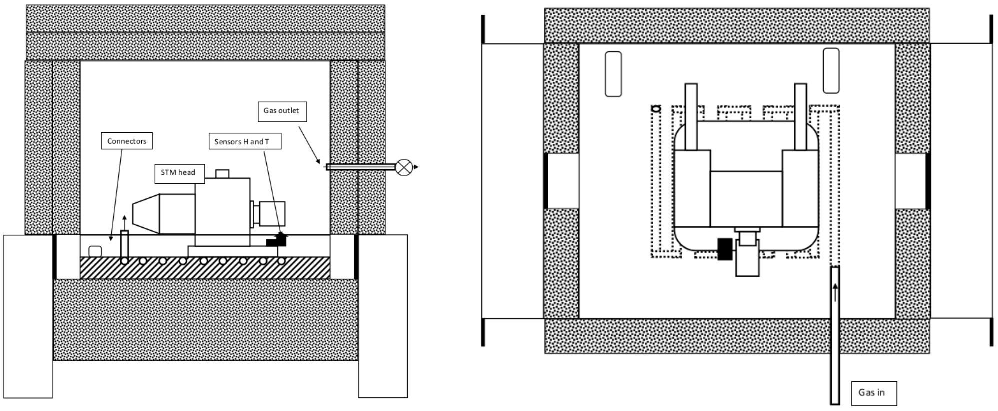

(a) (b)

FIGURE 3.3: Schematic diagram of STM chamber of the Environmental System.(a) Side view , (b) top view.

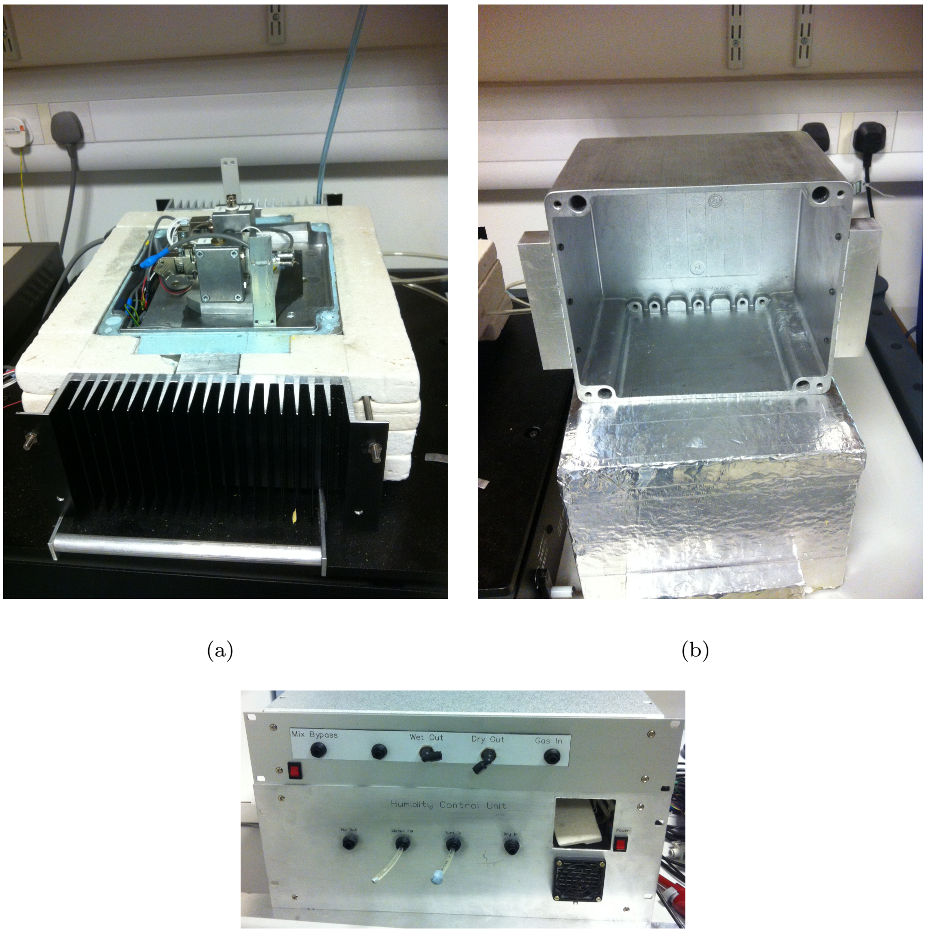

(a) (b)

(c)

Figure 3.4: Picture of STM chamber of the Environmental System.(a) STM system. (b) STM system box (c) Humidity system.

Several sensors were placed at desired positions in both chambers to control temperature and humidity. The heating and cooling elements are controlled through a PC software. For the temperature control, the main components are a microcontroller, a difference amplifier circuit, digital to analog (DAC) circuit. The microcontroller output signal depends on the set temperature and the temperature detected by the thermistor. The control signal is suitably amplified to drive the peltier device to either increase or decrease the bath temperature. Python was used for the interface with the user. To control the temperature, we need just to type the desired value which is passed to the microcontroller by serial communication. We can also check the temperature plot on the monitor.

We have to mention that both chambers and the connection pipes are very well shielded with thermal insulators. The system needs to be used so as to avoid condensation while the desired temperature and humidity conditions are achieved. The temperature in both chambers should be exactly the same in order to prevent the occurrence of condensation. The correct use of this system provides a good control of the environmental humidity and temperature, and thus allowed us to study the effect of these physical parameters on the properties of the nanostructures investigated.

3.4 Conclusions

In this short chapter, we described the design of an environmental system that was built, in the project including this work, to enable the use of SPM techniques under controlled conditions of humidity and temperature. The constructed control chamber has a dual importance in nanoscience studies: (i) to reduce the variability of environmental conditions that can lead to accordingly variable and difficult-to-interpret experimental results; (ii) to facilitate closer comparisons with theoretical studies, and thus faster useful interpretations of the same experimental results in terms of their chemical-physical underpinnings. In this chapter, we also stressed the importance of SPM techniques such as AFM and STM in the study of nanostructured materials, and we briefly described their operation principles.

Chapter 4

Proteins on Graphene

4.1 Introduction

Graphene is a unique 2D material which was first produced by exfoliation from graphite in 2004 [88]. This 2D structure can be in the form of a mono layer or a few layers of carbon atoms arranged in six-membered rings. Its extraordinary thermal, mechanical and electrical properties make it an important candidate for several applications. This is the reason why graphene has attracted rapidly growing attention in the past decade, with a consequent increase of experimental and theoretical studies of its properties and potential applications [89–91]. Graphene can be exfoliated from three-dimensional graphite crystals using micro-mechanical cleavage. This approach is allowed by the weak van der Waals forces between graphite layers. Thus, using tape, one can peel single layers from bulk graphite and obtain graphene samples of high quality. However, in this procedure the van der Waals forces between the first two layers must be overcome without perturbing any subsequent sheets [92]. Graphene is very important in chemical sensing applications due to its 2D structure and the two-dimensional characteristic is generally maintained in multilayer graphene; e.g., see [93].

Different molecular species can be linked to a graphene surface and influence the electron transport through graphene [94]. Graphene can also be used as the sensing component in photo-detectors [95]. This application requires that one is able to control the wavelength of the device response. The possibility to alter and control the conductive properties of graphene by its functionalization, inspire research for the development of methods to combine the functionality of biomolecules (in particular, proteins) with the properties of graphene in hybrid bioelectronic devices.

Chemical functionalization of graphene is necessary to enable various applications of graphene. The functionalization can be performed via either covalent or non covalent strategies [96–99]. Our aim is to immobilise protein molecules on graphene for its suitable functionalization. For this purpose, we engineer molecules relevant to bionanoelectronics by insertion of specific functional groups that enable them to be anchored to graphene surfaces. After immobilisation we carry out electrical characterization of the molecule-graphene system.

In this chapter we describe the experiments that were carried out to investigate the charge conduction through different types of proteins, covalently and non-covalently immobilised on graphene and graphite substrates. STM and AFM were used for imaging. The pyrene functional group was used for non-covalent linking of the proteins to the carbon surface. Azide was used for covalent protein anchoring to graphene. To this aim, we developed an experimental protocol in which the necessary activation of the azide group is achieved by UV irradiation.

4.2 Protein Engineering

Click chemistry is a method which can be used for protein modification, where it is possible to obtain new properties by the insertion of functional groups. This method was applied to modify PKA (protein kinase A), sfGFP (green fluorescent protein) and TEM (TEM beta lactamase) with long-linker pyrene, so as to have pyrene linking at positions 31, 204 and 105 or 165 as described in chapter 2. Pyrene was shown to be a good linker for protein to surfaces such as graphite or graphene [97, 100]. We performed another type of modification on cyt b_{562} using pyrene, which can be called a short-linker pyrene variation of the method, so as to enable linking to the graphene surface.

4.3 Proteins on Graphite

4.3.1 Cyt b_{562}, sfGFP, PKA on Graphite

At the first stage of this research, highly ordered pyrolytic graphite (HOPG) was used as the substrate for the proteins, β-lactamase, sfGFP204, PKA and cyt b_{562} with long and short pyrene linkers effective for anchoring to graphite and graphene surfaces. These proteins were deposited on HOPG. Different concentrations (5, 0.5, 0.1, 0.25, 0.05, 0.025) μM were tested with same time of incubation of 5 minutes, to find the optimal concentration for our study. The flakes of HOPG which are used in this work were mechanically exfoliated from the bulk piece of graphite by means of an adhesive tape. Placing a piece of tape on the bulk graphite, the top graphite layer was peeled to obtain a clean surface, from which the freshly produced flake was removed by means of tweezers. The HOPG flakes were imaged using AFM and STM in air at room temperature prior to incubation with proteins. Figure 4.1 shows the raw AFM and STM images of the surface.

The incubation consisted of the immersion of the flakes in the protein solutions for 5 minutes. Then the samples were rinsed with deionised water to remove the excess protein, and dried with nitrogen to be ready for imaging. Cyt b_{562} with short and long linker pyrene, PKA31 and sfGFP204 proteins were imaged by AFM. After the protein incubation, the graphite surface was covered with islands of proteins for high protein concentrations, which are 5 μM and 0.5 μM as seen in Figure 4.2.

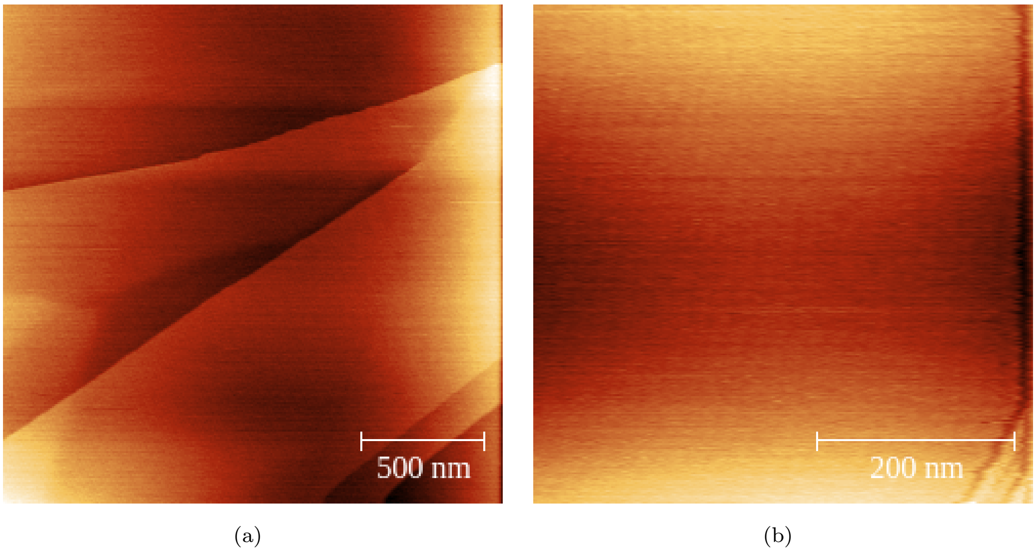

(a) (b)

FIGURE 4.1: Topographic image of HOPG. (a) AFM image; the lines represent the edges of the graphite. (z-range= 0-4.3 nm). (b) STM image (z-range = 0-7.3 nm).

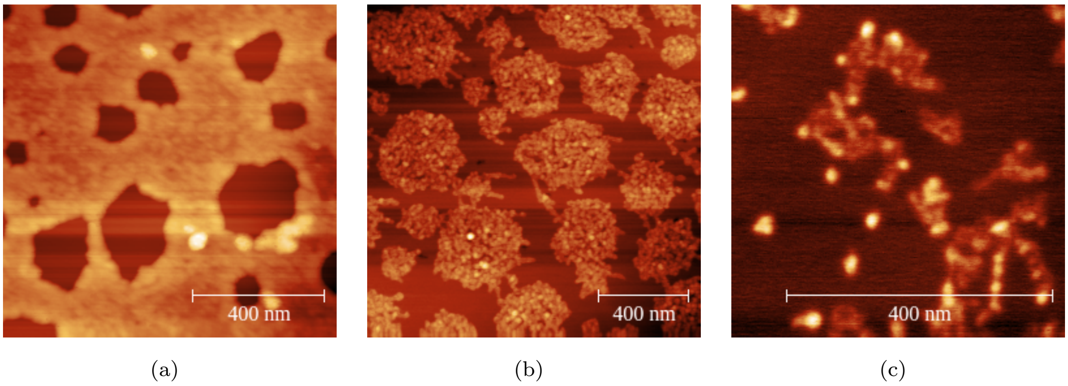

(a) (b) (c)

FIGURE 4.2: AFM image of sfGFP engineered with pyrene on HOPG. (a) Concentration = 5 μM, incubation time = 5 minutes. The white coverage represent the layer of proteins on the surface. The brown islands represent are areas of graphite which are not covered with the protein. (z-range = 0-24.6 nm), (b) concentration = 0.5 μM, incubation time = 5 minutes. The white islands represent the proteins on the surface and the darker areas between the islands are bare graphite surface (z-range = 0-11.1 nm), (c) concentration = 0.05 μM, incubation time = 5 minutes. The light dots represent the protein molecules on the surface (z-range = 0-8.9 nm).

The concentrations of 0.1 μM for cyt b_{562}, and 0.05 μM for sfGFP and PKA are very good for measuring individual proteins, as can be seen from Figures 4.2, 4.3 and 4.4. Cyt b_{562} SH-LA with short pyrene linker was attached to HOPG as well as can be seen in Figure 4.5, the used concentration was 0.025 μM which represents also good concentration to obtain individual proteins on the surface.

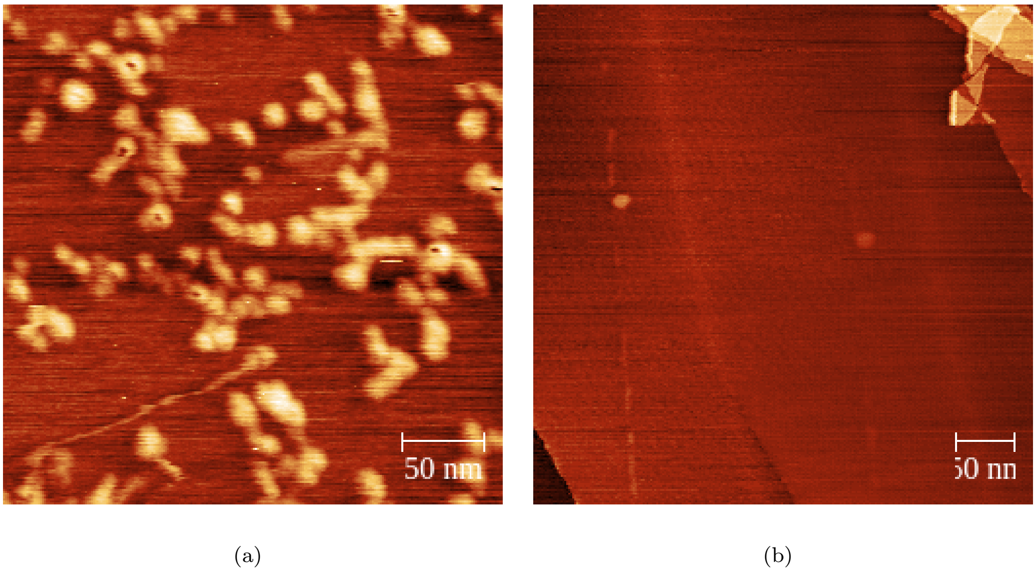

(a) (b)

Figure 4.3: Engineered PKA with pyrene-linker on HOPG.(a) AFM image, concentration = 0.05 μM and an incubation time of 5 minutes. The light dots represent the protein molecules on the surface (z-range = 0-4.2 nm). (b) STM image for a concentration of 0.05 μM and an incubation time of 5 minutes (z-range = 0-2.6 nm).

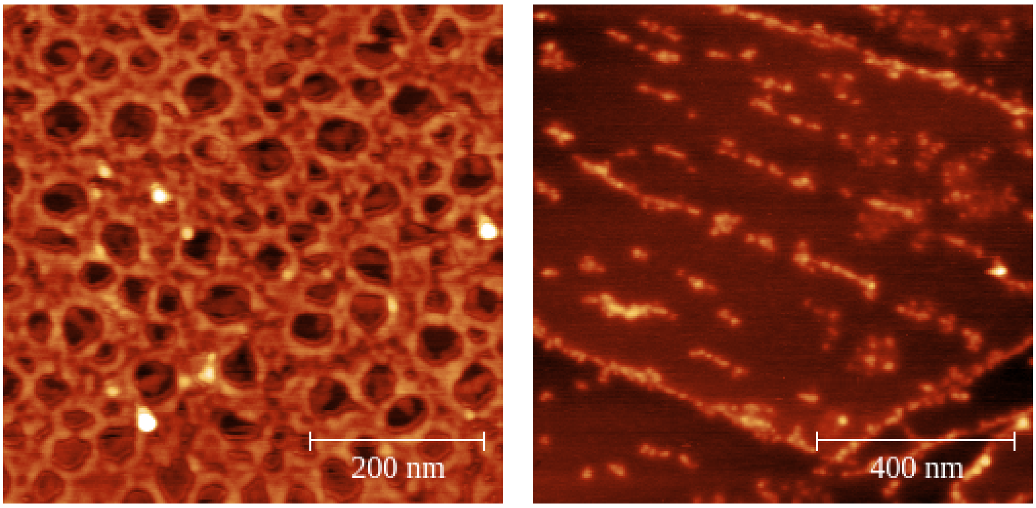

(a) (b)

FIGURE 4.4: AFM image of Cyt b_{562} with long-linker pyrene on HOPG.(a) Concentration = 0.25 μM, incubation time = 5 minutes. The figure shows a high protein coverage on the surface. The round islands are the areas which are free of protein molecules (z-range = 0-2 nm). (b) Concentration 0.1 μM, incubation time = 5 minutes. The light dots are the protein molecules which are bonded to the edges of the HOPG (z-range = 0-3.3 nm).

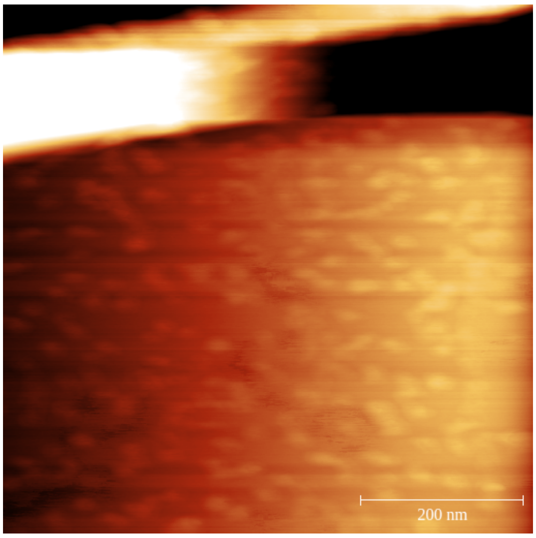

FIGURE 4.5: AFM image of Cyt b_{562} SH-LA with short linker pyrene on HOPG, concentration = 0.025 μM, incubation time = 5 minutes (z-range = -14.7-9.8 nm).

Successful AFM measurements were performed on all types of proteins, while STM imaging was not successful except of PKA as in Figure 4.3 but it was not reproducible, this can be due to removing the proteins by the STM tip as it is seen from the STM image for PKA, or the proteins are bound to the surface but there are small differences in conductance around the molecule which prevent sensing the molecules there by STM. The lateral dimensions of the protein molecules which were measured by AFM where slightly larger than the protein dimensions, due to the size of the tip. The measured molecular height was similar to that expected, except for some images, probably due to tapping of the AFM tip on the molecule. A drop-casting approach was also used to deposit the proteins on to the HOPG surface. This approach did not yield successful attachment of the proteins to the surface, because of the hydrophobic nature of the graphite surface. Both the engineered sfGFP204 and Cyt b_{562} were successfully attached to the graphite surface using an immersion method, as confirmed by AFM imaging. The average lateral and vertical molecular sizes from the experiments were about 9 nm and 5 nm respectively, which are on the order of magnitude expected for these proteins. The real dimensions of these proteins from x ray crystallography are (4.5, 3.5) nm for sfGFP and (5.2, 2.6) nm for cyt b_{562}. The differences from the measured values can be ascribed to the scanning conditions, where the AFM tip size affects the lateral dimensions of the measured molecule. The height of the molecules can be affected by AFM tip when using tapping mode technique specially if the molecules are soft biological proteins or presence of a thin contamination layer on the surface surrounding the molecule [101–103]. STM imaging of these proteins was not successful at any of concentrations used. The reason for this failure may be that the proteins are not strongly attached to the surface and thus are removed by the STM tip while doing the scanning, due to the interaction forces between tip and molecule, such as van der Waals or chemical forces which can be enough to move the molecules).

4.3.2 TEM β-lactamase on Graphite

Another protein immobilised on the HOPG surface was TEM β-lactamase. Two techniques were used for anchoring this protein to the HOPG surface. The first method consisted in the deposition of TEM β-lactamase that was previously modified with DBCO-pyrene. In the second approach, HOPG surface was first functionalised with pyrene, and then TEM105AzF molecules were deposited on the functionalised surface and linked through the azide phenylalanines to the pyrene groups. In the first approach, the HOPG flakes were immersed for 5 minutes in 5 nM of pre-modified protein solution. Then the samples were rinsed with deionised water, dried with nitrogen before imaging. In the second approach, the HOPG flakes were incubated with 0.2 mM pyrene for 15 minutes, the surface was immersed in 100 % DMSO (Dimethyl sulfoxide), rinsed with deionised water, and dried with nitrogen. The HOPG functionalised with pyrene was then immersed for 10 minutes in 100 μL of TEM105AzF of concentration 1 nM, rinsed with water, and dried with nitrogen. AFM imaging followed.

Both techniques, proteins linked to pyrene and proteins deposited over pyrene, enabled protein anchoring to the HOPG surface. However, the direct bonding to the surface through the pyrene linker was more successful than the pre-modified surface approach in producing well defined individual proteins on the surface. Note that clicking pyrene with protein method differs from and represents an advance on all the previous methods for protein bonding to HOPG surfaces. In previous approaches the proteins were attached to HOPG through gold clusters which were decorating the HOPG surface at earlier stage [104, 105] and others were using other linkers to functionlise the HOPG surface and thus enable proteins anchoring [106]. The AFM images in Figure 4.6 show the topography of the HOPG surface functionalised with TEM proteins by means of the two incubation methods. Again, the STM imaging did not show the TEM proteins on the surface, which may be ascribed to the limited conductivity of a protein on HOPG that contains no metal core or cofactors to further investigate this hypothesis, we compared the conductive properties of TEM, sfGFP and PKA on gold. The STM imaging failed again for the TEM proteins, while good STM images were obtained for sfGFP and PKA.

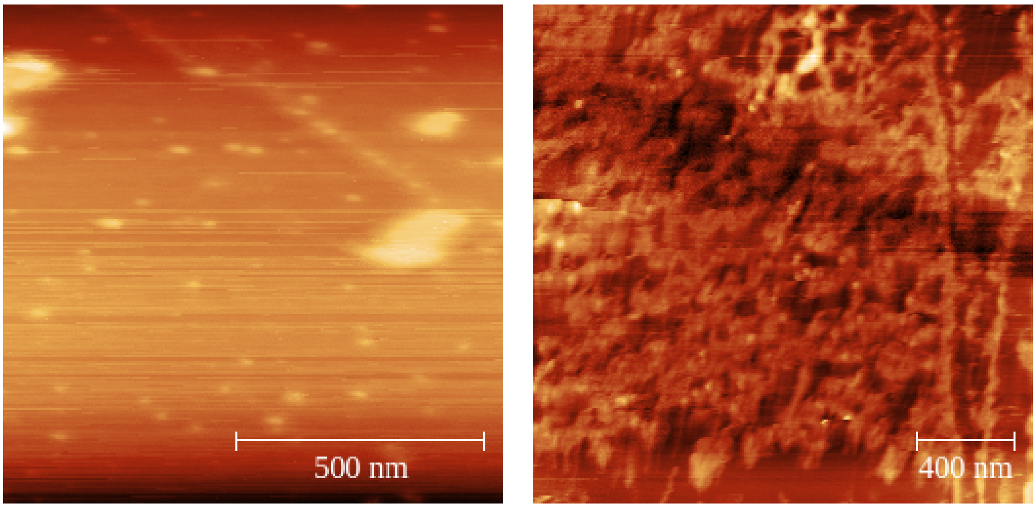

(a) (b)

FIGURE 4.6: (a) AFM image of TEM105 with pyrene on HOPG, the small light dots represent the protein molecules, the big dots may be agglomerated proteins (z-range = 0-10.2 nm). (b) AFM image of TEM105 attached through pyrene to HOPG. The big brown coverage represents the pyrene, while the small light dots are the protein molecules over the pyrene (z-range = 0-9.8 nm).

4.4 TEM β-lactamase on Graphene

Assemblies of biomolecules on solid surfaces and other substrates are critical ingredient in bio-nanoelectronics. Because of its unique properties, graphene is a good candidate as a substrate for molecules in nanoelectronic devices. Due to its unique electronic structure, especially the high density of the electronic states which covers wide energy range allows graphene with fast electron transfer, So graphene is very sensitive to electronic changes in the attached proteins, and thus it can effectively transfer the effects of these changes to the electrodes [107]. Therefore, changes in electrostatics, protein-protein and protein-substrate interactions can be easily detected. Moreover, specific protein attachment to graphene can provide an ideal setup for measuring single-molecule conduction. In our experiments, the protein attached to graphene was TEM β-lactamase. Investigating the behaviour of this protein on substrates is important for uses in biomedical nanoelectronics, including biosensing applications. Phenyl azide chemistry was encoded at defined positions in the protein. Using click chemistry (see section 2.6.3), pyrene was attached to the phenyl azide inserted in the TEM protein, thus enabling the protein assembly on the graphene surface.

4.4.1 Sample Preparation and Imaging

Samples of graphene on copper from Exeter University and from Graphene Supermarket were used. All graphene sheets were deposited on the copper substrates by means of chemical vapor deposition (CVD). Methane was used as the carbon source. The (4 mm thick) graphene on copper pieces were immersed in PBS containing protein and incubated at room temperature for 10 minutes. We used different protein solutions of wild type TEM β-lactamase and TEM β-lactamase pre-modified with the DBCO-pyrene, with different concentrations: (0.5, 0.010, 0.005 and 0.001) μM, and the incubation was done by drop cast or by immersion, pouring the protein in the incubation tube, and then holding the sample by tweezers, inside the solution. The samples were then immersed in about 50 ml of deionised water to remove the excess protein, and dried with nitrogen. AFM imaging was carried out using a Veeco Nanoscope IIa (Bruker) in tapping mode. Each area of a sample was scanned up to 10 times, with a total of 6 different regions imaged, to check the stability of the protein molecules on the graphene surface. Although the images show some drift, it is clear that the proteins are stably bound to the surface. That is, TEM proteins linked to pyrene were successfully attached to the graphene surface.

4.4.2 Results and Discussion

4.4.2.1 TEM165 Protein with Pyrene on Graphene Experiments

Before preparing the samples the pristine graphene substrates were imaged using AFM and STM techniques, in order to visualize the surface before incubation with the protein solution (see Figure 4.7) and enable a clear comparison with the functionalized surface. All specimens from Exeter and from graphene supermarket showed that the graphene surface is not homogeneous, but it contains different edges and wrinkles. These defects can affect the homogeneity of the deposited protein layer. For example, when a high concentration protein solution is used, we cannot obtain a homogeneous molecular layer on the graphene surface because proteins tend to attach more on the edges of the surface.

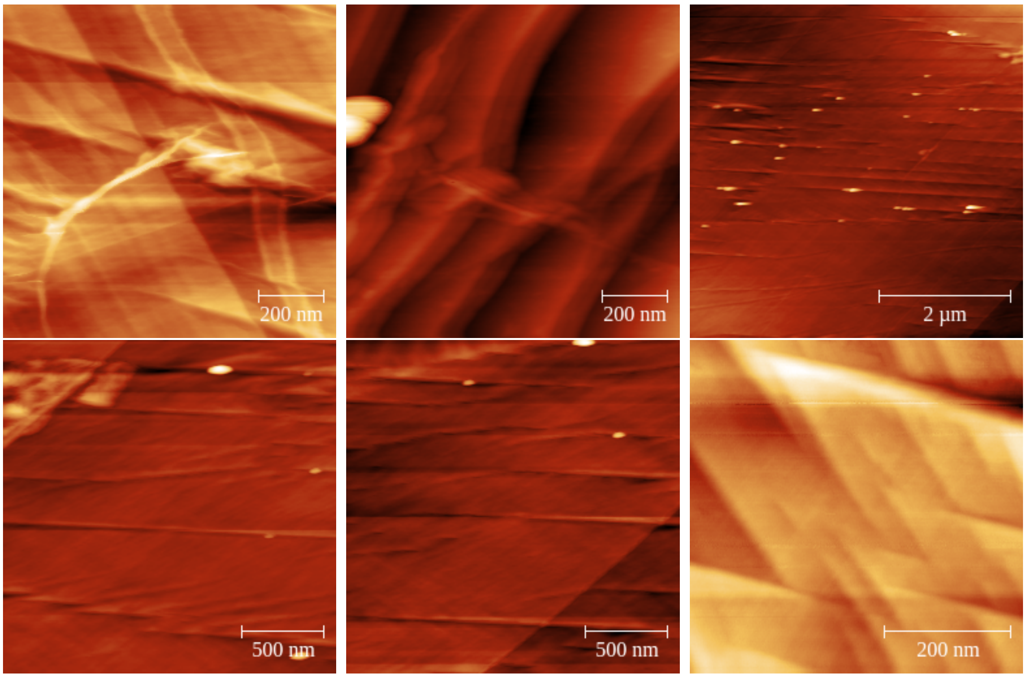

FIGURE 4.7: AFM images of different areas of pristine graphene from the Graphene Supermarket. Different areas from different samples show different features on the surface such as edges (the line-like features) or wrinkles (peaks and troughs).

Raman spectroscopy images of pristine graphene on Cu foils were taken by the Exeter group. Raman spectra collected in air at room temperature demonstrated mono layer graphene. The prominent peaks in the Raman spectrum of graphene are the G peak at about 1580 cm^{-1} and the 2D peak at about 2700 cm^{-1}. The G and 2D peaks, were clearly seen for all of the graphene specimens that we used in our experiments. Figure 4.8 shows typical Raman spectra for graphene samples from graphene supermarket and from Exeter, respectively.

The linking of the molecules to the graphene surface is achieved by π stacking of the pyrene to the graphene surface [108]. We demonstrated that enzymes can be interfaced with graphene by molecular engineering. To this end, AZF and pyrene

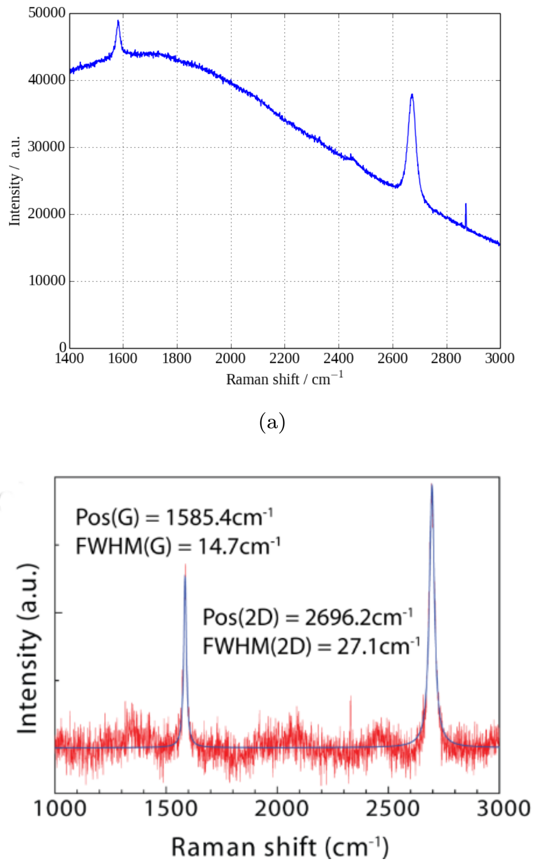

(a)

(b)

FIGURE 4.8: (a) Raman spectra for pristine graphene from graphene supermarket. (b) Raman spectra for pristine graphene from Exeter University.

were attached at defined position of the TEM. The coupling of pyrene to the protein prior to incubation with the graphene samples enabled a specific coupling to the surface, without the need to functionlise the carbon surface with pyrene as in previous studies [108, 109]. Intermittent-contact mode AFM (tapping mode) imaging showed that TEM165AZF modified with pyrene binds stably to graphene surfaces (see Figure 4.9), the used concentration was 0.005 μM and the incubation time was 10 minutes. The protein molecules were not significantly disturbed by multiple scans. The average apparent height was 3 nm, which is close to the predicted height of the protein bound in the designed orientation (Figure 4.10).

The average apparent lateral dimension was larger than predicted (10 nm versus 5 nm), as a result of tip convolution effects. Conversely, wild type TEM did not stably bind to the graphene surface, with tip contamination commonly observed

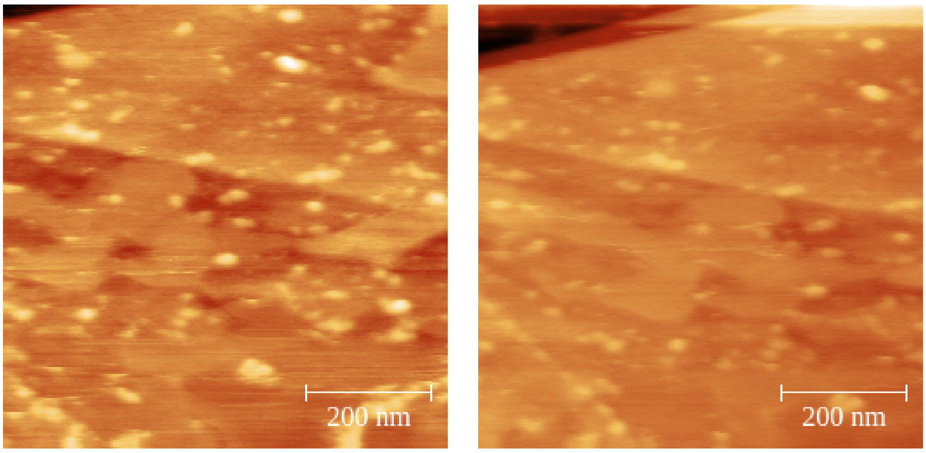

(a) (b)

Figure 4.9: AFM imaging of pyrene modified TEM165azF on graphene, it shows that the proteins are stable on the surface over multiple scans. (a) The sixth scan (z scale 0-10.1 nm). (b) The tenth scan (z scale 0-17.6 nm).

after multiple scans (see Figure 4.11, for the results of AFM imaging of wild-type TEM -lactamase on graphene. The surfaces were incubated in 1 nM protein solution for 10 minutes.

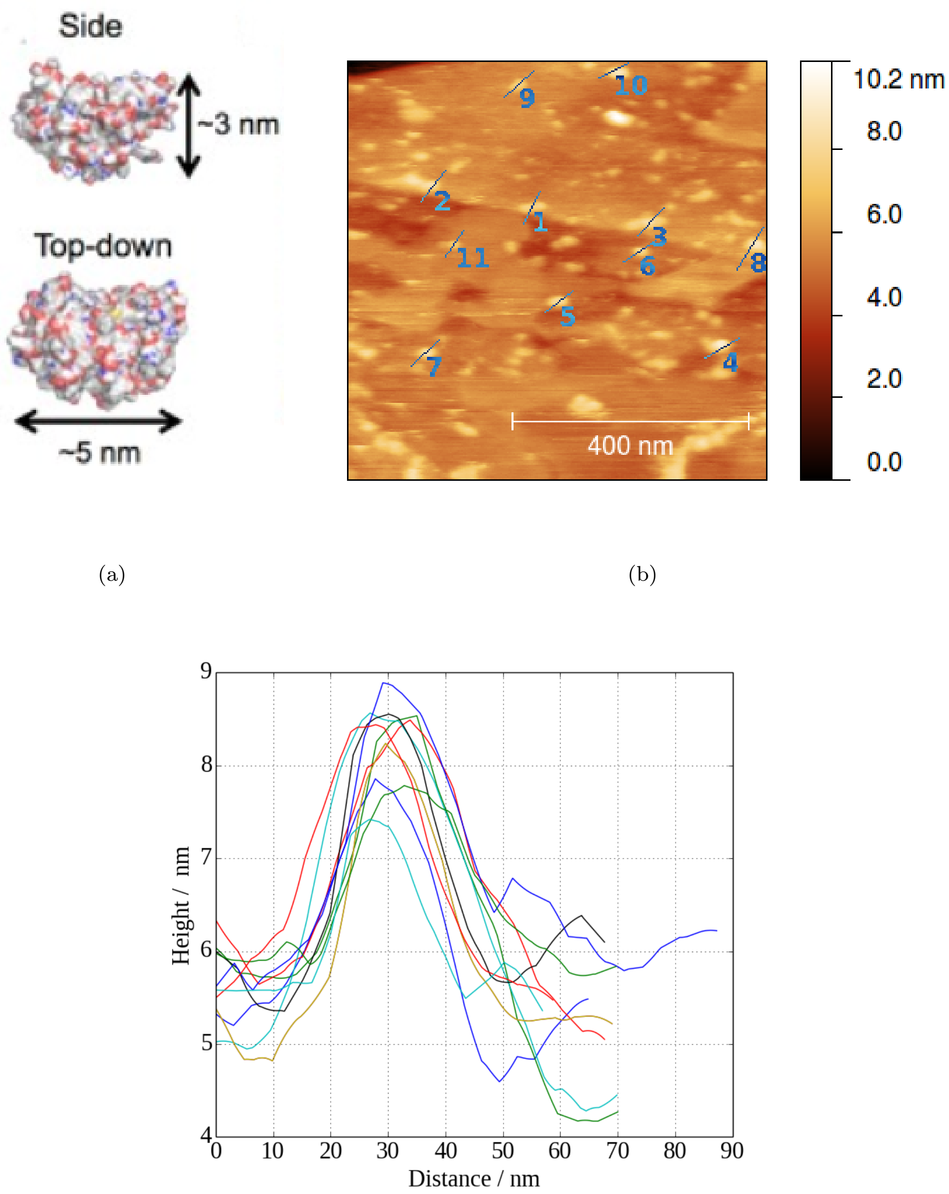

(a)

(b)

(c)

FIGURE 4.10: TEM with pyrene. (a) The structure of the TEM protein. (b) Modified TEM on graphene. (c) height cross section image to show the dimensions of single molecules.

The surface was imaged after the first and tenth scan. The protein images are initially poorly defined, presumably due to weak surface binding, and become even less defined as the proteins are spread across the graphene surface by AFM scanning. The clarity of the images is also deteriorated after multiple scans due to tip contamination. This work on TEM adsorbed on graphene was published in Chemical Science [5].

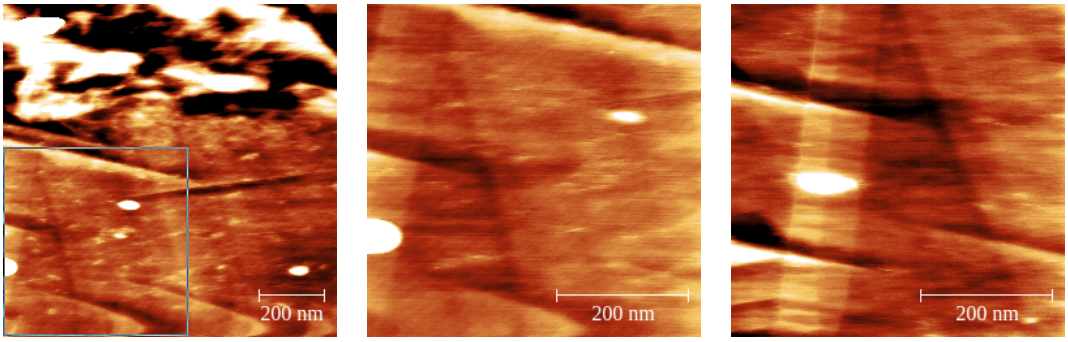

(a) (b) (c)

FIGURE 4.11: AFM imaging of wild type TEM on graphene, it shows that the proteins are not stable over multiple scans. (a) The selected area (z-range = -1.8-2.8 nm). (b) The first scan (z-range = -2.1-2.3 nm). (c) The tenth scan (z-range = -1.3-2 nm).

4.4.2.2 TEM105 Protein with Pyrene-Linker on Graphene Experiments

Similar experiments were carried out on another variant of the TEM protein, TEM105, where azF was positioned at residue 105 and then the pyrene was linked to it. Proceeding in this way, we achieved results similar to those obtained for TEM165. The following images were taken using AFM and STM for different engineered TEM concentrations, to verify the protein binding to the graphene surface and to find the most appropriate concentration for studying this type of protein deposited on the graphene surface. We used many concentrations in the range 0.5-0.001 μM. The graphene surface was fully covered by proteins at sufficiently high concentrations, but lower concentrations led to protein distributions more appropriate for the study of single molecule conduction.

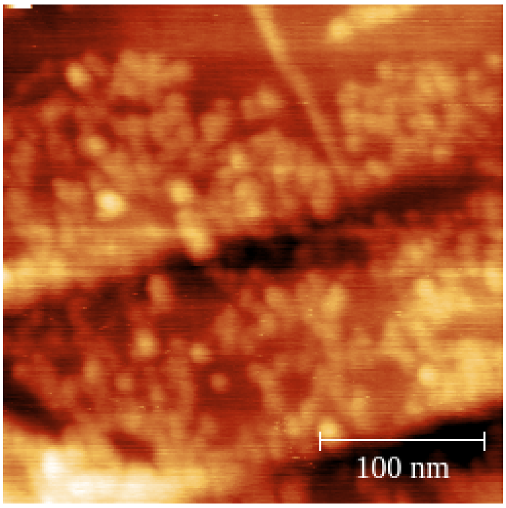

FIGURE 4.12: AFM image of pre modified TEM105 on graphene. The concentration was 0.005 μM and the sample was immersed in the protein solution for 10 minutes. The light dots represent the protein molecules on the graphene surface (z-range = -4.3-6.5 nm).

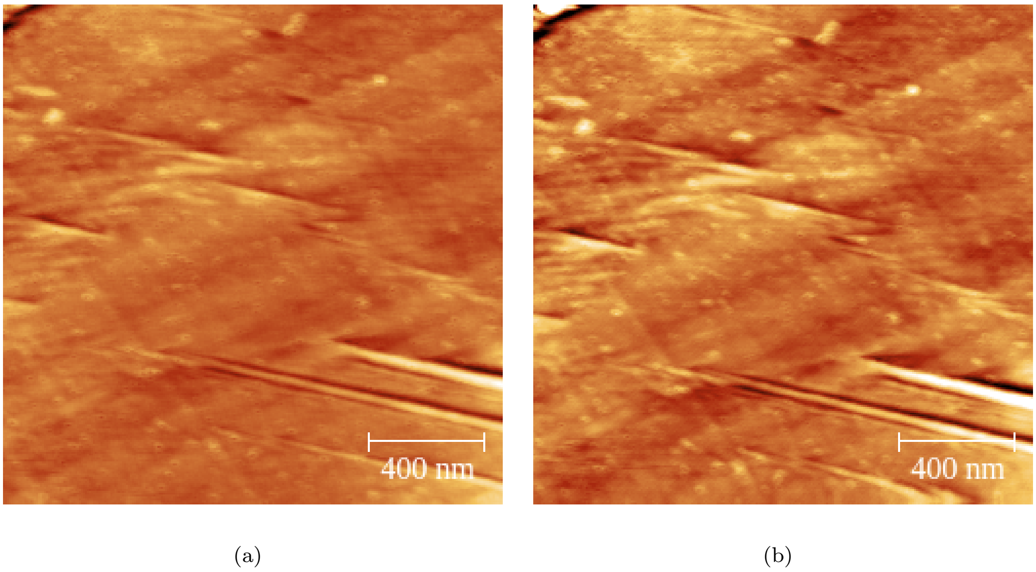

(a) (b)

FIGURE 4.13: AFM imaging of pre modified TEM105 with pyrene-linker on graphene. Concentration= 0.001 μM, incubation time = 10 minutes. The images show that the protein molecules are stable over many scans. The light dots represent the protein molecules on the graphene surface. (a) The 1st scan (z-range = 0-11.6 nm). (b) The tenth scan, (z-range = 2.2-9.8 nm).

Figure 4.12 shows the topography of the surface after deposition of TEM105 pre modified with pyrene. The low concentration 0.005 μM produced a sparse distribution of the proteins on the graphene surface, thus enabling the contact of the tip with individual molecules.

For TEM105 pyrene, we used a concentration of 0.001 μM and performed multiple scans to test the stability of the proteins on the surface. After ten AFM scans the protein molecules were still stable on the surface, as is shown in Figure 4.13. In the protein engineering, the position of pyrene on the protein was established with high accuracy, thus enabling efficient linking of the protein to graphene at the desired positions. Clearly, our approach can be usefully applied to other systems and provide functionalized graphene surfaces for a variety of nanotechnological applications (e.g., in biosensing devices and enzymatic biofuel cells with carbon-based electrodes).

To investigate the electronic properties of proteins on graphene, we tried imaging them with STM. Figure 4.14 shows the STM images of TEM105 and TEM165 proteins on graphene respectively, TEM165 is the same type of protein which we used before, but in the present system azide Phenylalanine(AZF) is attached at the position 165, while AZF was at position 105 in the previous system. The difference in structure between the two systems is expected not to have any effect on imaging, but the electrical measurements on these two proteins may differ. Note that we attached many protein molecules to the graphene surface, but the STM imaging was not able to visualize the proteins in most of the studied systems.

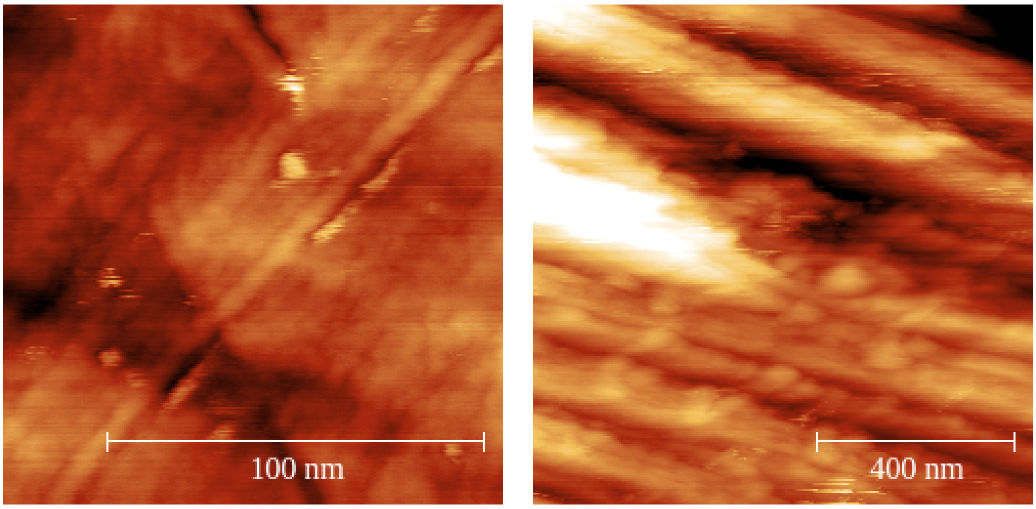

(a) (b)

FIGURE 4.14: STM imaging of TEM proteins with pyrene on graphene, concentration=0.005 μM, incubation time=10 minutes. (a) TEM105 (z -range= 0-7.9 nm), (b) TEM165, (z -range= 9.1-11.1 nm).

in summary, the AFM imaging was successful for the pyrene-modified TEM105 proteins on graphene, and a good distribution of single protein molecules on the substrate was observed at a concentration of 0.01 μM. We observed lateral dimensions of about 10 nm, which are higher than the real dimensions. Such an overestimate, can be due to the size of the tip. The height of the molecules was between (1.5 and 2.0) nm, which is comparable to TEM dimensions when they are measured by STM. From the above figures, one can see that many proteins can be attached to graphene via pyrene for concentrations not lower than 0.001 μM.

4.4.2.3 Experiments on cyt b_{562} with short-Linker Pyrene on Graphene

In engineering proteins, azF residue was inserted at specific positions: position 50 for the long-axis variant and position 5 for the short-axis variant. Click chemistry was used to click the pyrene with azF. Copper-promoted azide-alkyne cycloaddition (CPAAC) was used to attach pyrene directly to azF without linkers, thus obtaining what we call short-linker pyrene. In the experiments, we tested different concentrations of cyt b_{562} proteins with short-length pyrene, and we achieved optimal functionalized graphene for single-protein study at 0.005 μM concentration and the time of immersion was 10 minutes. The experiments allowed us to demonstrate the effects of the pyrene length on proteins anchoring to graphene, as shown in the following figures. Figure 4.15 shows separate proteins on graphene. The molecular distribution on the carbon surface enabled our study of the conduction through single molecules.

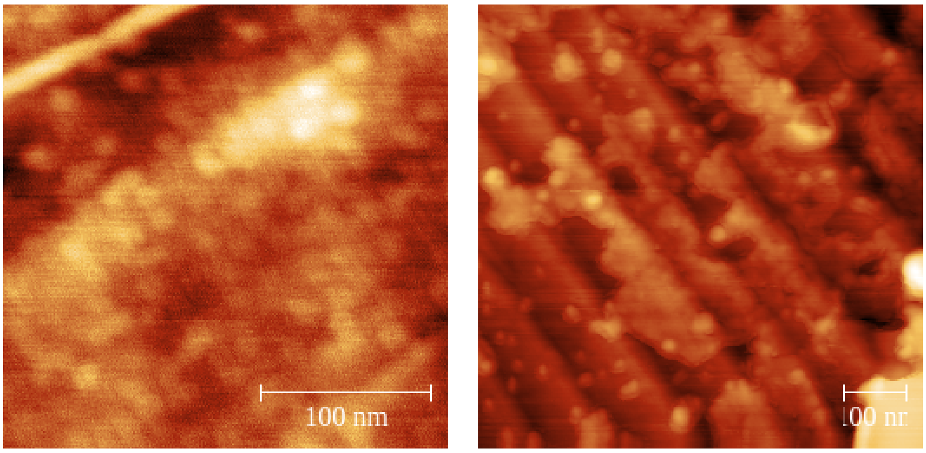

(a) (b)

FIGURE 4.15: AFM images of cyt b_{562} with short length pyrene on graphene. The light dots represent the protein molecules on the graphene surface. (a) The SH-SA variant, at a concentration of 0.005 μM , was incubated for 5 minutes by immersion (z-range = 0-5.1 nm). (b) The SH-LA variant, at a concentration 1 μM, was incubated for 10 minutes by drop cast method (z-range = 0-24.9 nm).

We made many attempts to observe the proteins on graphene samples by means of STM. Proteins were successfully imaged in only a few scans (may be because of the small differences in conductance from the area around the molecules). AFM imaging were successfully conducted on cyt b_{562} with short length pyrene. The observed lateral dimensions of 5 nm and height of 2.6 nm are comparable with the expected dimensions for such proteins from x-ray crystallography.

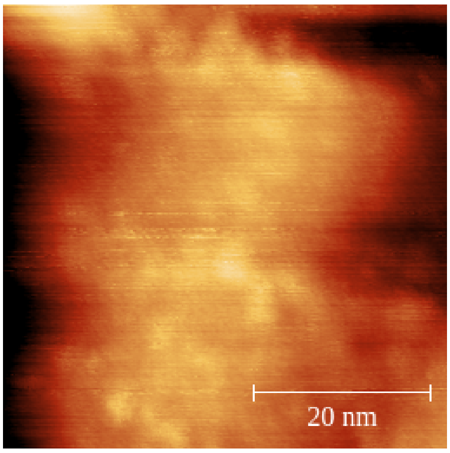

FIGURE 4.16: STM image of cyt b_{562} with short length pyrene on graphene, concentration=0.005μM, incubation time = 5 minutes by immersion, set point current = 0.05 nA, bias voltage = -0.05 V (z-rang = -5.5-4.3 nm).

4.5 UV experiments on graphene functionalized with proteins

We developed a new method to link proteins to the surfaces of carbon allotropes. Since the engineered TEM and GFP proteins carry the azF moiety, reactive nitrene species are formed (as molecular nitrogen is lost) when this residue is irradiated with UV radiation with wavelength below 310 nm (see Section 2.5.3). Several reactions can be photoinduced, including reduction and insertion into carbon-hydrogen bonds or into carbon-carbon double bonds. This reactivity was exploited in our systems to covalently linking proteins to graphene surfaces, after incubating the graphene substrates in protein solutions and irradiating with UV light to activate the azF residue. Thus, our novel approach enables protein linking to the carbon surfaces without need for use of additional linkers.

4.5.1 Sample Preparation

Protein samples were deposited on graphene (adsorbed on copper foil substrates) from the graphene supermarket. Bonding to graphene was provided through covalent linking of the proteins, that was stimulated by UV irradiation. The foil pieces (4×2 mm) were immersed in PBS containing 10, 5, 2 and 1 nM TEM protein with azido group, at position 105 and 165 or sfGFP with azido group at position 204, and incubated at room temperature for 10 minutes in the dark. After the incubation, the foil pieces were rinsed with high purity deionised water and dried under nitrogen flow. The same procedure was applied to other substrates, but with UV irradiation by a UVM-57 handheld UV lamp (302 nm, 6 Watt) during the incubation time. All the experiments were carried out in a closed chamber under nitrogen flow keeping the relative humidity between 7% to 11%. While preparing the samples, the chamber was shielded from the ambient UV. AFM imaging was performed using a Veeco Nanoscope IIa (Bruker) in tapping mode. The imaging of different regions on the graphene surface allowed us to study the distribution of the proteins. Density calculations of molecules from many AFM images for each sample were performed. The density was calculated by means of a python program written by Dr. Martin Elliott, this was used to achieve the density data for different small areas around 1 μM in size. The experiments were repeated many times and density histograms were produced for all samples, since the distribution of the molecules was not homogeneous on the surface. These histograms were used to compare the densities of molecules adsorbed on graphene from the UV irradiation experiments and dark experiments. GFP and cyt b_{562} proteins were similarly engineered and used in similar experiments to test the new approach for different types of proteins on graphene.

4.5.2 Results and Discussion

4.5.2.1 UV Experiments of TEM and sfGFP on Graphene

Experiments were performed on different types of proteins to anchor them to graphene surface using the UV irradiation method.

Figure 4.17 shows the AFM results for TEM105-azF in the dark and under UV irradiation. We observed inhomogeneous protein coverage, which is due to the graphene as we discussed above. The protein coverage is much greater for the UV treated samples than for the dark samples. This indicated that the assembly of proteins using UV irradiation was successful. This is an elegant approach to immobilize proteins on to substrates such as graphene, without need for decorating the surface with any linker or gold clusters.

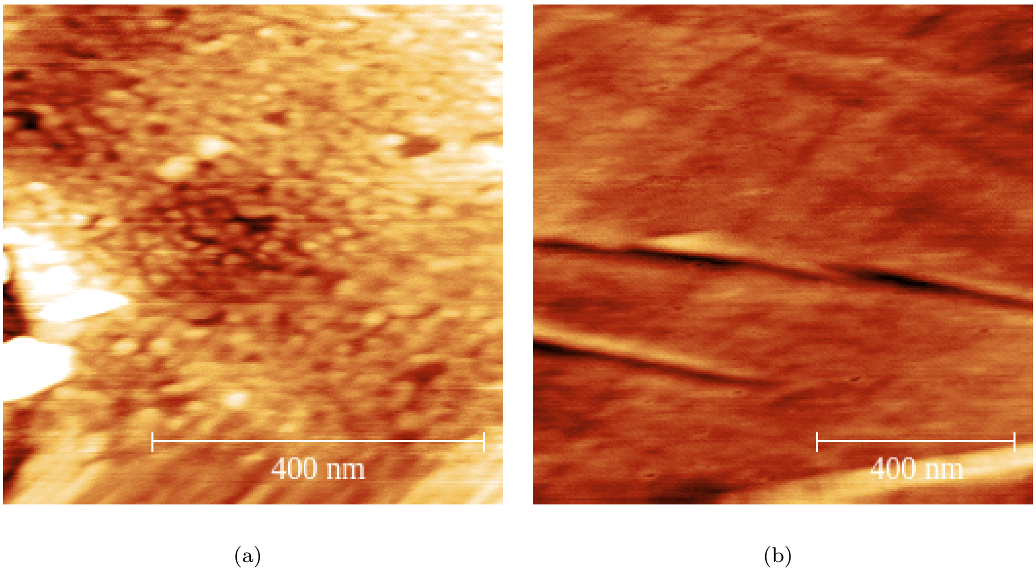

(a) (b)

Figure 4.17: AFM images of TEM105azF on graphene. Concentrations of 10 nM, incubation time of 10 minutes. (a) The sample prepared under UV irradiation. The light dots represent protein molecules on graphene surface (z-range = 0-5.0 nm). (b) The sample prepared in the dark. The image shows the bare graphene surface without protein molecules attached (z-range = 0-5.0 nm).

The high concentration did not allow to distinguish individual proteins, and the variation in apparent size probably indicates the presence of molecular clusters. Statistical analysis on the topology of the immobilised proteins were conducted. The protein heights turned out to be around 1-2 nm. All the concentrations used consistently showed efficient protein attachment under UV irradiation. We applied successfully the same approach to TEM165-azF. The results were similar to those obtained for TEM105-azF on graphene. The UV method gave a high distribution of proteins anchored to the graphene surface. However, some samples prepared in the dark showed a few proteins, which can be due to the affinity of the proteins to defects on the graphene surface (see Figure 4.18). The measured apparent heights were around 1-1.5 nm.

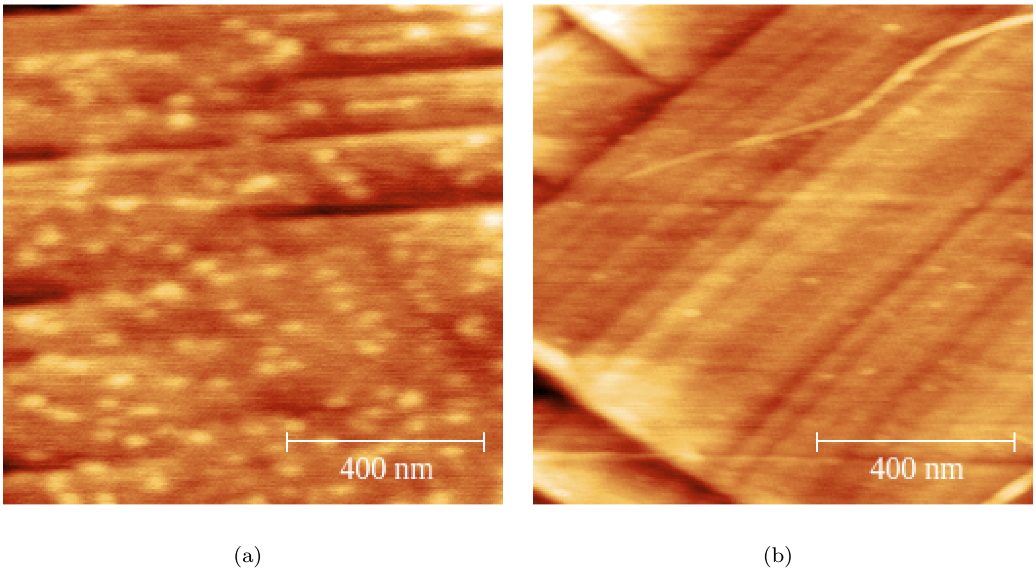

(a) (b)

Figure 4.18: AFM images of TEM165-azF on graphene. Concentration = 5 nM, incubation time= 10 minutes. (a) The sample prepared under UV irradiation. The light dots represent protein molecules on graphene surface (z-range = 0-6.5 nm). (b) The sample was prepared in the dark. The image shows the bare graphene surface with few protein molecules attached (light dots) (z-range = 0-9.0 nm).

On the other hand, sfGFP is readily immobilized on graphene using the UV approach. The azide was introduced at position 204 in this protein. Images of the protein immobilization on graphene are reported in Figure 4.19. The protein concentration used in this experiment was 1 nM. The figure shows a clear difference between the results from the samples incubated in the dark and with UV exposure. These results clearly demonstrate that sfGFP204-azF does bind to the mono-layer graphene under the preparation conditions employed and that the photochemical insertion process was successful in obtain protein anchoring to graphene. Individual proteins can easily be imaged for this concentration and are fairly uniform in apparent size. Typical heights observed are around 2 nm.

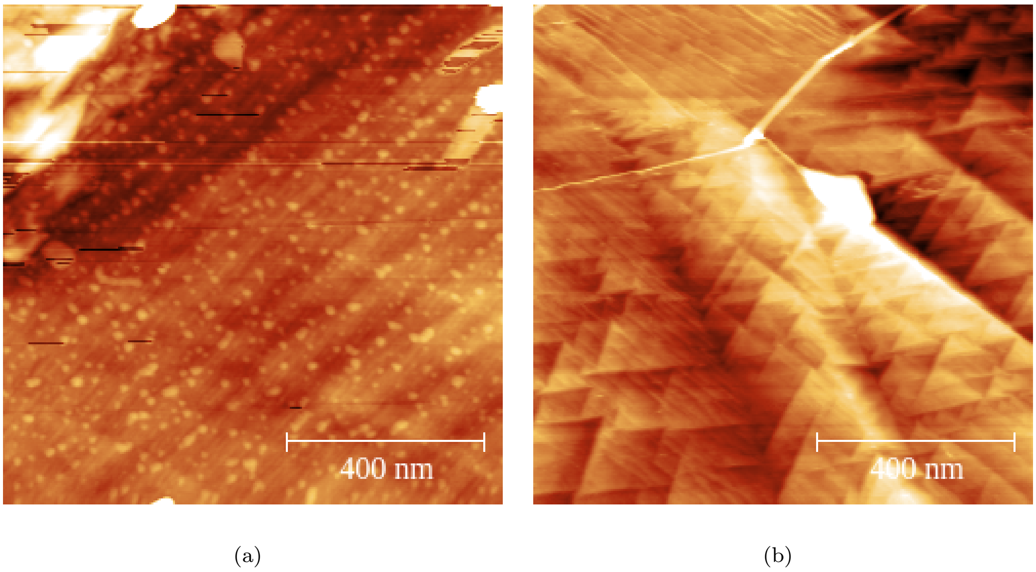

(a) (b)

Figure 4.19: AFM images of sfGFP204-azF on graphene, concentrations of 1 nM, incubation time = 10 minutes. (a) The sample prepared under UV irradiation (z-range= 0-15 nm). (b) The sample prepared in the dark (z-range = 0-15 nm).

4.5.2.2 Using UV approach to link Cyt b_{562} on Graphene

The same approach was used to attach cyt b_{562} to graphene. Several concentrations of the Cyt b_{562}-azF LA protein and rinse times were used. We compare the samples prepared in the dark and under UV irradiation. UV samples showed many more proteins attached than the dark samples. However, some proteins were attached the graphene surface for the dark samples. For these experiments AFM imaging was performed over many different areas on the surface to take into account the inhomogeneity of coverage across the graphene, and to get enough statistics for density measurements analysis. Figure 4.20 shows the AFM results of the 5 nM concentration. The heights observed are around 2 nm, which is a little smaller than the smallest 2.5 nm dimension of cyt b_{562}, but considerably smaller than the maximum dimension of 5 nm. Figure 4.21 shows the STM image of this type of protein on graphene prepared under UV irradiation and the heights observed are around 2 nm as it is seen from the cross section image. Density histograms were plotted to compare the distribution of proteins in both dark and UV cases (see Figure 4.22). The results were in agreement with the previous results on other proteins, since the UV samples showed higher density of molecules attached to the graphene surface than the dark samples.

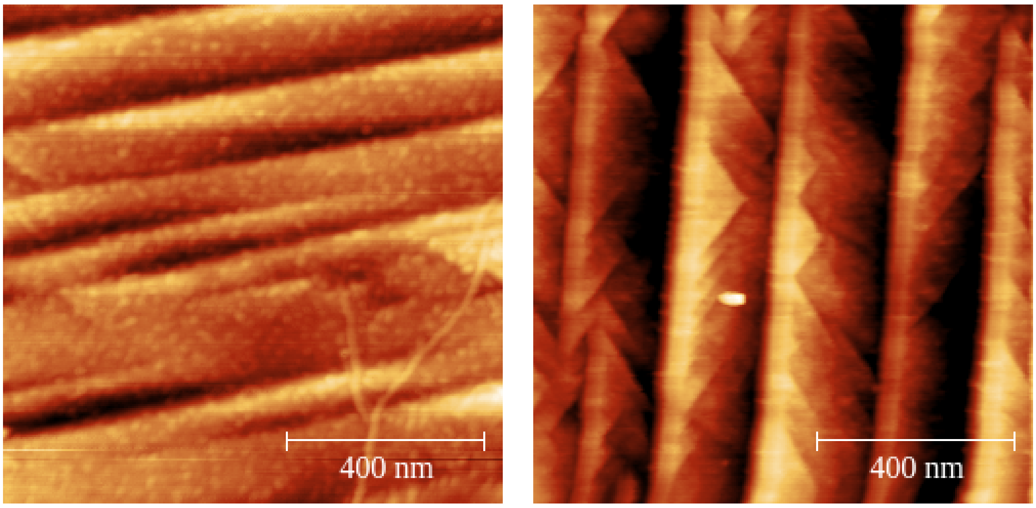

(a) (b)

FIGURE 4.20: AFM images of Cyt b_{562}-azF on graphene, concentration = 5 nM, incubation time = 10 minutes. (a) The sample prepared under UV irradiation (z-range = 0-15 nm). (b) The sample prepared in the dark (z-range = -5-10 nm).

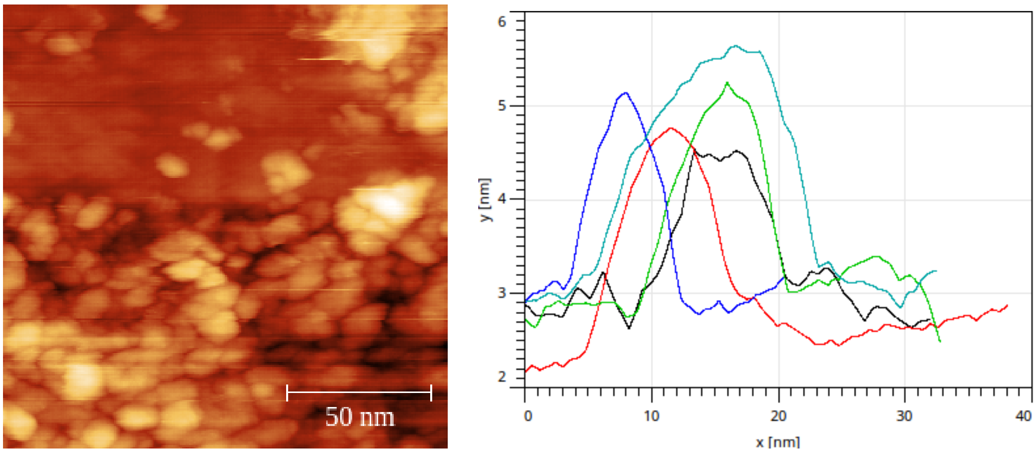

(a) (b)

FIGURE 4.21: Cyt b_{562}-azF LA50 on graphene prepared under UV irradiation, concentration of 5 nM, incubation time = 10 minutes. (a) STM image, bias voltage = 0.02 V, set point current = 0.05 nA (z-range = 0-8.3 nm), (b) Height cross section of individual molecules.

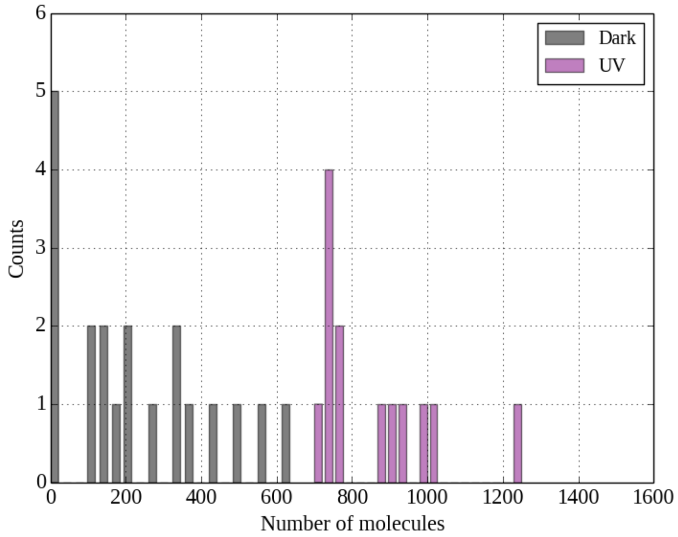

FIGURE 4.22: Histogram of cyt b_{562} molecules distribution on graphene for samples prepared in dark and under UV irradiation.

The UV-exposed samples were strongly attached to the graphene surface, as evidenced by multiple imaging (see Figure 4.23). This is consistent with the fact that UV exposure results in binding of the molecules. On the contrary, in the dark the protein attachment was weaker and the AFM tip was increasingly contaminated during the imaging, which means that the few molecules non-specifically bound in the dark were disrupted by the tip.

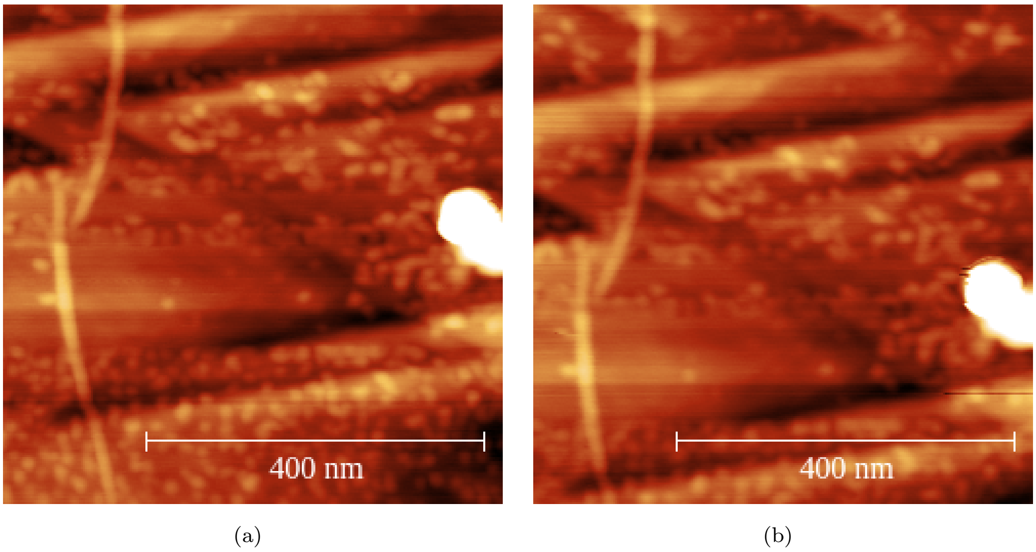

(a) (b)

FIGURE 4.23: AFM images of cyt b_{562}-azF on graphene, concentrations = 0.005 μM, incubation time = 10 minutes prepared under UV irradiation. AFM images of 0.59 μM squares show the proteins are robust to multiple scans. (a) The 1st scan (z-range = 0-15 nm), (b) the 10th scan (z-range = 0-10 nm).

Additional evidence of covalent protein attachment was obtained by taking Raman spectra of the surfaces, shown in Figure 4.24. Raman measurements were performed by our collaborators in Exeter university. From the Raman spectra, we can recognize three prominent features in each sample: the strong $G\prime$ (also denoted 2D) band centred around 2677 cm^{-1} , the G band around 1585 cm^{-1} , and a rather weak disorder-induced D band at around 1343 cm^{-1} . The sharp peak around 2335 cm^{-1} is due to atmospheric molecular nitrogen [110].

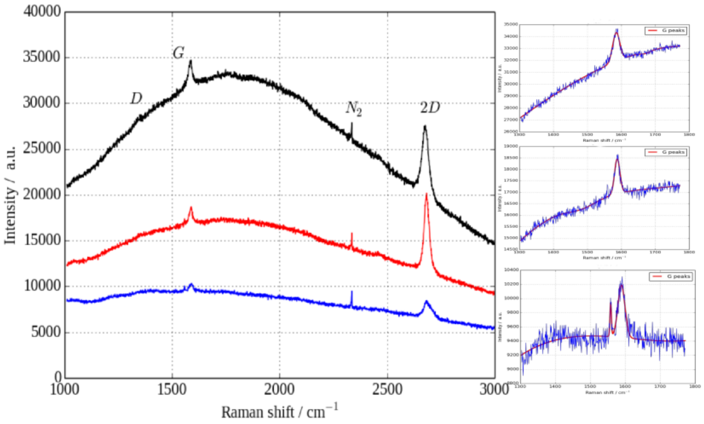

FIGURE 4.24: Raman spectrum for cyt b_{562} azF samples on graphene. Black curve: pristine graphene. Red: sample prepared in the dark. Blue: sample prepared under UV irradiation. The three side figures show the small side peak below the G peak. In each case, the red line represents the fitting. The top figure is for pristine graphene, the middle one was obtained for the dark sample, and the bottom one refers to the UV sample.

There is a consistent overall decrease in Raman intensity in the protein-treated samples, particularly after UV treatment. The 2D/G ratio is strongly reduced for the UV-treated sample, as expected because of doping of the graphene through linking to the azide group (see Figure 4.25). In fact, it is known that the decrease in the 2D/G ratio indicates the occurrence of nitrogen doping of graphene [111–114]. Consistent with this, the 2D peak is upwards from (2677 ± 0.11) cm^{-1} for pristine graphene to (2688 ± 0.29) cm^{-1} for the UV-treated sample, which indicates the graphene doping [114, 115]. Finally, the appearance of a small sharp peak below the G band can be due to the covalent bonding of the proteins with graphene surface [116].

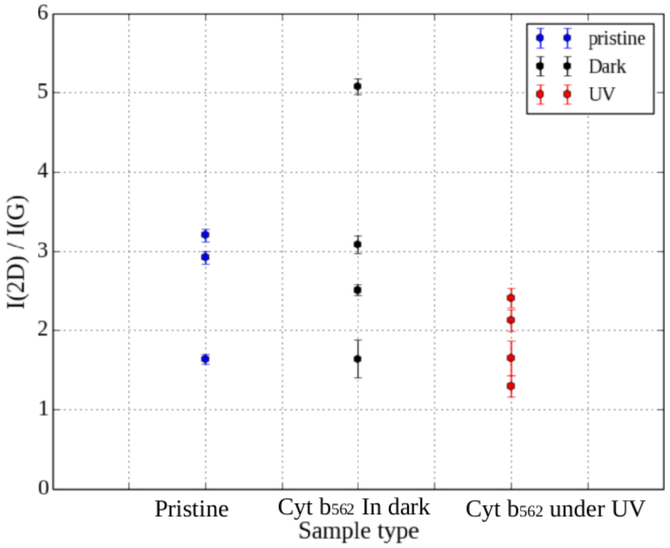

FIGURE 4.25: The ratio of 2D peak over G peak for different samples (sample of cyt b_{562}azF on graphene under UV, the sample of cyt b_{562}azF on graphene in dark and pristine graphene).

The D peak around 1350 cm^{-1}, appeared clearly in the UV sample areas but not for the pristine and dark samples. This peak originates from defects in the graphene structure. In fact, the protein covalent linking introduced some defects into the structure, in as much as C=C double bonds are broken [116]. The D peak indicates structural disorder. It is common for as-prepared graphene not to have enough structural defects for the D peak to be Raman active, so that it can only be seen at the edges of the graphene sheet [117]. The D peak appears in the Raman spectrum of graphene doped with nitrogen due to the consequent disturbance of the graphene structure [111]. We observed a shift in 2D and G peak positions, as it is illustrated in Figure 4.26. This effect is common when doping graphene substrates. There was no change in the peaks width for all samples, instead (see Figure 4.27).

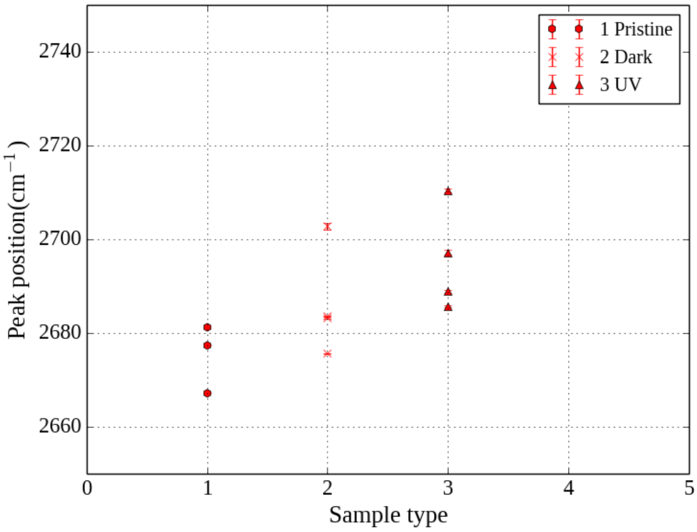

(a)

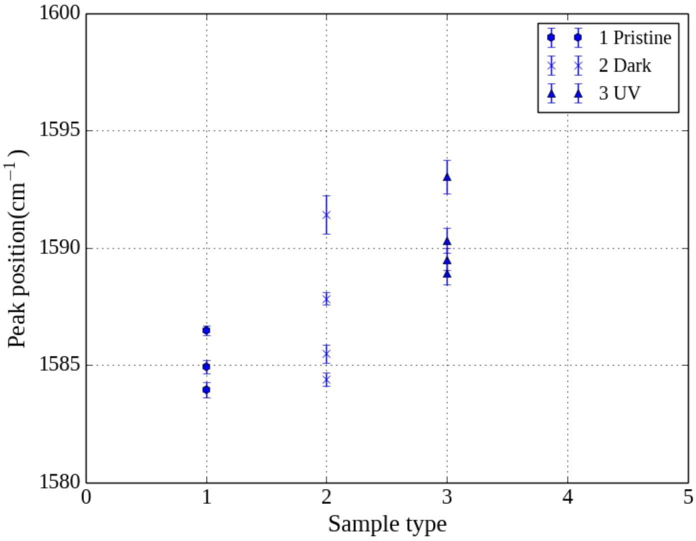

(b)

FIGURE 4.26: Peak positions for different samples. (a) 2D peak position, (b) G peak position.

The presence of doping is clear from the considerable change in 2D/G ratio, the G-band and the 2D-band. And in particular, the side peak near the G peak, which did not appear only when UV was used. All of these variations reveal clear effects of nitrogen doping, in agreement with Ref. [118], and contribute to demonstrate the successful direct linking of proteins to graphene via UV irradiation.

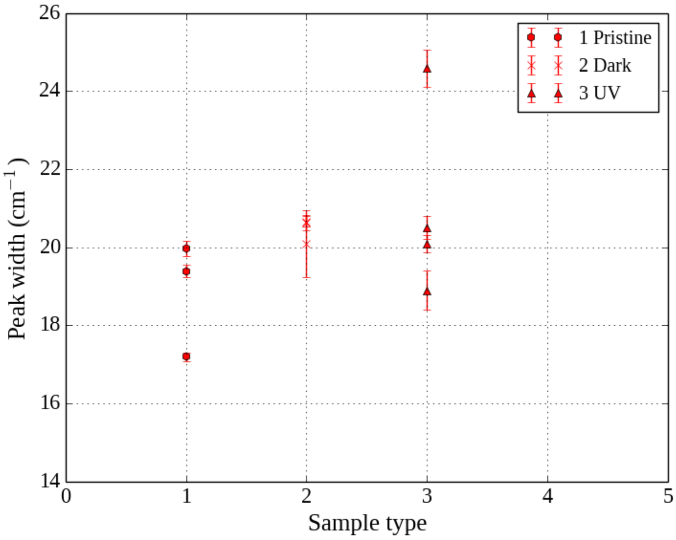

(a)

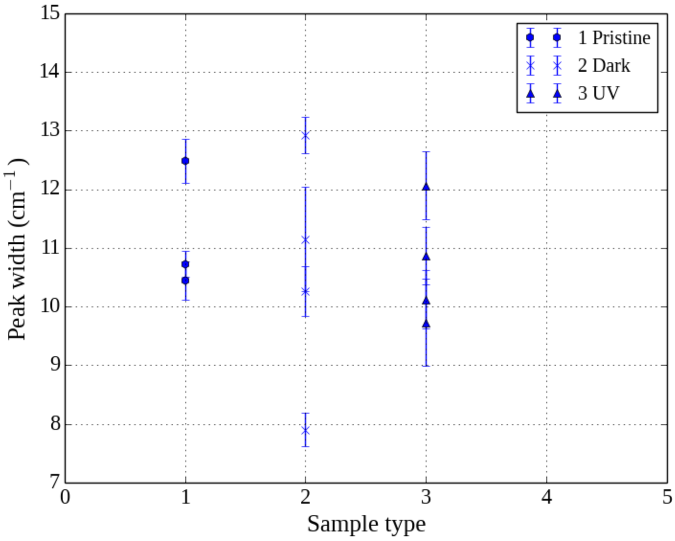

(b)

FIGURE 4.27: Peak width for different samples. (a) 2D peak width. (b) G peak width.

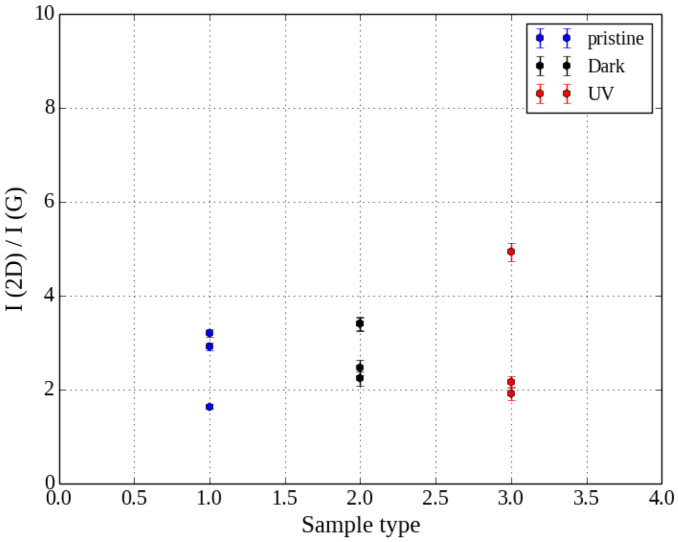

FIGURE 4.28: The ratio of 2D peak over G peak for sfGFP204 on graphene (UV sample and dark sample) and of pristine graphene sample.

The same Raman experiment was performed on sfGFP204 proteins on graphene and the results for the 2D/G ratio is shown in Figure 4.28 and Figure 4.29 shows the peak positions for different samples while 4.30 demonstrates the peaks width for the pristine graphene, UV and dark samples.

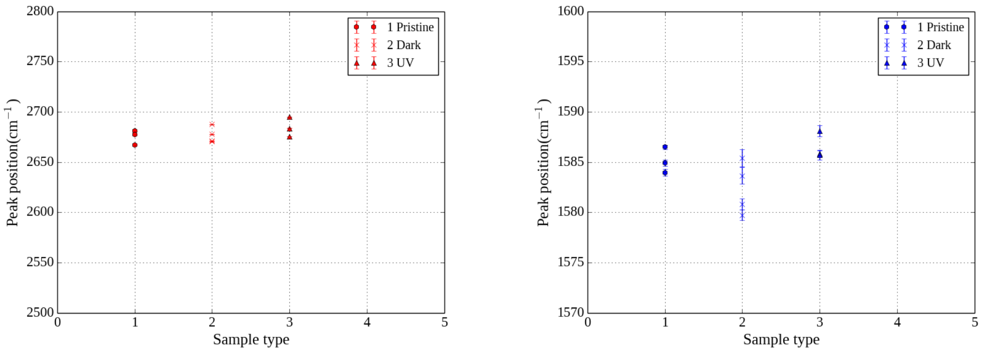

(a) (b)

FIGURE 4.29: Peak positions for different samples to compare sfGFP204 samples prepared under UV and in dark with the pristine graphene sample. (a) 2D peak position, (b) G peak position.

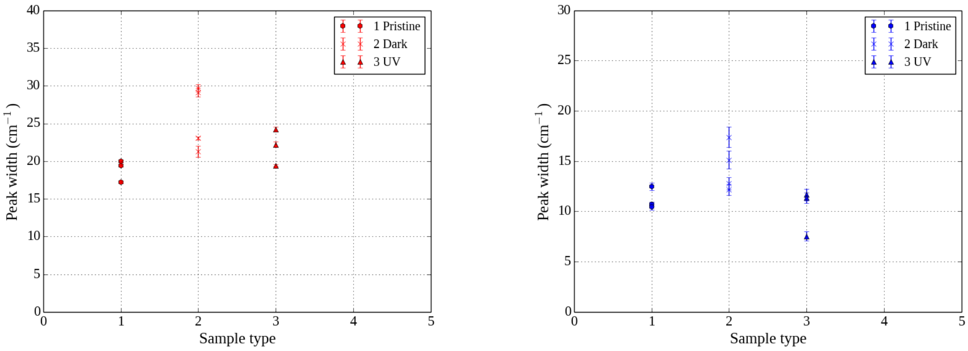

(a) (b)

FIGURE 4.30: Peak width for different samples samples to compare sfGFP samples prepared under UV and in dark with the pristine graphene sample. (a) 2D Peak width. (b) G peak width.

All the results from the Raman measurements for the sfGFP204 are in agreements with the Raman results of cyt b_{562} which strongly demonstrates that the UV approach is working successfully with different protein molecules, this method of immobilisation results in doping the graphene which is clear from the Raman analysis.

4.5.2.3 Resistance Experiments

Other evidence of protein covalent attachment to graphene was obtained by performing resistance measurements. This is another way to investigate the linking of proteins to the graphene surface by means of the UV approach which was illustrated in the previous section. Molecular adsorption alters the structural and electronic properties of the graphene. Moreover, electron transfer to/from the molecule can change the density of carriers in graphene. In fact, it has been shown that doping graphene with electron-donor or acceptor molecules affects the resistance of the graphene sheet [119, 120]. Therefore, the resistance measurements also contribute to investigate graphene doping. In this thesis work, we developed a method to attach proteins to graphene by means of UV irradiation. The photo-response of the graphene after protein deposition was investigated using different proteins and was compared to that of pristine graphene samples. Four-point probes

[121, 122] were used in our work for local and non-destructive measurements of the graphene resistance.

4.5.2.4 Sample Preparation and Experimental Setups

Protein samples were deposited on CVD graphene, which was lying on an insulating SiO_2/Si(p-doped) substrate. The samples were purchased from Graphene Supermarket. Bonding to graphene was obtained through covalent linking of the proteins, which was stimulated by UV irradiation as in our previous UV experiments (section 4.5). The samples (10 × 10 mm) of specimens were mounted on a two 6-pin leadless chip carrier and connected by gold wire of diameter 0.25 μm. The bonded samples were loaded into a pin breakout board, which was connected to an AC source and to a lock-in amplifier to measure the output voltage. This set-up allowed us to measure the resistance of the graphene sheet using the Van der Pauw method: four contacts were made on graphene samples, we produced an AC current between two contacts of the graphene sample and measured the output voltage between the other two contacts. The resistance of the graphene sheet was measured for 10 minutes. Then 1 μM solutions of sfGFP204 or cyt b_{562} proteins with azido group, at position 204 for sfGFP and position 50 for cyt b_{562}, were dropped on the sample and left there for 20 minutes in dark. Next, the sample was exposed to UV from a UV diode (wavelength 305 nm) for 30 minutes, whereupon the diode was switched off and the sample was allowed to relax. During all these steps, the resistance was measured automatically using a Python program.

The same procedure was applied to other substrates with just buffer for comparison. All the experiments were carried out in a closed chamber under nitrogen flow, keeping the relative humidity between 1% and 2% to prevent oxidation from happening, which can affect the resistance measurements. While preparing the samples, the chamber was shielded from the ambient UV. The experiments were repeated many times. GFP and cyt b_{562} proteins were similarly engineered and used in similar experiments to test the new UV-based anchoring approach for different types of proteins on graphene. A Python script was used to read an input file specifying the measurement parameters for a single measurement and to calculate the sheet resistance using the Van der Pauw formula.

Preliminary experiments were also performed with the same set-up, to measure the photo-response of the prepared samples after they dried out. In fact, we wanted to explore the integration of photo-active proteins to create hybrid materials with photo-responses using desired wavelength. The samples were measured in the dark and when exposed to light of wavelength 305 nm for alternate time intervals of 10 minutes each. A step shape behaviour is observed for illumination with 305 nm for sfGFP204 samples but not for the other samples which were pristine graphene, buffer and cyt b_{562} samples.

4.5.2.5 Results and Discussion

In Figure 4.31 we show the effect of UV on the sample which was prepared with sfGFP204 azF proteins and Figure 4.32 shows the sample which was prepared with buffer, in order to compare the two samples, and to demonstrate the effect of the UV irradiation in the presence of the proteins. Both figures show the resistance measured in the dark, when adding the solution, and then when exposed to a UV light of 305 nm, at an intensity of 8.7 W/m^2.

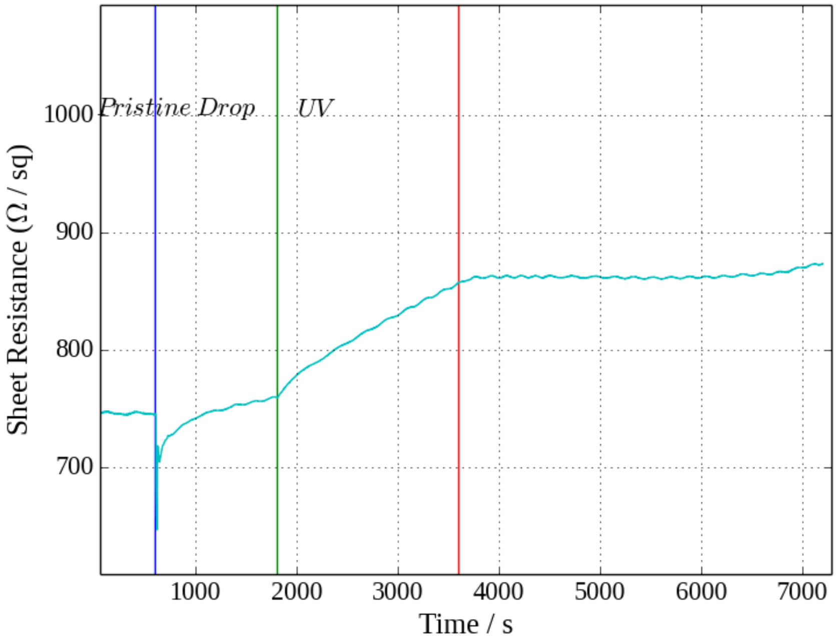

FIGURE 4.31: The sheet resistance as a function of time during the incubation of the graphene sample with sfGFP204-azF protein solution, the used concentration = 1 μM.

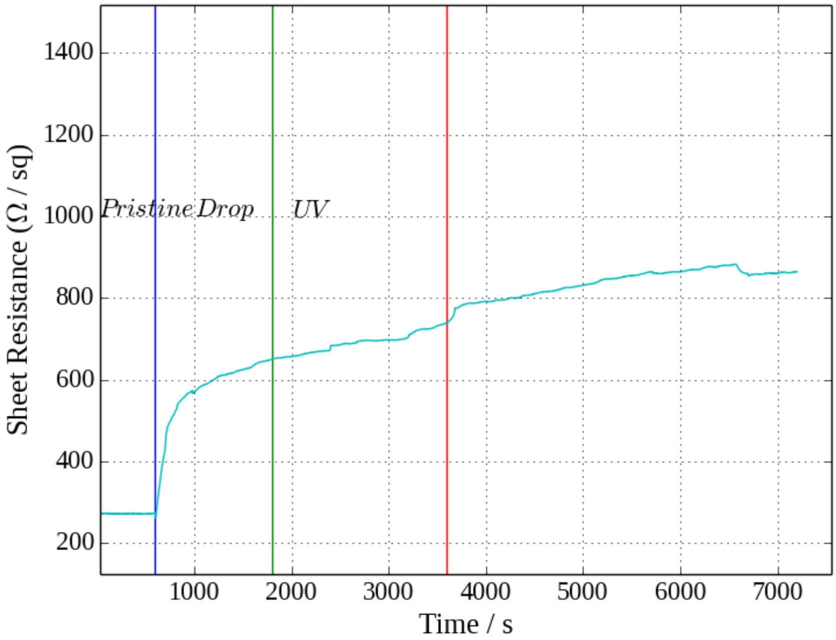

FIGURE 4.32: The sheet resistance as a function of time during the incubation of the graphene sample with buffer.

In both cases, a change in resistance was observed when adding the solution drop, which can be due to the liquid-surface interface experienced by the graphene, which is offset by the potential drop over the electrical double layer in solution, that is associated with negative surface charge [123]. A significant change in resistance was observed when illuminating with UV for the protein sample (as it is shown in Figure 4.31), while there was no effect of UV irradiation for the buffer sample. This important result was consistently confirmed by many experiments. After switching the UV off, for some samples the resistance continued to increase before achieving a plateau. The amount of further increase and the plateau value of the resistance changes from a sample to another. In the case of the buffer sample (Figure 4.32) we can see an increase in resistance during the experiment but the UV irradiation has no effect there. We noticed that when the samples are dry the sheet resistance of the buffer sample turns out to be almost the same as that of the pristine sample (which is around 200-1000 Ω/sq) before starting the experiment, while for the protein sample the resistance stays at a higher level, around 3000-3500 Ω/sq.

This result gives another confirmation that the UV approach is successful. In fact, the activation of the azide is stimulated by the UV, the linking of the proteins to the surface disturbs the graphene structure and thus changes the electronic properties of the surface, as demonstrated here by the dramatic change in resistance.

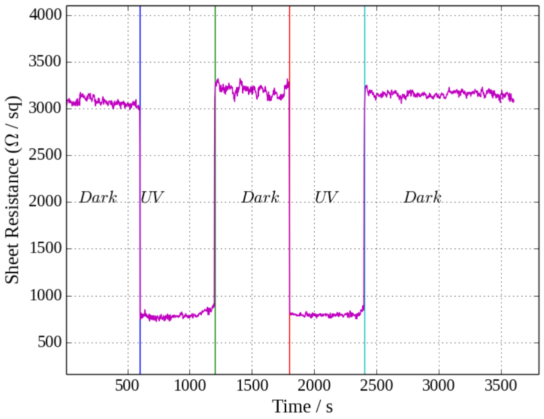

(a)

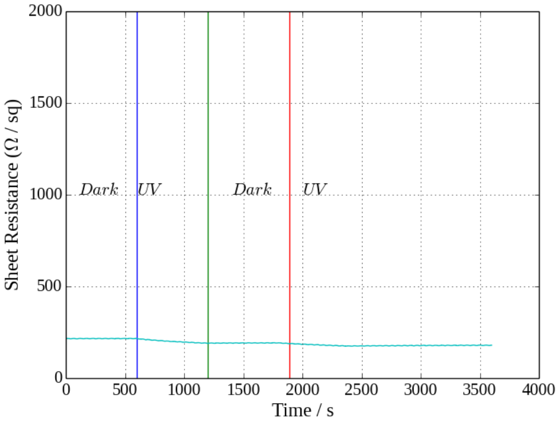

(b)

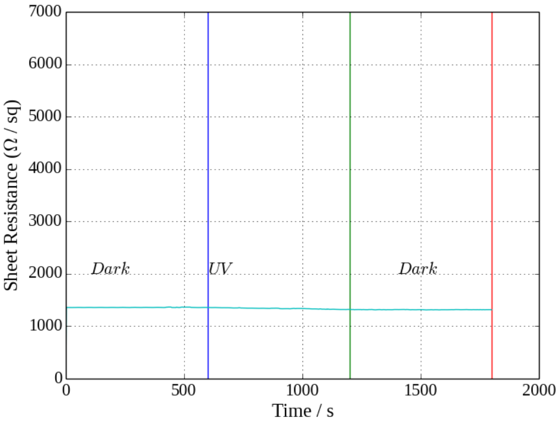

(c)

FIGURE 4.33: Photo response of dry samples illuminated by UV of 305 nm wavelength. (a) sfGFP-azF sample, (b) Pristine graphene. (c) Buffer sample.

Another experiment was performed to study the effect of the UV radiation on the dry samples. A significant (dramatic, indeed) change is observed only for sfGFP204 azF protein samples irradiated with UV of 305 nm wavelength , which is the same wavelength that was used to stimulate the protein linking to the surface (see Figure 4.33). We observed minor changes in resistance for the pristine graphene (Figure 4.33 b) and graphene with buffer (Figure 4.33 c) samples instead (these behaviours agree with the trend observed in Ref. [124], although visible light was used in that work). The photoinduced conductivity switching in Figure 4.33 a can be ascribed to effects of UV on the photo-sensitive sfGFP204 protein, including charge redistribution in GFP upon photo-excitation, or GFP-graphene charge transfer (since GFP is reported to be a light-induced electron donor [125]) which causes increase in the conductance through graphene. Indeed, sfGFP shows appreciable absorption at the wavelength used as in Figure 4.34 [126]. Photocurrent was observed by Lu *et al.* [55] for a different graphene-GFP system and using different radiation wavelengths. Compared to the system in Ref [55], even over time intervals of comparable length upon UV irradiation, we observe a very stable and markedly reversible switching between two well-defined conductive states of our system. The specific reasons for the clear-cut conductance switching in Figure 4.33 a are subject of our ongoing and future investigation. Let us stress that the photo-response effect indicates as well that the proteins are still active after linking to graphene, which is a vital factor for the implementation of devices that exploit the molecular functionalities.

The photo-response of the sfGFP protein was checked over many days. We noticed an unchanged response during the first four days, while the response to UV illumination was decreasing in the fifth day and was non appreciable in the sixth day. Future studies will aim to determine whether such an evolution results from long-term instability of the functionalized graphene surface or from other occurring event involving the protein layer that alters its response to UV.

The same experiments as in Figures 4.31 and 4.33 were performed on cyt b_{562}-azF. While similar trends are seen in Figure 4.35 a, the photo-responses of the dry sfGFP and cyt b_{562} samples differ. In fact, the dry cyt b_{562} sample shows a very modest resistance dependence on UV. However, the resistance value in Figure 4.35 b is similar to that in the absence of UV in Figure 4.33 a, and both are much larger than the resistance of pristine. This means that, similarly to sfGFP, cyt b_{562} was successfully attached to graphene, but its conductivity is not sensitive to the presence of UV.

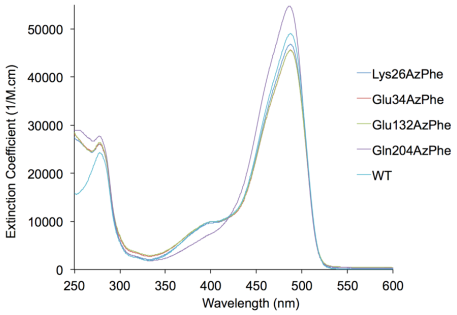

FIGURE 4.34: UV-visible absorption spectra of azF-sfGFP variants.

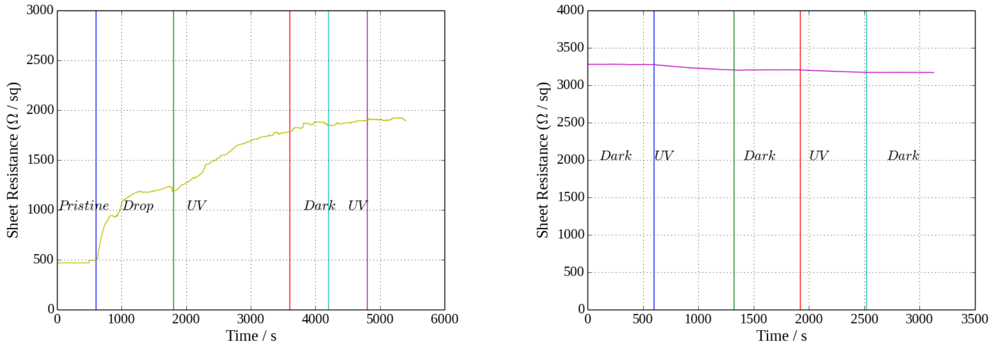

(a)

(b)

FIGURE 4.35: (a) The sheet resistance as a function of time during the incubation of the graphene sample with cyt b_{562}-azF protein solution, the used concentration was 1 μM. (b) Photo response of dry cyt b_{562} sample.

4.6 Conclusions

In summary, we developed an efficient method to functionalize graphene by means of UV irradiation and we widely investigated the success of the functionalization and the modified conductive properties of the resulting hybrid materials. Two techniques for attaching proteins to the graphene surface were successfully employed in this work, as was suggested by SPM imaging and Raman spectroscopy analysis and resistance measurements. The two methods were direct covalent bonding through UV irradiation and non-covalent bonding through pyrene group. These methods provide new feasible ways to investigate and use biological molecules on graphene, with potential for future nanoelectronic applications. Sample imaging with AFM was successful for all types of proteins which were engineered with pyrene on HOPG, although proteins were mostly not visible by STM (STM imaging was achieved for some proteins on graphene, but it was not reproducible in all cases). The AFM images showed that all of the engineered TEM, TEM-azF, sfGFP-azF and wild type TEM attached to the graphene surface, but with different distribution properties. The measured average lateral and height values for the molecular layer were approximately corresponding to the dimensions of the TEM protein. 0.005 μM turned out to be the best protein concentration to obtain separated (single) proteins on the graphene surface. The UV approach for anchoring the proteins to graphene was also validated by histogram analysis of the AFM images, as well as by Raman spectra collected for the sfGFP-azF and cyt b_{562}-azF samples and by resistance measurements on such systems.

The imaging by AFM and by STM were both successful for cyt b_{562}-azF and cyt b_{562} with short-length pyrene on graphene. Also for the cyt b_{562} proteins on graphene, 0.005 μM was the best concentration to observe single molecules. We have showed that the four-point probes can be used to perform resistance measurements on graphene and thus to provide extra evidence that our UV approach is successfully linking the proteins to graphene. We also showed for sfGFP samples that, after protein deposition on graphene, the electronic properties of the hybrid material can be manipulated by UV irradiation. This can have a big impact on future applications, such as photo detectors, because this type of protein is light sensitive and graphene has unique structural and functional properties. The observed consistent, dramatic and reversible decrease in resistance under UV (see Figure 4.33 a) for sfGFP samples demonstrates the possibility to implement photoinduced molecular electric switches using our approach to functionalize graphene. Future experiments related to this work will aim to study the photoswitching conductivity observed in Figure 4.33 at the radiation wavelengths of maximum absorption for sfGFP204.

Chapter 5

Holo and Apo Cyt b_{562} Proteins on Gold

5.1 Introduction

In this chapter, we describe our study of conduction through single SH-SA and SH-LA cyt b_{562} holo and apo-proteins adsorbed on Au(111) surface. This study was made possible by the ability developed in our group to target and measure individual protein molecules using the STM I-z technique. This ability is mainly the result of two main achievements: the construction of a low drift instrumentation and the development of protein engineering to anchor stably the molecules to the substrate [28]. This setup was used for some conductance measurements on holo-cyt b_{562} in the tip retraction mode [28]. In this study, we performed extensive measurements using the home-built STM setup, including both holo and apo-cyt b_{562} proteins, and using an environmental cell more recently built in our laboratory to enable conductance measurements under different conditions of humidity and temperature. Before passing to the description of the experiments, we wish to clarify the general context for the study in this chapter.

Conductance through single molecules can be measured by using scanning tunnelling microscopy (STM). This microscopy can also be used to study charge transport through small organic molecules [4, 127, 128]. The insertion of the anchoring groups at appropriate positions and the interactions among proteins enable their efficient self-assembling on gold (or other metal) surfaces. Electron transfer (ET) is an ubiquitous process of critical importance in many systems of relevance to biology, biochemistry and physics. The development of molecular electronics requires to understand and control the structural stability and the ET efficiency at molecule-electrode interfaces, as well as the effect of the solid state component on the functional charge dynamics inside the molecular system.

ET between biomolecular centres often occurs in the weak-coupling limit (Marcus non-adiabatic regime), because of the involved ET distances and the consequently small overlap between electronic states that are localized on the donor and acceptor molecular groups. Yet, the small intra or inter-molecular coupling allows for long-range communication via ET. At a redox biomolecule-electrode interface, the charge can be either localized in the biomolecule or transferred to the electrode, where it soon delocalizes (and it is swept away when a bias potential difference is applied). Tunnelling or resonant tunnelling can also take place through relatively small molecules between electrodes; and an average occupation of the molecular system can only be defined in such cases [1, 50].

Cyt b_{562} is an ET protein that shuttles electrons between neighbouring membrane cofactors. The presence of the heme cofactor and the related ability of this protein to transfer electrons by switching between different redox states, as well the possibility to immobilise the protein on electrodes, makes this protein a good candidate for molecular electronic studies and future applications [4]. Cyt b_{562} can be in the holo form, which contains the heme cofactor, or in the apo form, that is, without heme. Apo-proteins can also have a role in biological processes and can be used to conduct current in molecular junctions [129]. In fact, in a matrix of apoproteins sandwiched between electrodes, the protein cavities or clefts that correspond to the absence of the prosthetic groups may induce charge localization and polarization in the surrounding protein regions that facilitate the electron hopping from one electrode to the other.

Many studies have been carried out to investigate the conductance of holo proteins [4, 130, 131]. However, little is still known about the conductive properties of apoproteins. Recently, a group in Japan has successfully reported imaging of apoproteins with STM, studying the effect of the bias voltage on the apparent height, shape and intermolecular distance for apoproteins adsorbed on Au(111) [127, 132].

Single-molecule measurements have a crucial role in gaining the understanding that is required for developing molecular electronics. Current-distance (I-z) measurements can provide important information on the mechanism of charge transfer through protein-electrode interfaces, and thus on the optimal conditions for structural stability and electrical conduction in a molecular device. For this reason, we have produced big sets of current measurements at different tip-substrate distances, also changing the humidity conditions and the rate of data acquisition. All experiments were carried out first for the bare gold surface and then after the protein deposition. In this way, we were able to compare the conductivity of the system before and after the protein deposition. Moreover, using suitable amounts of proteins, we obtained protein densities on the metal substrate that enabled single-molecule conductance measurements, as validated by AFM and STM topographic imaging of the functionalised metal surface. Thanks to Andriy Moskalenko for helping in taking some of the STM images and I-z measurements.

5.2 Experimental work

5.2.1 Sample Preparation

A gold bead was used as the substrate where the proteins were immobilised. To get a single crystal, the bead was etched electrochemically in a 0.1 M H_2SO_4 solution. One electrode terminal was applied to the gold bead and the other to the platinum-iridium wire which was used for the etching. A voltage of +15 V was applied for 30 seconds; afterwards, the bead was immersed in 1 M HCL for 10 seconds and then in deionised water for 10 seconds. This procedure was repeated two times to improve the quality of the bead surface. Finally, the bead was baked for 8 hours in an oven at 860 °C. The cleaned gold bead was first imaged by STM in the absence of the protein sample and then was incubated for 5 minutes at 4 °C in the protein solution. We tested different concentrations of double-mutant holo cytb$_{562}$ on Au(111), so as to obtain concentrations that enabled the experimental study of individual protein molecules. After the incubation, the system was immersed in deionised water to remove excess protein, and then dried with nitrogen gas. All the measurements and imaging were performed with a home-built STM and a commercial AFM, using a multi-mode microscope with a Nanoscope III controller (DI Veeco, Santa Barbara, USA) with poly-silicon probes. Triangular cantilevers were purchased from NT-MDT (Moscow, Russia) with a nominal spring constant k = 5.8 N/m and a resonant frequency f = 120 kHz. The Platinum Iridium (Pt-Ir) tip of STM was used, and was prepared by mechanical cutting from Pt-Ir wire.

Also in some experiments the Au samples were obtained from Phasis, they were cut from the bulk piece with scissors, and cleaned by immersion in acetone for about 2 minutes, followed by immersion in isopropyl alcohol for 1 minute, and then blow drying with nitrogen gas. The cleaned Au(111) substrate was then incubated for 5 minutes in 0.5 μM and 10 minutes in 1.5 μM D5C and SH-LA apoprotein solutions, respectively. After this procedure, the sample was immersed in deionised water to remove excess protein and dried with nitrogen gas.

5.2.2 I-z Measurements

The current-distance (I-z) measurements were performed in air at room temperature and under different conditions of humidity that were achieved using the STM in combination with the home-built environmental system. The measurements were taken once the system was stabilised thermally and mechanically. Regarding the I-z method [133], the STM tip was approached to selected small scan areas with a linear size of about 10 nm, around the molecules. Once the tip was placed above the molecule, the feedback was disabled, the tip was held above the surface at set point current of 0.05 nA and bias voltage of 0.05 V. The tip was then withdrawn a fixed distance (z-start) from the set-point position. The tip then approached the surface with constant velocity recording the current as a function of z. At a distance z-end relative to the set point, the tip motion was reversed along the same path again measuring I(z). Typical values of z-start and z-end were +7 $\AA$ (retraction) and -4 $\AA$ (approach), respectively, but other values of these parameters were sometimes used. If the gap between the tip and the surface is occupied by a molecule, some characteristic features are observed in the I(z) curves. For example, in the retraction mode, the current decreases with distance starting from z-end; then a flat region of the I(z) curve that looks almost like a plateau is observed while the tip is in contact with the molecule and the latter is neither particularly compressed nor elongated (over this z range, relatively small beta factors typical of proteins are at play); finally, the current drops rapidly to zero after that the junction is broken, due to the beta decay factor associated with the air gap. Therefore, a step-like feature may be observed in the I-z curve. To produce systematic data, the measurements were repeated on several molecules and around 50-700 curves were obtained on each molecule.

5.3 Cyt b_{562} on Au(111): Results and Discussion

5.3.1 I-z of Holoproteins on Au(111) in Air

In this section we describe our experimental results on cyt b_{562} in the holo form, where a heme cofactor is attached to the (apo) protein and thus participates in the ET processes through the protein. In these experiments, the protein was immobilised on the surface of a gold bead through thiol binding groups. The measurements were performed in ambient conditions, using AFM and homebuilt STM with low drift. The low drift was checked by imaging the single molecules under study before and after performing the conduction measurements. AFM and STM were used to image the gold surface before the protein incubation, so as to ascertain that the Au(111) surface was clean and, in particular, free of gold nanoparticles. In fact, we noticed that such nanoparticles grow on Au(111) substrates over time as it is shown in Figure 5.1 or they can be produced when the STM tip crashes with the surface.

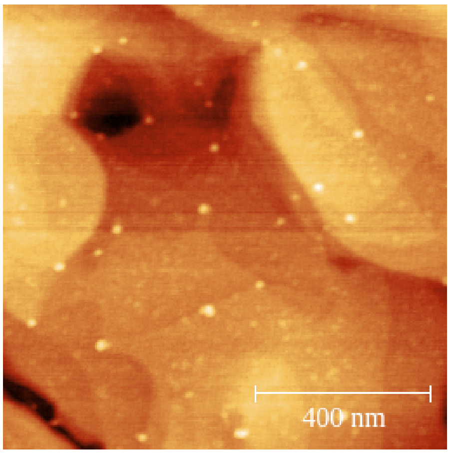

FIGURE 5.1: This AFM image of Au(111), shows that gold nanoparticles appear on the surface over time (z-range = 0-6.1 nm).

After protein immobilisation, AFM and STM images proved that the engineered SH-SA and SH-LA variants of the protein were adsorbed on the Au(111) surface in specific overall orientations. Tests prior to the conduction experiments allowed us to select protein concentrations that produced distributions of well-separated molecules on the gold surface and thus enabled single-molecule measurements. More specifically, we found that concentrations between 0.025 and 0.5 μM give well-separated protein molecules on Au(111). Figure 5.2 shows the AFM imaging of single proteins, while Figures 5.3 and 5.4 show the STM imaging of both SH-SA and SH-LA variants. The molecular heights from AFM are about 2-2.5 nm for SH-SA and in the range 4-5 nm for the SH-LA variant, in agreement with the dimensions of these proteins (2.4 nm and 5.2 nm for SH-SA and SH-LA, respectively, as in illustrated in Figure 2.9). The difference in average AFM height between the two species confirms the success of molecular engineering in defining preferential orientations of the biomolecules on the substrate surface. The single-molecules heights measured by STM are an order of magnitude lower than the real ones (as inferred from the molecular structure of cyt b_{562} proteins), namely, they appear to be between 0.2 nm to 0.5 nm in air. This considerable underestimation of the height of biomolecules on metal surfaces (compared the predicted size and AFM data) is characteristic of STM imaging and was reported previously [134]. In Ref. [134], it is explained that the false molecular height resulting from STM is the result of a convolution of electronic and structural (topographic) contributions to the observed image. However, relative height values may still be informative for adsorbates with similar electronic properties (such as electron affinity). The lateral dimensions from AFM are affected by the size of the tip, which leads to an apparent lateral size between 15 and 25 nm. The lateral dimensions from STM were instead comparable to the real dimensions of this protein. The lateral and height dimensions found in this work agree with the respective dimensions previously reported for both variants of cyt b_{562} [28].

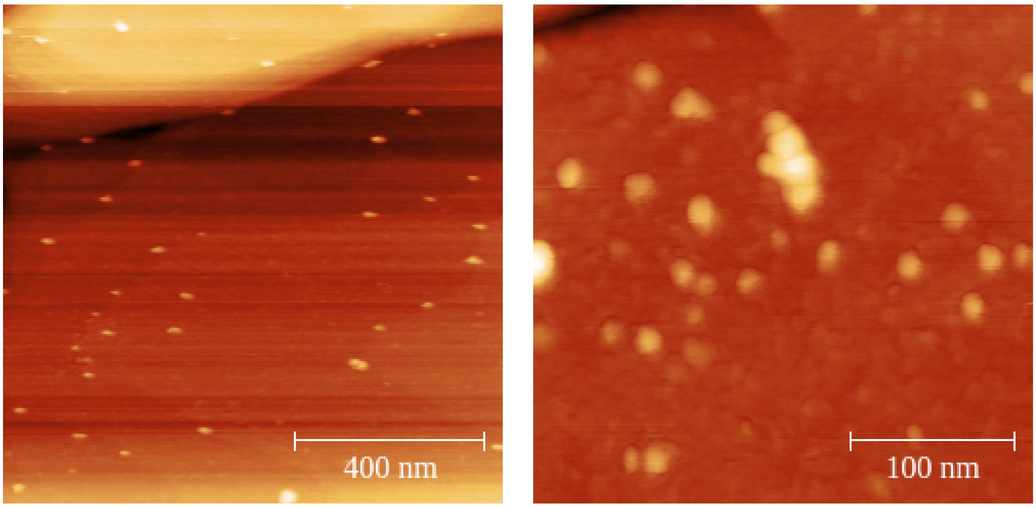

(a) (b)

FIGURE 5.2: AFM images of holo cyt b_{562} on Au(111) at ambient RH, the protein concentration used in preparing the sample was 0.025 μM. The incubation time was 5 minutes. (a) SH-SA (z-range = 0-13 nm). (b) SH-LA (z-range = 0-20.7 nm).

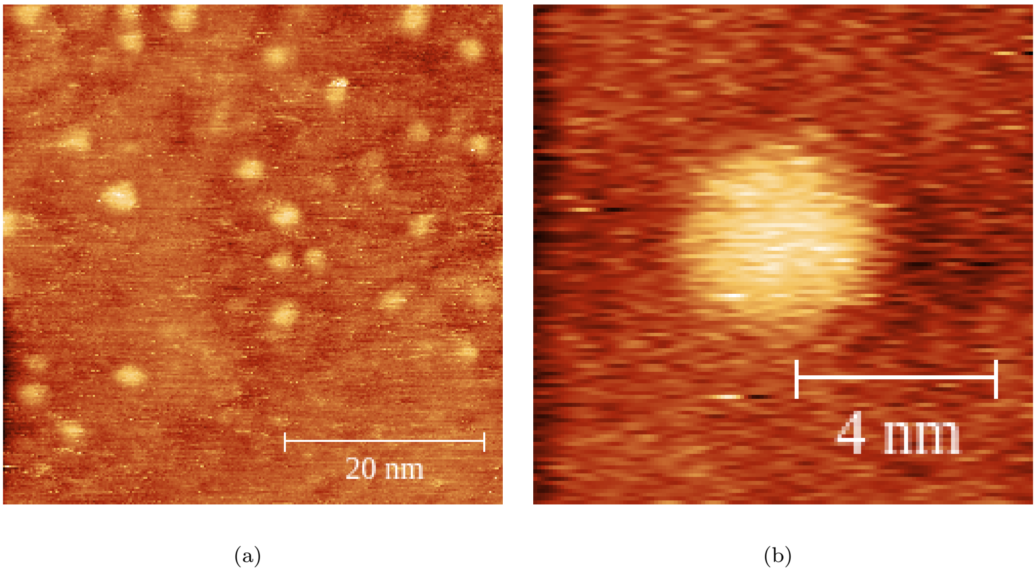

(a) (b)

Figure 5.3: STM images of cyt b_{562} holo SH-SA on Au(111) at ambient RH and temperature. The concentration used to prepare the sample was 0.05 μM. The incubation time was 5 minutes. Current set point = 0.05 nA, bias voltage = 0.05 V. (a) Many molecules (z-range = 0-0.72 nm). (b) Single molecule (z-range = 0-0.52 nm).

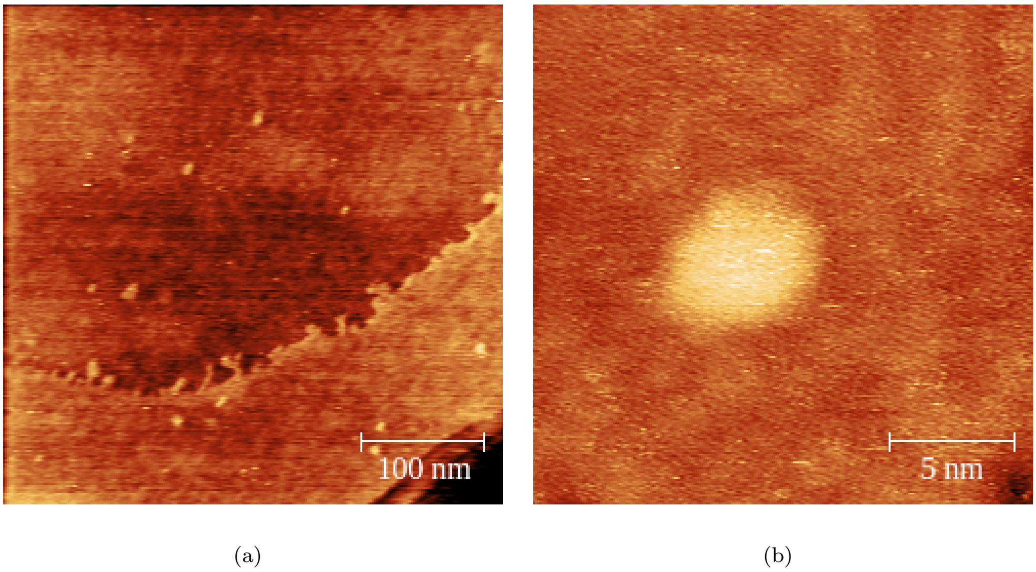

(a) (b)

Figure 5.4: STM images of cyt b_{562} holo SH-LA on Au(111) at ambient RH and temperature (23.57 °C). Sample preparation: protein concentration = 0.05 μM, substrate incubation time = 5 minutes. Measurement conditions: current set point = 0.05 nA, bias voltage = 0.05 V. (a) Many molecules (RH = 39.33%; (z-range = 0-2.2 nm). (b) Single molecule (RH = 39.06%; z-range = 0-0.6 nm).

Before studying the functionalized surface, we measured the conductance as a function of the tip-substrate distance in the absence of protein. Most conductance curves did not show any step-like feature (see Figure 5.5) and, accordingly, the conductance histograms did not show peaks (Figure 5.6), differently from what was observed for the samples with biomolecules (see below). To investigate the electrical properties of the two cyt b_{562} variants, we first imaged the proteins on Au(111) with STM at a constant current of 0.05 nA and a bias voltage of 0.05 V, thus visualizing the morphology of the functionalized surface and ascertaining that we could see well-separated single protein molecules. Afterwards, several I-z measurements were taken on many different molecules. Figures 5.7 and 5.8 show the conductance curves for single holo-SH-SA cyt b_{562} proteins. After that the system was equilibrated under a current set point of 0.05 nA and a bias voltage of -0.05 V, the distance dependence of the current was measured retracting the tip away from the functionalized surface by 4 $\AA$ (z-start = 4 $\AA$) and then approaching the surface by 4 $\AA$ (z-end = -4 $\AA$). Similar conductance measurements on the holo SH-LA cyt b_{562} are reported in Figure 5.11 (for this system the retraction distance was 7 $\AA$ while the other physical parameters were set as in Figures 5.7 and 5.8).

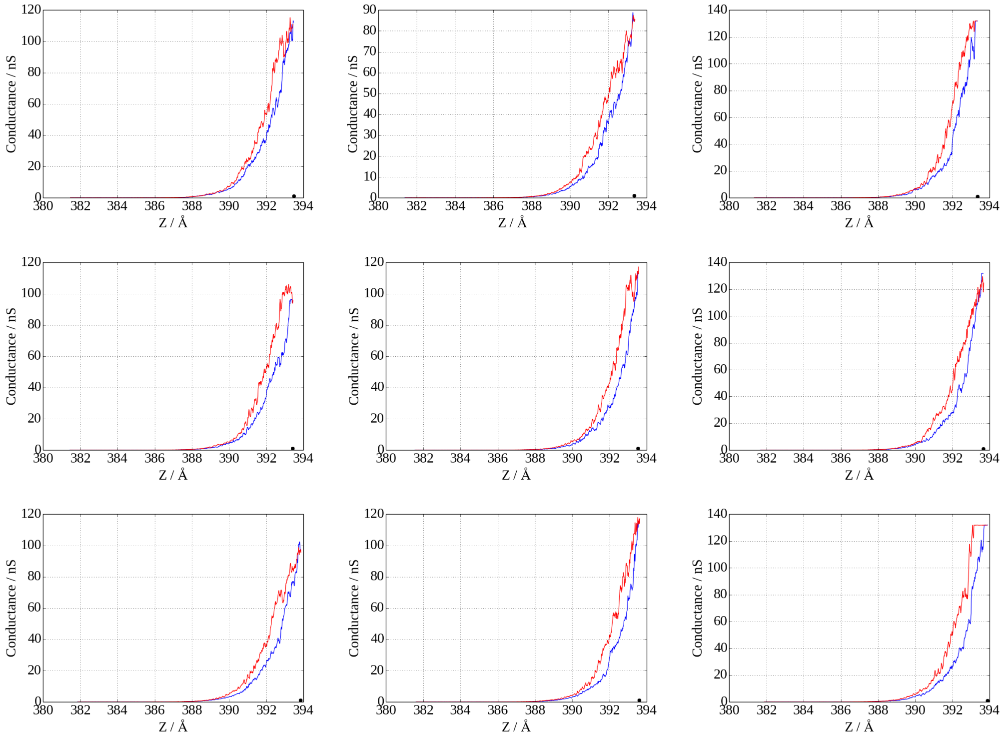

Figure 5.5: Conductance curves on Au(111), Current set point = 0.05 nA, bias voltage = 0.05 V, z-start = 7 $\mathring{A}$, z-end = -5 $\mathring{A}$, tip sweep rate = 1 nm s^{-1}.

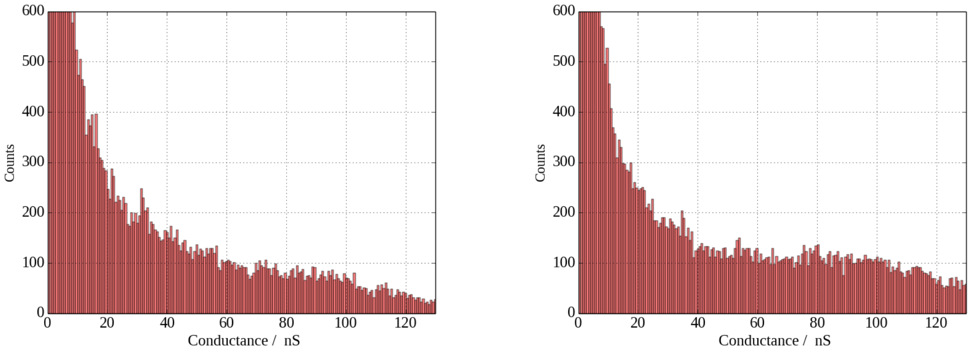

(a)

(b)

Figure 5.6: Conductance histograms of Au(111) at ambient conditions (100 curves were used to produce this histogram), z-start = 7 $\mathring{A}$, z-end = -5 $\mathring{A}$, included data shown in Figures 5.5. Conductance was calculated as the ratio between the measured current and the applied voltage. (a) From approaching curves. (b) From retracting curves.

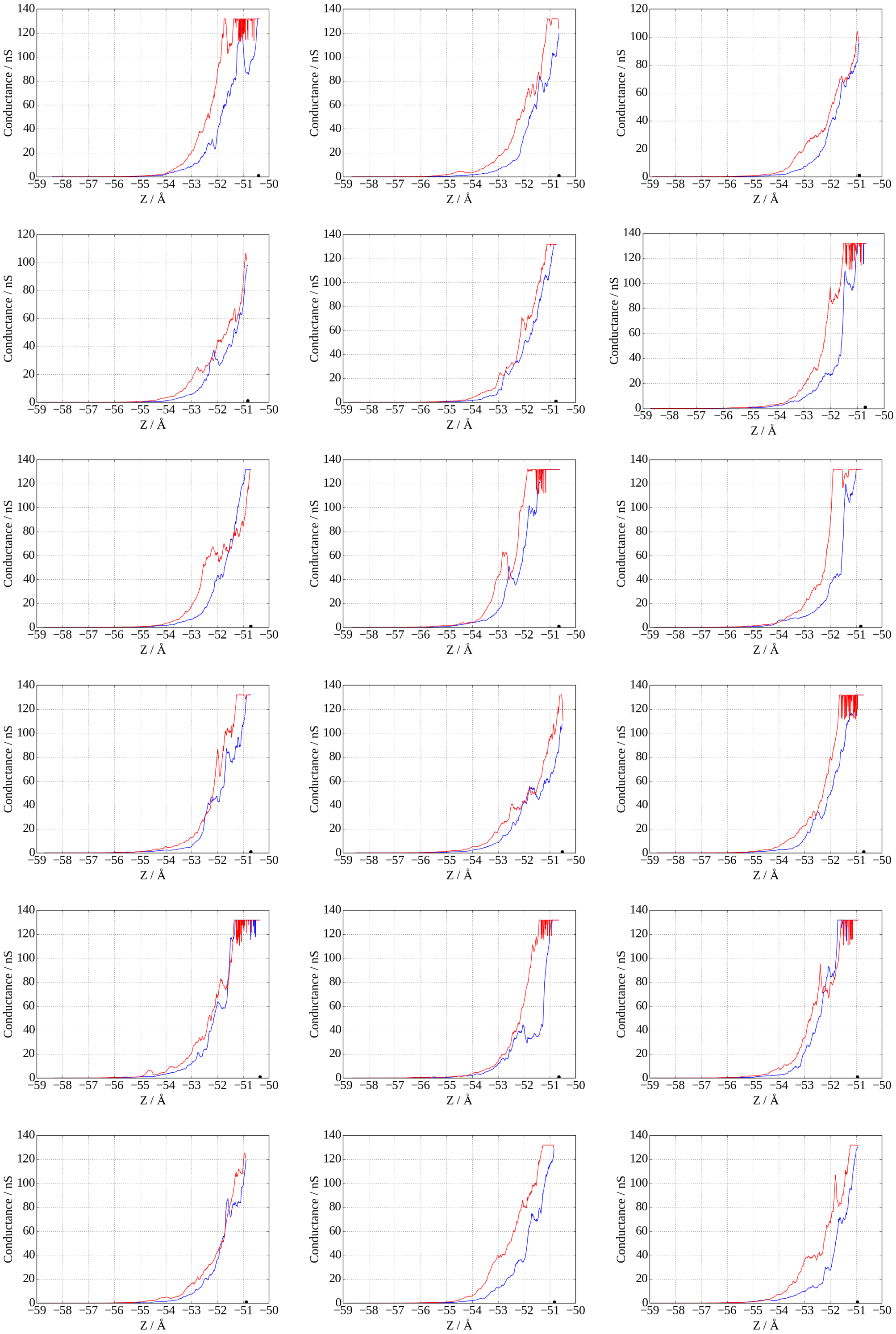

FIGURE 5.7: Set of conductance curves for cyt b_{562} SH-SA on Au(111). The conductance was recorded as a function of the tip-substrate distance z, which was measured relative to the set point. z-start = 4 $\AA$, z-end = -4 $\AA$, current set point = 0.05 nA, bias voltage = -0.05 V, rate = 1-10 nm s^{-1}. Approach and retraction curves are drawn in blue and red, respectively.

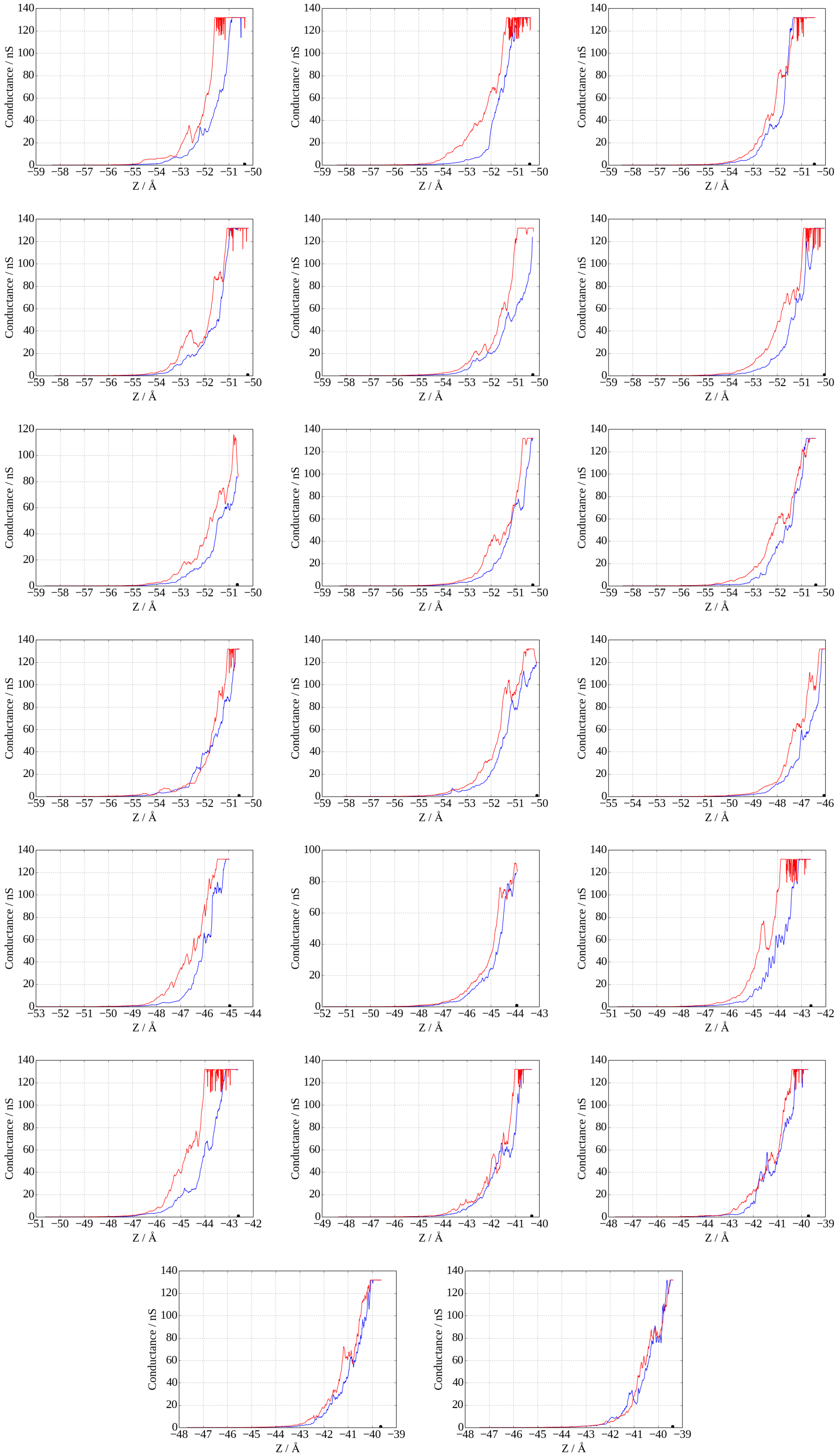

FIGURE 5.8: Other set of conductance vs distance curves on single cyt b_{562} SH-SA molecules on Au(111), z-start = 4 Å, z-end = -4 Å, current set point = 0.05 nA, bias voltage = -0.05 V, rate = 1-10 nm s^{-1}. Approach and retraction curves are drawn in blue and red, respectively.

The I-z curves do not show a smooth single-exponential decay of the current with distance, as it would be expected in the absence of sample molecules [135, 136]. In this case, only the beta decay factor (see section 2) of the essentially homogeneous air medium would be observed. Features such as conductance steps are instead observed. For example, in Figure 5.7, first graph of the third line, in the approaching mode (blue line) the current increases with a beta factor on the order of 2 $\AA^{-1}$ which can be ascribed [137] to the contribution to the conduction by an air gap. Contact with a molecule introduces a much smaller beta factor (the one for the protein medium), with the appearance of a step-like feature in the I-z curve which is a signature of the formation of a molecular junction [135, 138, 139]. Further approach can change the conduction mechanism and the number of available charge-transport channels, thus determining a new large increase in the current. In the retraction mode (red curve), we can see a significantly wider regime of through-protein conduction. We might infer that, after the approach of the tip, the molecule takes, on the average, different conformations and has a wider contact area with the tip (compared to before the approach), thus determining a lingering of the tip-molecule contact and a persistence of the through-protein conductive mode over a longer distance range. Multiple steps are observed in some I-z curves. The presence of multiple steps could lead us to think to subsequent contact of the tip with different numbers of molecules. However, similar steps would appear if the tip gets closer to the protein, increasing the number of contact points with the protein and the routes for charge transfer to the substrate. This interpretation can be appropriate when the molecules are separated enough on the surface. Hysteresis between approach and retraction was observed for all I-z curves. This hysteresis might be at least partly attributed to the fact that, for fast enough z scan rates, the molecule is unable to achieve an equilibrium configuration at each tip position. Thus, at the same z during the two runs of the tip, the molecule takes different average configurations between the electrodes, which produce different conductance values. This interpretation is further supported in those I-z cycles where the approach and retraction conductance curves show similar features, since such features suggest the stable presence of a protein molecule between tip and substrate during the two tip runs.

The current increase before the contact with molecules (as interpreted from step-like features in the I-z curves) is rather smooth, and probably indicates a combined contribution of the air gap and the protein to the conduction prior to achieving the contact with a molecule. In fact, if the redox biomolecule is under the tip, (a) changing z amounts to changing the fraction of substrate-tip gap occupied by the molecule and thus the potential difference across the molecule; (b) it has been shown that the molecular reorganization determines a smoother evolution of the current as a function of the voltage compared to the case of molecules with negligible reorganization energy or to the absence of redox molecular bridges [47, 50]. Considering that the change in tip-substrate distance also changes the profile of the potential drop in between, it would be interesting and useful to see future theoretical studies that explain the non- linear conduction phenomena described above by using models similar to those developed to describe such phenomena in I-V curves [50]. The presence of non-linear conduction and low-conductance features are clearly shown by the departures from linearity in the logarithmic conductance plots for SH-SA (Figure 5.9). The fact that conduction through the air gap and through the protein both approximately obey exponential decays with distance (although with different decay factors) and the fact that the protein extends through a significant fraction of the tip-substrate gap lead to curves that could be considered linear to a gross level of approximation, but changes in slopes and other complecities are clearly visible in the curves of Figure 5.9.

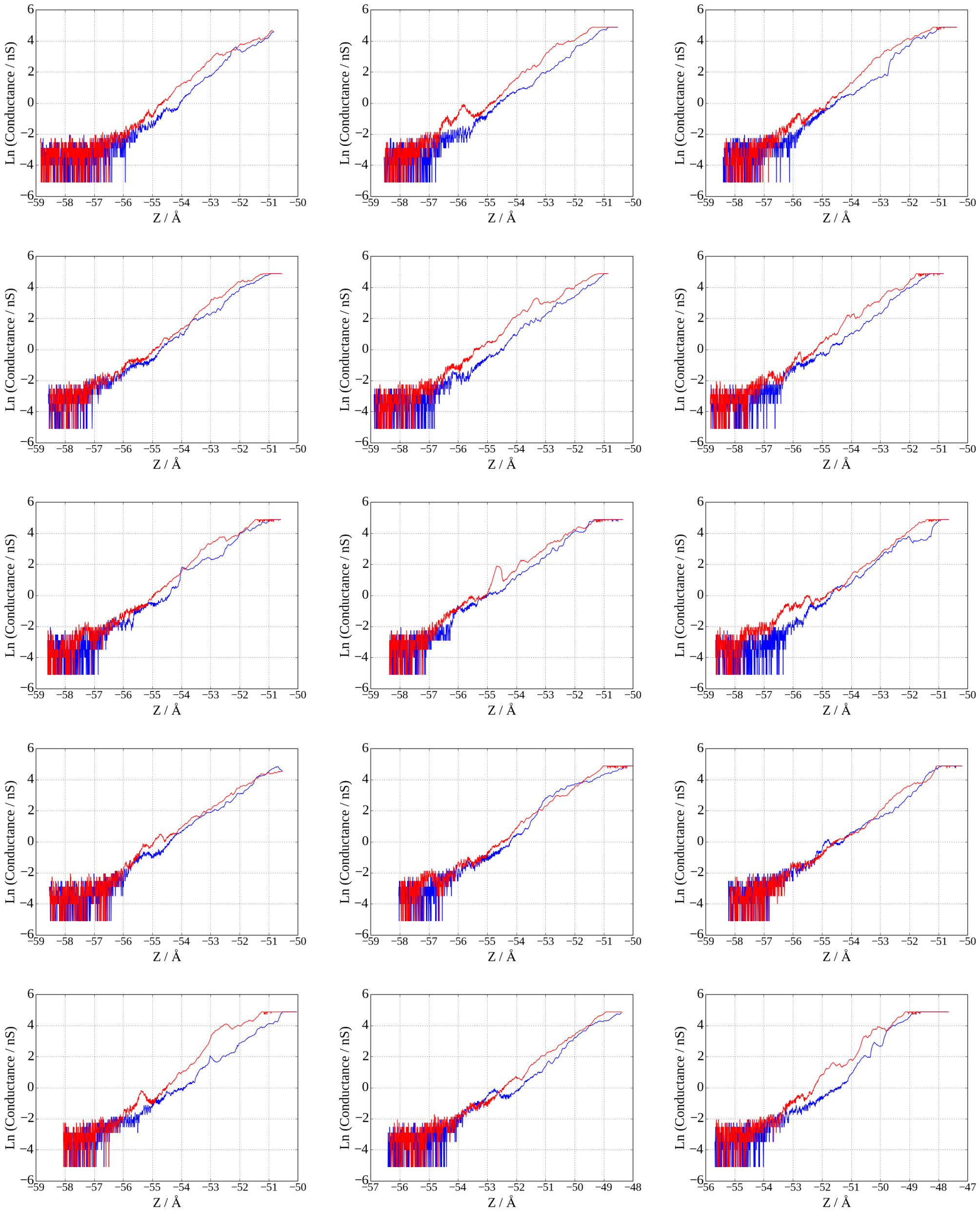

FIGURE 5.9: Logarithmic conductance as a function of the tip distance from the substrate for single b_{562} SH-SA on Au(111). z-start = 4 *Å*, z-end = -4 *Å*, current set point = 0.05 nA, bias voltage = -0.05 V. Approach and retraction curves are drawn in blue and red, respectively. The tip sweep rate ranged from 1 to 10 nm s^{-1} for the different curves. This figure shows the step-like features that appear at low conductance values.

Statistical analysis was performed to produce conductance histograms, where we counted the number of data points, over many I-z curves, with conductances in given ranges. The conductance was readily obtained as the ratio between the measured current at a given z and the applied bias voltage

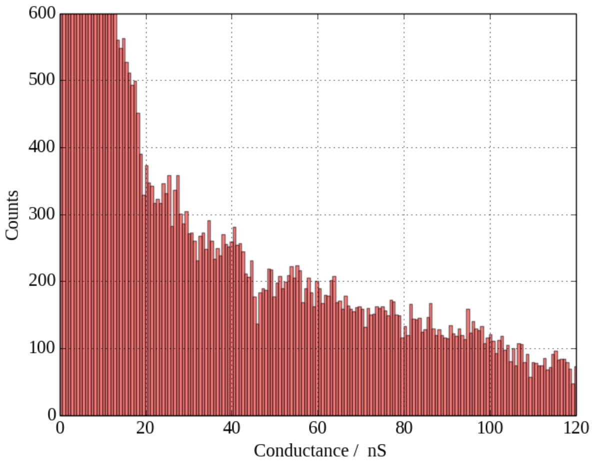

(a)

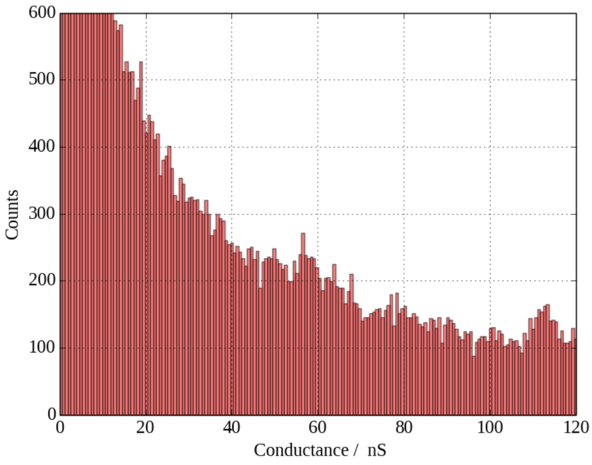

(b)

FIGURE 5.10: Conductance histograms of cyt b_{562} SH-SA at ambient conditions (selected data: 143 curves out of 741; the selection was performed manually). z-start = 4 $\AA$, z-end = -4 $\AA$, included data shown in Figures 5.7 and 5.8. Conductance was calculated as the ratio between the measured current and the applied constant voltage. The two histograms were obtained from the (a) approaching curves and (b) retraction curves.

Figure 5.10 shows the conductance histogram for SH-SA . The weak peaks arise from the fact that more data points (taken at different z values) have similar conductances. Therefore, these peaks correspond to relatively flat regions along the I-z curves, namely, to z ranges where the beta factor is smaller, likely because of the presence of a molecule or a part of it that fits into the gap between tip location and substrate. I-z curves which showed these short plateaus were selected for inclusion in producing the histograms shown in Figure 5.10 for the SH-SA variant and in Figure 5.12 for the SH-LA variant. No clear peaks are observed if all the I-z curves are included in the analysis. In fact, although the protein engineering produces a preferential average orientation of the adsorbed molecule between tip and substrate, molecules are subject to conformational changes and the reciprocal orientation of tip and molecule, as well as the distortion of molecule as the tip approaches it, generally differ in different runs and even along a single run of the tip. These factors generate a distribution of small beta z regions over different curves, thus smoothing the peaks in conductance histograms, until when they are not visible for sufficiently large sets of I-z curves employed. Another reason why the histogram peaks would tend to vanish if all I-z data were included in the statistical analysis is that the conductance steps are not seen in about 80-85% of the I-z curves. In Figure 5.12, we can see the conductance histogram for the SH-LA variant, which showed similar behaviour to that of SH-SA, where no clear peaks are observed but some weak peaks are discernible. Even though many short plateaus are seen in Figures 5.7, 5.8 and 5.9, these occur at a range of different current values (which can be explained in terms of different paths for charge transfer through proteins [140]), leading to a shortage of clear peaks in the histograms. Xiao, et al. have found similar sequences of steps at different conductance for Single Peptide Molecules as well [141].

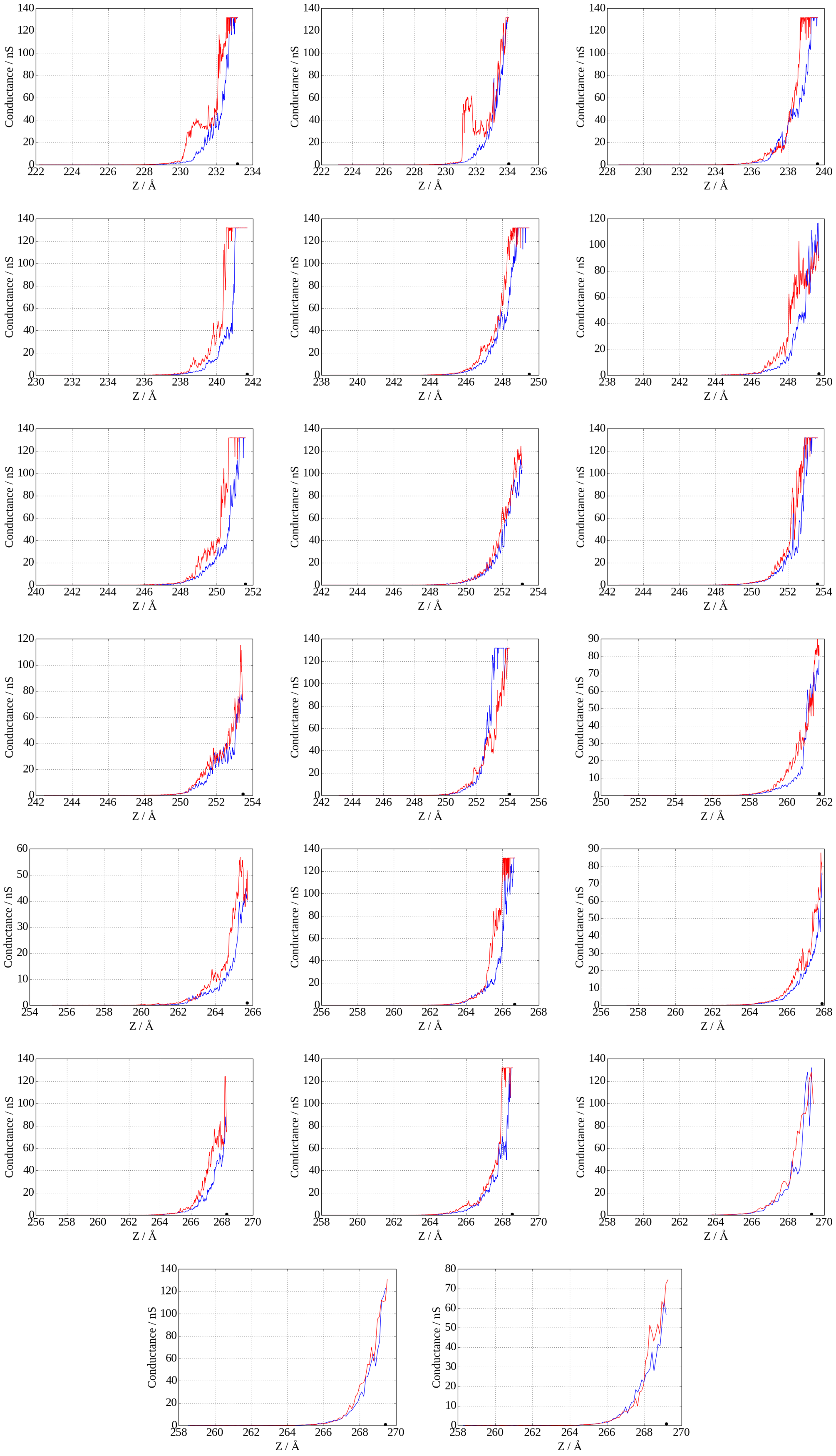

FIGURE 5.11: Conductance as a function of the tip distance from the substrate for single cyt b_{562} SH-LA molecules on Au(111), z-start = 7 *Å*, z-end = -4 *Å*, current set point = 0.05 nA, bias voltage = -0.05 V, rate = 1 nm s^{-1}. Approach and retraction curves are drawn in blue and red, respectively.

The features in Figures 5.7, 5.8 and 5.9, as well as in Figures 5.10, 5.11 and 5.12 for the SH-LA molecule, can also partly arise from local regions of different beta factor that prevalently fit into the gap between tip and substrate at different z values along a tip run and in different runs. For example, β-sheets and α-helices have different beta decay factors for electronic couplings [138] and hence (see chapter 2) for the current. In this regard, a combined experimental-theoretical work recently showed how amino acid side chains, peptide length, and peptide secondary structure strongly influence electron transport [140]. In addition, as said above, the conduction mechanism will generally depend on the tip-substrate distance and, while a beta decay factor can be approximately defined in both single-site hopping (as arising from the expressions for the ET rate constants) and coherent transport mechanisms (see Chapter 2), free energy parameters significantly affect the current (in addition to the shift between molecular and metal energy levels) in the case of charge hopping through the protein redox center.

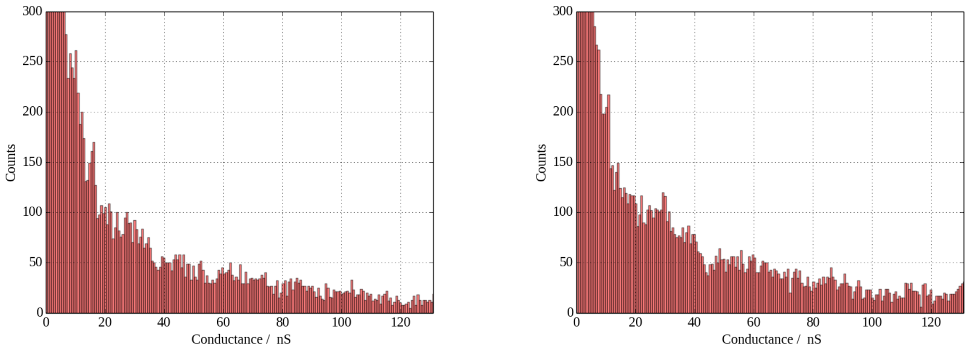

(a) (b)

Figure 5.12: Conductance histograms of cyt b_{562} SH-LA on Au(111) at ambient conditions (selected data: 50 curves out of 352), z-start = 7 $\AA$, z-end = -4 $\AA$. All of the data shown in Figure 5.11 were included in the statistical analysis. (a) From approaching curves. (b) From retracting curves.

The above discussion also implies that one has to be careful in testing different distances of minimum approach to a molecule. Long tip runs can cause molecule compression and denaturation or breaking. In Figure 5.13, the tip was moved by 20 $\AA$ towards the surface, using a speed of data acquisition of 200 $\AA s^{-1}$. This approach damaged the molecule, as shown by the images before and after the

I-z measurements in Figure 5.13. A calculation of the distance between tip and substrate at the set point using equation 2.19 in chapter 2 (with I = 0.05 nA and V = 0.05 V) gives a value of 12 $\AA$, which is clearly an underestimation of the real distance (as said in chapter 2), although equation 2.19 can be used to assess relative distance values regarding similar systems. β factors were calculated by fitting the approximately linear parts of the experimental ln(I) versus z curves to equation 2.19. Therefore, the β factor values were obtained from the slopes of the fits.

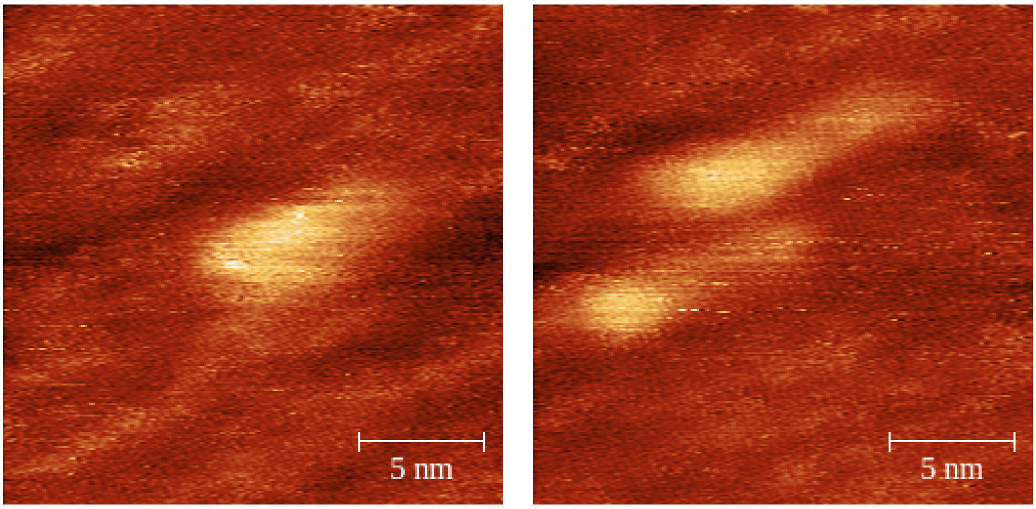

(a) (b)

FIGURE 5.13: STM images of cyt b_{562} SH-LA on Au(111), current set point= 0.05 nA, bias voltage = 0.05 V, z-start = 0 $\AA$, z-end = 20 $\AA$. (a) Before I-z measurements (z-range = 0-0.41 nm). (b) After I-z measurements (z-range = 0-0.41 nm).

The above data demonstrate that the closest approach distance is an important consideration for studying protein conductance via STM: too close an approach can lead to damage to the protein molecules.

Now, we consider whether the approach and retraction rates can significantly affect the observed I-z curves. Figure 5.14 illustrates the β factor values for SH-SA single molecules, which were calculated from the experimental approaching and retracting I-z curves for different rates of data acquisition (that is, for different speeds of the tip). The β factor was found to be in the range 1.2 ± 0.6 $\AA^{-1}$ for cyt

b_{562} under ambient conditions of temperature and humidity. This range of values is comparable to what was previously observed for cyt b_{562} [28]. Moreover, Figure 5.14 shows that the ranges of beta factor values at different tip speeds largely overlap, which means that the range of explored electron tunnelling pathways is similar for different tip sweep rates.

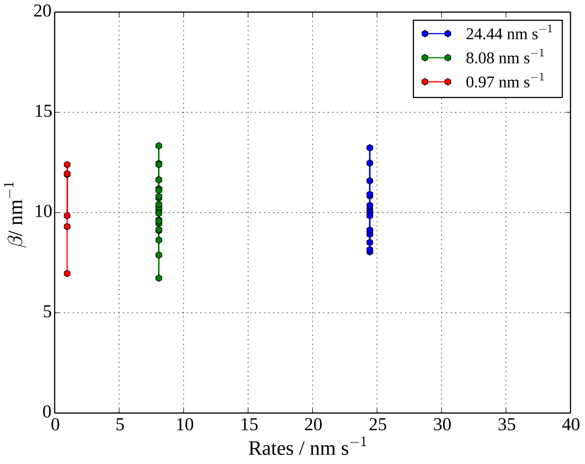

(a)

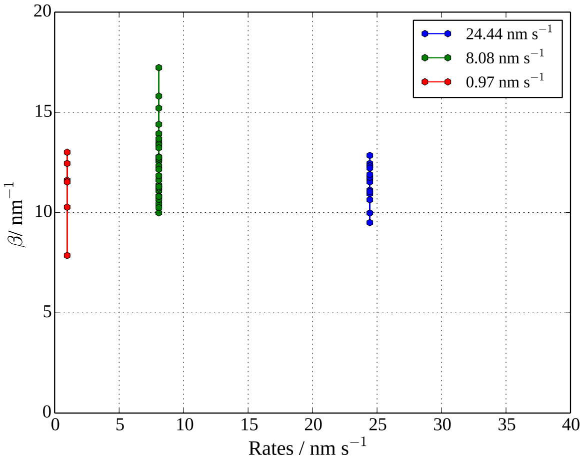

(b)

FIGURE 5.14: β factor of approaching and retracting I-z curves for different tip sweep rates on cyt b_{562} SH-SA under ambient RH. (a) For approaching curves. (b) For retracting curves.

5.3.2 I-z of Holoproteins on Au(111) in Environmental Cell

In these experiments, cyt b_{562} SH-LA proteins in the holo form were immobilised on the surface of a gold bead through their thiol groups and studied under low humidity conditions and also at low temperature, as allowed by the use of the environmental cell. Therefore, these measurements, together with the ones described in the previous section, provide information on the influence of the humidity and temperature on the conductance through the functionalized surface. To investigate the effect of water moisture on the electrical measurements of protein molecules, the environmental system was used to obtain low relative humidity (RH) levels, between 0.5-3.8%. Under these conditions, the proteins were first imaged with STM and then I-z curves were taken for single molecules similarly to those discussed in the previous section. Figure 5.15 shows the molecules on the A(111) surface imaged by STM under low humidity levels (RH = 2.06-2.66%). Note that the contrast of the images is different from that obtained under ambient conditions. Note also that the large inter-molecular distances observed in Figure 5.15 enabled measurements of single-molecule electrical properties.

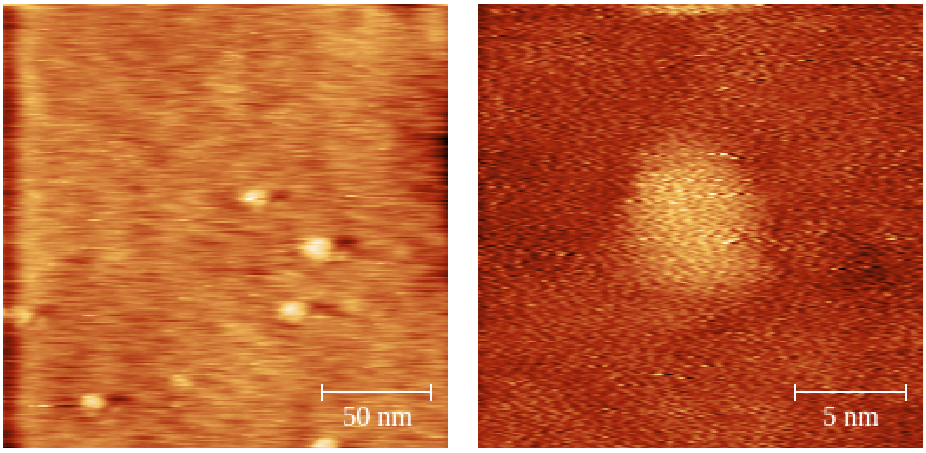

(a)

(b)

FIGURE 5.15: STM images of cyt b_{562} SH-LA under low RH and temperature (23.58 °C). Protein concentration in the sample preparation = 0.05 μM, incubation time = 5 minutes, current set point = 0.05 nA, bias voltage = 0.05 V. (a) Many molecules (RH = 2.06%), (z-scale = 0-2.4 nm). (b) Single molecule (RH = 2.66%), (z-scale = 0-0.8 nm).

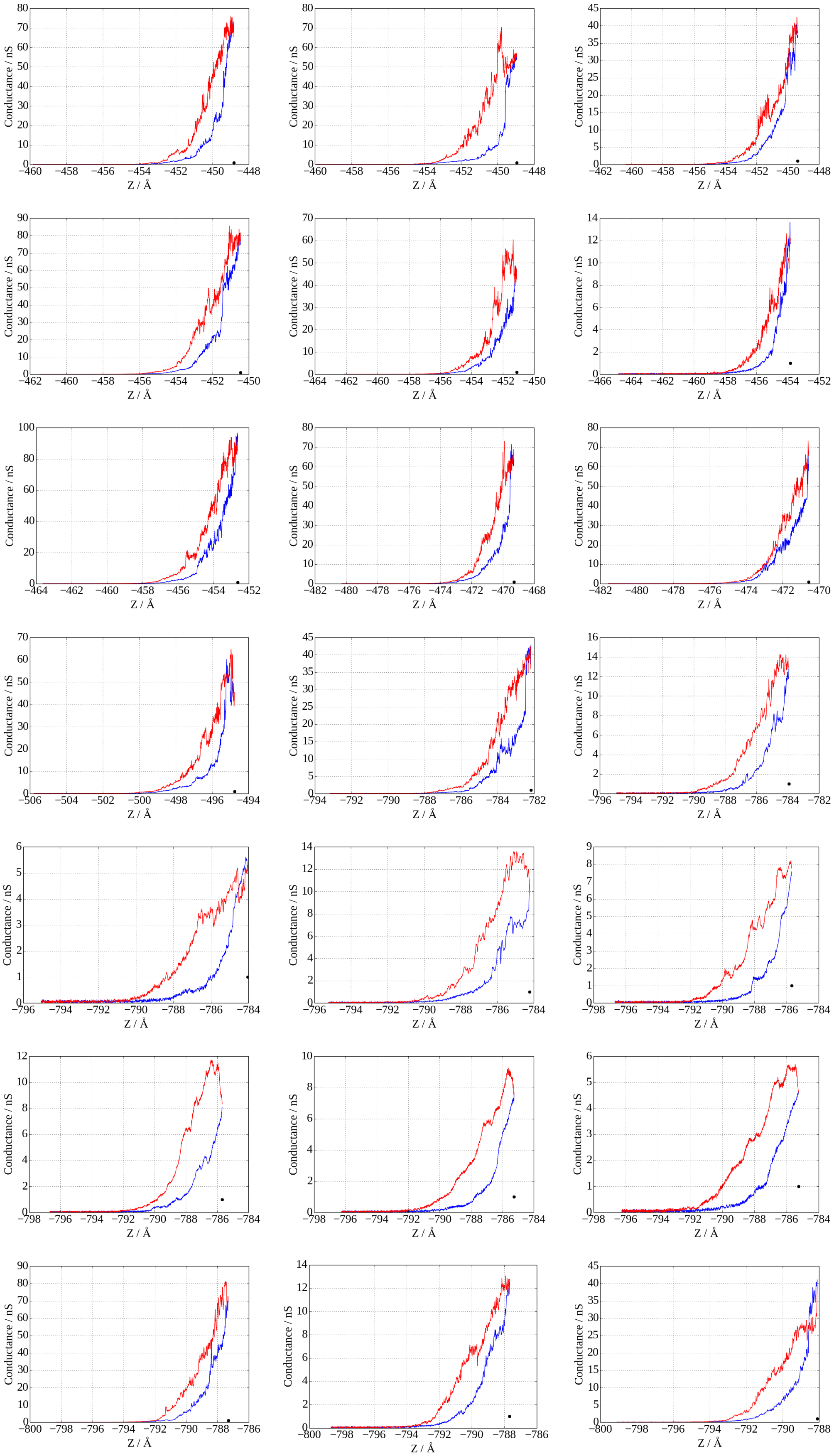

FIGURE 5.16: Conductance as a function of distance of the tip position above the substrate for cyt b_{562} SH-LA onAu(111) under low humidity. RH = 2.25%-3.70 %. z-start 7 A, z-end -4 A. Current set point = 0.05 nA, bias voltage = -0.05 V.

The conductance curves for SH-LA were taken for levels of RH between 2.25 % and 3.70 %. The z- start value was 7 $\AA$ and the z-end was -4 $\AA$, with set point current and bias voltage of 0.05 nA and 0.05 V, respectively. The I-z curves are shown in Figure 5.16. Steps in the conductance appear similarly to what observed under ambient conditions. Figure 5.16 shows a wide range of possible currents and, on the average, lower currents than under ambient RH conditions.

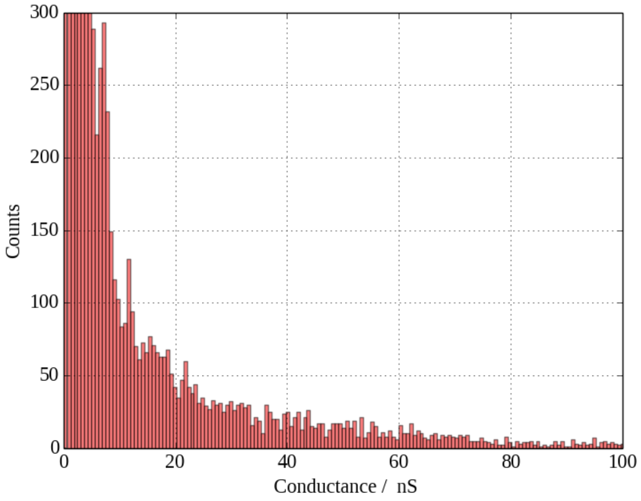

(a)

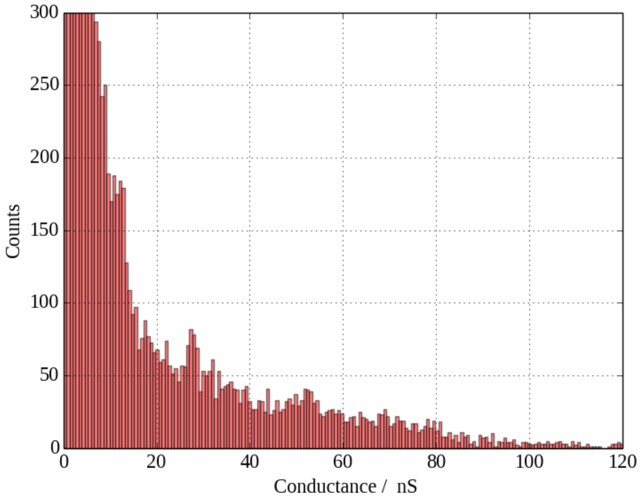

(b)

FIGURE 5.17: Conductance histograms of cyt b_{562} SH-LA under low humidity. Selected data: 29 out of 163. RH = 2.25%-3.70%, z-start 7 $\AA$, z-end -4 $\AA$). (a) From approaching curves. (b) From retracting curves.

The conductance histograms for the data taken under low humidity are reported in Figure 5.17 and show some weak peaks for both the approach and retraction curves. The β factors under ambient conditions (RH around 40%; a single measurement gave the value RH = 38.87%) and under low RH (3.65%) for SH-LA variant for different tip sweep rates are reported in Figure 5.18. On the average, the β decay factors at low RH are a little lower than those found under ambient conditions (for example, compare the ranges of values at ambient and low RH for the tip sweep speed of about 1 nm/s).

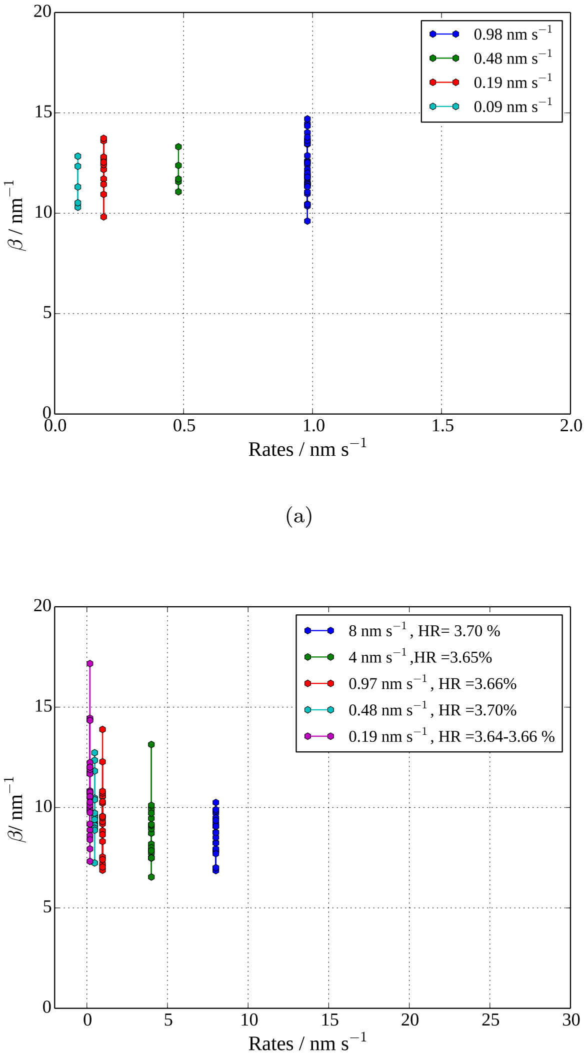

(a)

(b)

FIGURE 5.18: β decay factor as a function of tip sweep rate for cyt b_{562} SH-LA. (a) Under ambient (RH around 40%; a single measurement gave 38.87%). (b) Under low RH (3.65%).

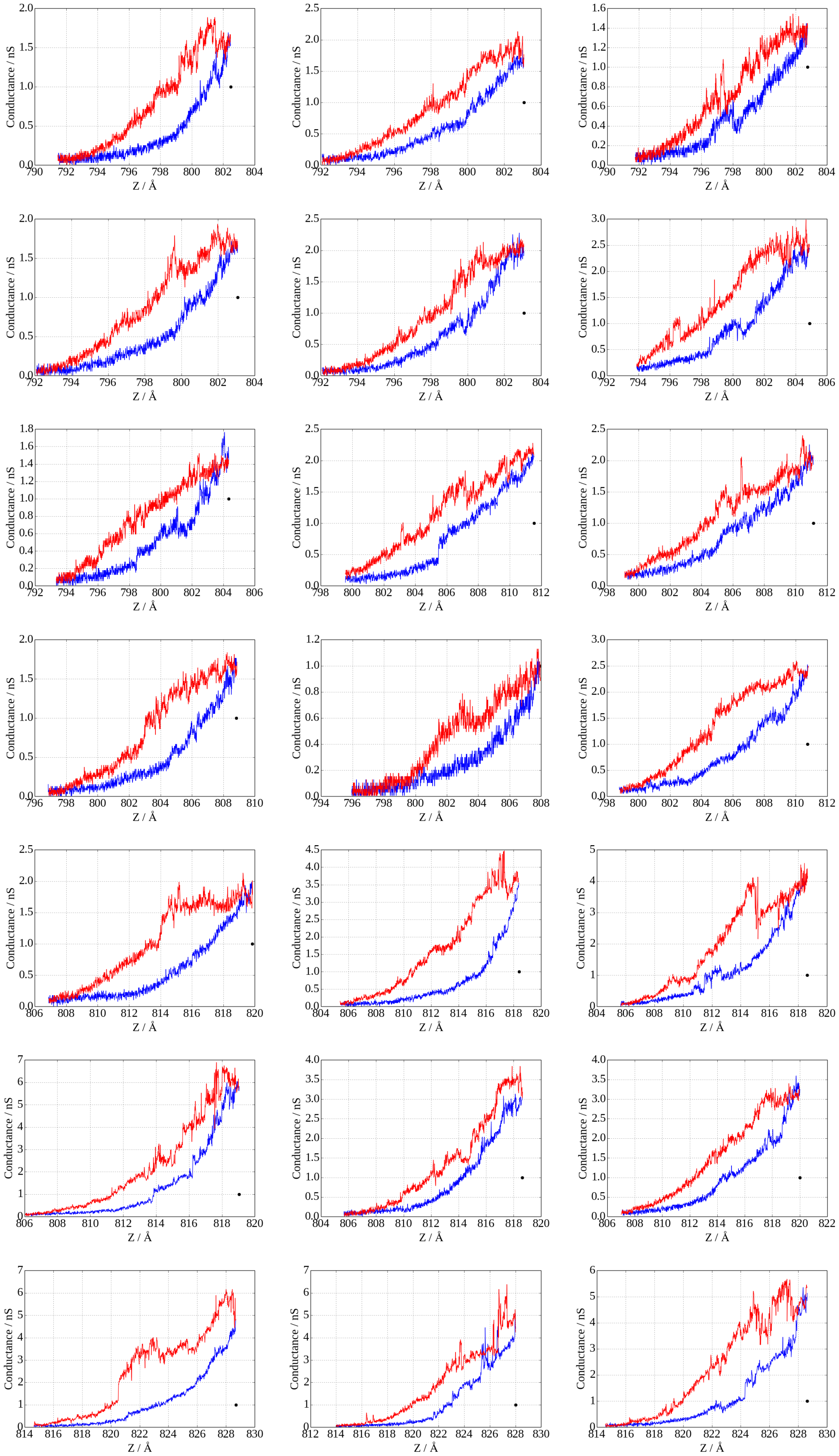

FIGURE 5.19: Conductance curves for cyt b_{562} SH-LA on Au(111) under low RH of 0.82% - 1.01% and low temperature of 13.85 °C; z-start = 7 $\mathring{A}$, z-end = -4, -5, -6, -7 $\mathring{A}$; current set point = 0.05 nA, bias voltage = -0.05 V.

The conductance is further decreased at low humidity and relatively low temperature (cf. Figure 5.16 with Figures 5.17, 5.19 and 5.20), and clear count peaks are observed in the conductance histograms of Figure 5.20, which denote the presence of molecular features over a significant fraction of the tip-substrate gap at each tip position. Moreover, the values of the beta decay factor (see Figure 5.21) are further decreased compared to those in Figure 5.18.

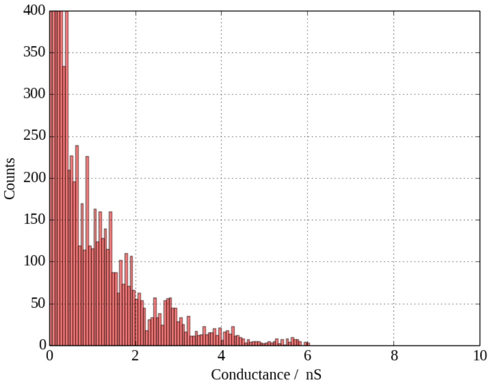

(a)

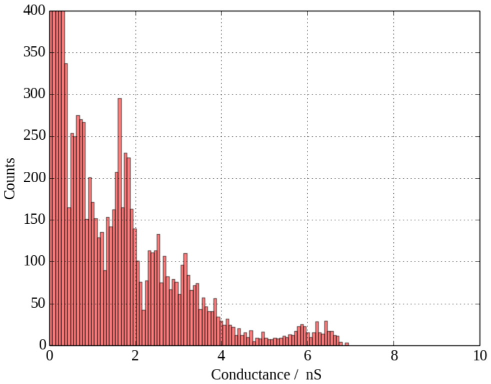

(b)

FIGURE 5.20: Conductance histograms of cyt b_{562} SH-LA under low RH of 0.82%- 1.01% and low temperature of 13.85 °C. We analysed 10 curves for each of the chosen z-start and z-end values. z-start = 7 $\mathring{A}$, z-end = -4, -5, -6, -7 $\mathring{A}$. (a) From approaching curves. (b) From retracting curves.

The low humidity values are very far from the natural environment of a protein (even farther than typical ambient RH in our lab is), where the aqueous solvent is a determinant of its folding, which tends to move hydrophobic patches towards the inner part and hydrophilic patches towards the external, solvent-exposed part of the protein. Very low humidity conditions may determine a partial loss of structural compactness of the molecule, or changes in structure features relevant to ET, also related to loss of structured water, with accordingly reduced conductance. The larger extent of the molecule between tip and substrate (so that the molecule occupies a larger fraction of the tip-substrate gap at each tip position), together with the deterioration of specific water-assisted channels for the through-protein ET, would consistently explain why the tip displacement affects a little less the conduction under low humidity than other ambient (much higher) humidity, thus leading to an overall lower β decay factor for the junction bridging medium. This hypothesis relies upon the fact that working folded proteins are generally exposed to some aqueous solvent in their natural environment. However, currently, we do not have enough direct evidence supporting our hypothesis on the effect of humidity on protein structure and hence on conductance in the STM setup (but also see Figure 5.35). Future experimental and theoretical investigation to test this hypothesis would be desirable.

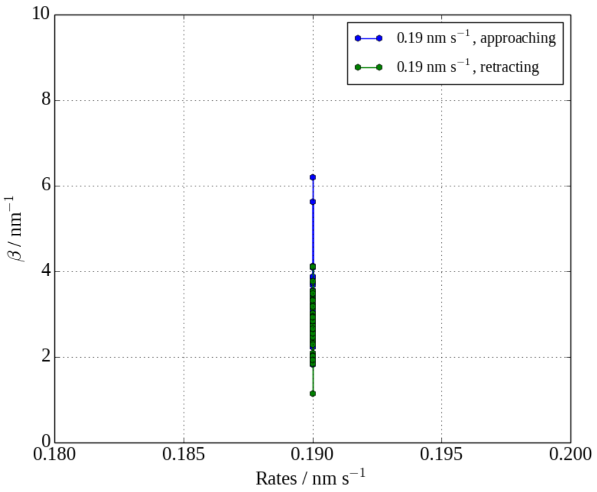

Figure 5.21: β factor of approach and retraction curves for cyt b_{562} SH-LA under low RH (0.82%) and low T(13.85 °C). Tip sweep rate = 0.19 nm s^{-1}.

5.3.3 I-z of Apoproteins on Au(111) in Air

In this work, we directly anchored apoproteins to an Au(111) surface through sulfur bonding. After introducing cysteine at specific position in the protein.

Scanning with AFM and STM, we were able to show the topography of the gold surface with adsorbed apoproteins, and to measure the conductance through these proteins. Two different variants of mutated apoprotein were used to show the dependence of the conductance on the molecular orientation. The first one, the single-mutant variant D5C, has the cysteine residue at position 5; the second one, the double-mutant variant SH-LA, has two cysteine residues at positions 50 and 21 that should favour molecular alignment along its long axis between tip and substrate. These measurements, together with the ones discussed above, allow us to compare the conductivities of the holo and apo forms of the protein, hence to quantify the effect of the redox cofactor on the electrical properties of the individual protein molecules.

Tapping mode AFM was used to image the substrates with the protein molecules immobilised on them. STM was used to measure electrical properties such as the molecular conductivity. The samples were deposited on Au(111) on mica. We used the same preparation protocol as in section 5.2.1. We successfully imaged the apoproteins on Au(111) by both AFM and STM. As it is shown in Figures 5.22 and 5.23, individual protein molecules were clearly identified. The average molecular lateral sizes from STM were in the range 5 to 6 nm, as expected for these proteins. The height of the cyt b_{562} apo-D5C was found to be in the range 0.2 to 0.4 nm from STM and mostly in the range 2 to 2.5 nm using AFM, although a large height was measured for some molecules, up to 4 nm.

Figure 5.24 and Figure 5.26 show conductance curves in ambient conditions for the D5C and SH-LA proteins, respectively. In Figure 5.24, the current set point is 0.03 nA and the bias voltage is -0.05 V; the value of z-start is 4 $\mathring{A}$ and z-end takes the values -9, -10 and -14 $\mathring{A}$. The measurements in Figure 5.26 were also taken at ambient conditions and the bias voltage was - 0.05 V for all curves, while the current set point was 0.05 nA or 0.5 A. The value of z-start was 7 $\mathring{A}$ and z-end was -4 $\mathring{A}$.

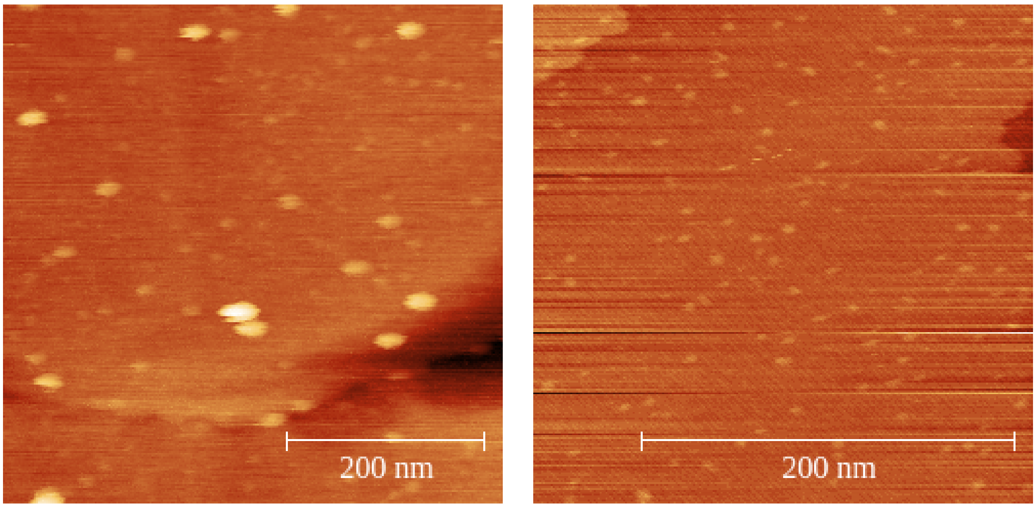

(a) (b)

FIGURE 5.22: Cyt b_{562} D5C apo proteins images with veeco system, 0.5 μM, 5 minutes incubation time. (a) AFM image (z-range = 0-18 nm). (b) STM image. Current set point = 0.05 nA, bias voltage = 0.05 V (z-range = 0-2.2 nm).

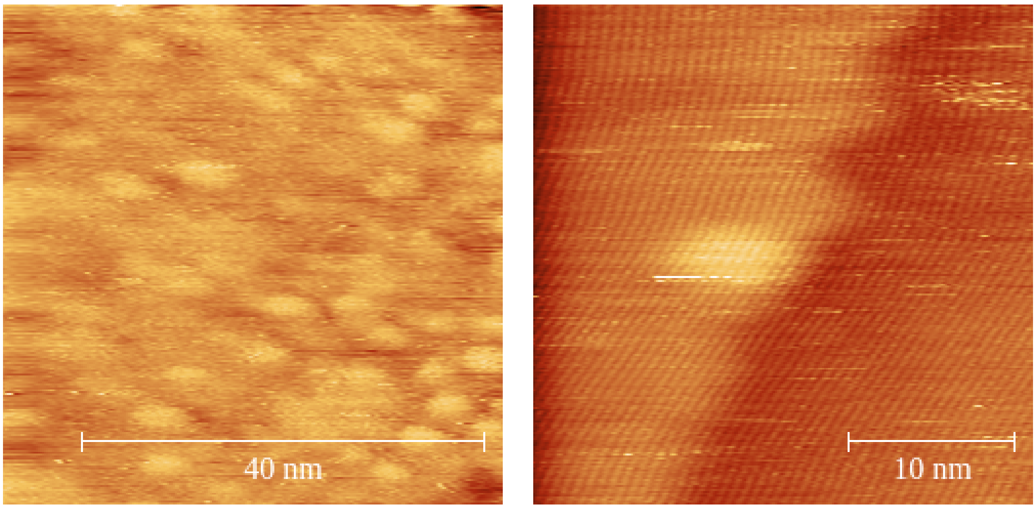

(a) (b)

FIGURE 5.23: Images taken with the home-built STM. Current set point = 0.05 nA, bias voltage = 0.05. (a) Cyt b_{562} D5C apoproteins, 0.5 μM, 5 minutes incubation time (z-range = 0-2.6 nm). (b) Cyt b_{562} SH-LA, 1.5 μM, 10 minutes incubation time (z-range = 0-1 nm).

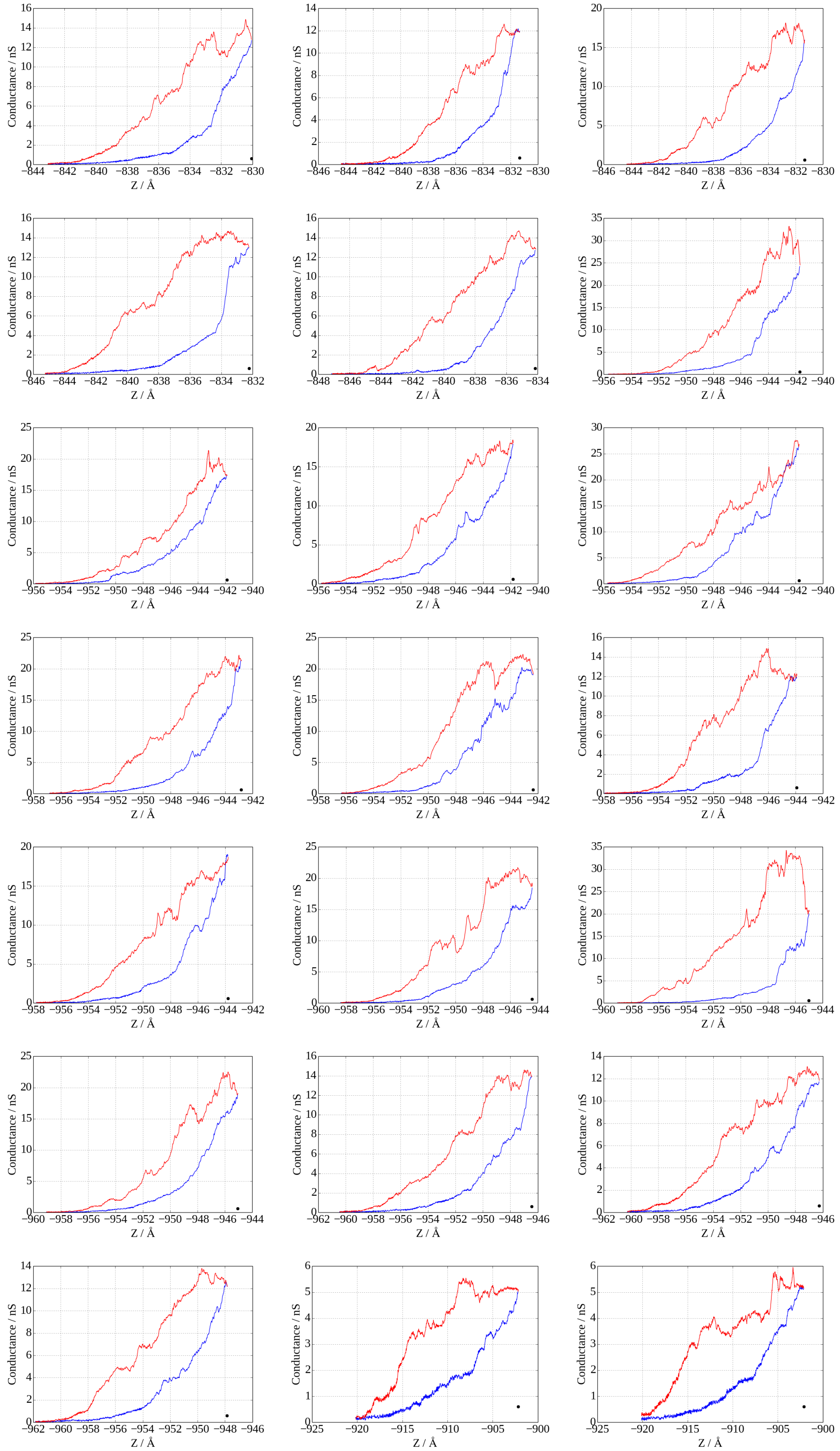

FIGURE 5.24: Conductance curves as a function of tip distance from the substrate for single cyt b_{562} apo D5C molecules on Au(111) under ambient conditions. z-start = 4 $\AA$, z-end -9, -10, -14 $\AA$; current set point = 0.03 nA, bias voltage = -0.05 V.

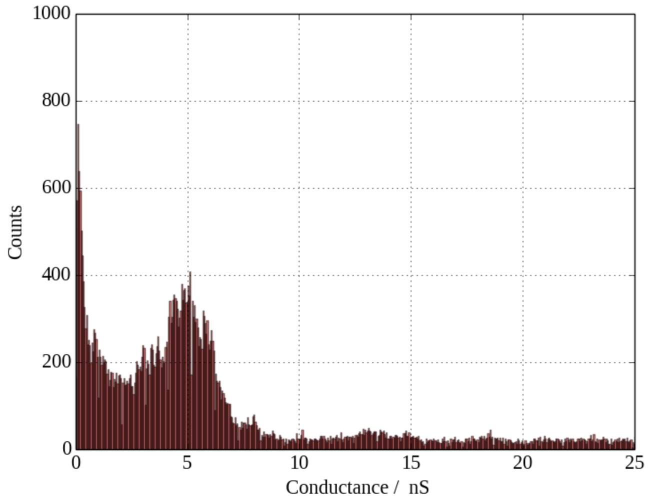

(a)

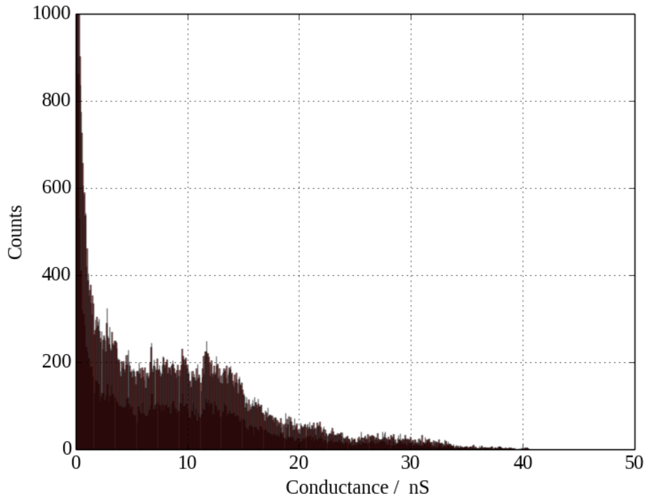

(b)

FIGURE 5.25: Conductance histograms of apo D5C on Au(111). Current set point = 0.03 nA, bias voltage = -0.05 V. (a) Retracting curves; z-start = 4 $\AA$, z-end = -14$\AA$. 156 curves were used to produce this histogram. (b) Retracting curves; z-start = 4 $\AA$, z-end -9 -10 $\AA$. 98 curves were used to produce this histogram.

The comparison of Figure 5.24 with Figure 5.26 suggests that some of the SH-LA proteins may use both thiol groups to bind to gold. In this case, the molecule would lie with the long axis parallel to the substrate (thus leading to a low conductance) and the tip would touch the molecule on some other area that does not involve any thiol group. This would explain the wide range of conductance values in the

I-z curves of Figure 5.26, some of which are well within the range of conductances for the D5C species. The range of conductance values for D5C suggests that the molecule with one thiol, being fixed only one side to the gold substrate, can take different orientations, sometimes lying and other times tilting with respect to the gold surface. The anchoring to the substrate via only one thiol leaves the D5C molecule with high conformational freedom, which may be the reason for the large hysteresis, contrary to the SH-LA variant, whose orientation can be constrained around the axis defined by the two thiol anchoring points, in configurations of different efficiency in order to support the charge transport between substrate and tip. The possibility that, in some cases, both thiols of the SH-LA apoprotein bind to the substrate needs further investigation to be validated. Theoretical-computational investigation (including molecular dynamics simulations) could also help to shed light on this possibility and on the hypotheses here formulated to interpret the conductance curves in Figure 5.24 and 5.26 .

A comparison of the I-z curves with low conductance in Figures 5.16 (SH-LA holoprotein for RH in the range 2.25 to 3.70%) and 5.19 (SH-LA holoprotein for RH in the range 0.82 to 1.01% and temperature around 14 °C) with those in Figures 5.24 (D5C, ambient conditions) and 5.26 (SH-LA apoprotein, ambient conditions), suggests that dry conditions might determine arrangements of the holoproteins on the gold surface similar to those of the apoproteins (and especially D5C), without involvement of the heme cofactor in the charge transport between tip and substrate.

Figure 5.25 represents the conductance histograms which were obtain from I-z curves on cyt b_{562} D5C. Figure 5.25a shows the conductance histogram for the tip retracting mode, with a tip run toward the substrate of 14 $\AA$. Approaching distances of 9 and 10 $\AA$ were considered in Figure 5.25b. A peak was observed around 5 nS for the long tip run of Figure 5.25a. However, no clear peak was observed for the shorter approach distances in Figure 5.25b.

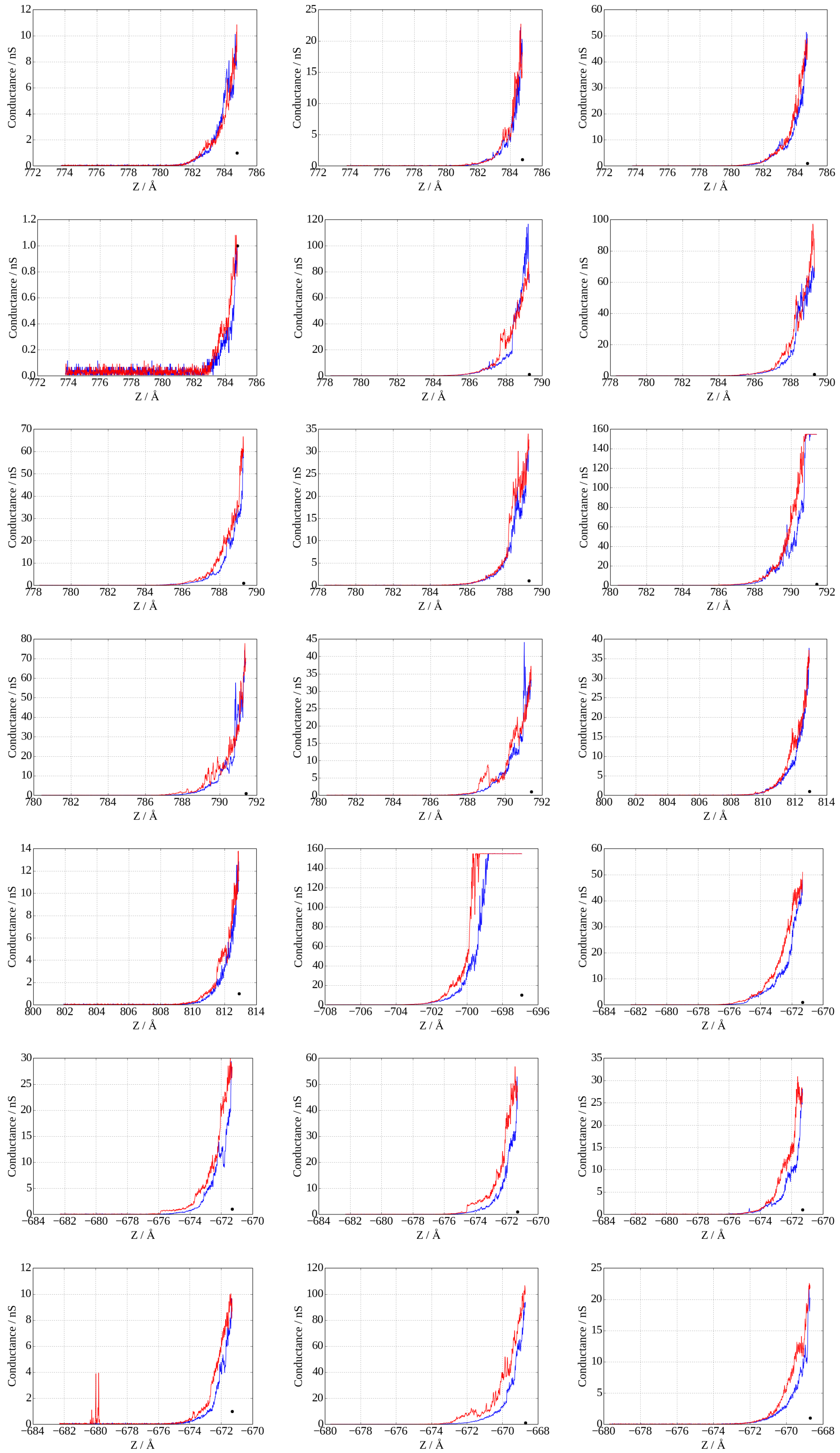

FIGURE 5.26: Conductance curves for single cyt b_{562} apo SH-LA molecules on Au(111) under ambient conditions. z-start = 7 $Å$, z-end = -4 $Å$, current set point = 0.05, 0.5 nA, bias voltage = -0.05 V.

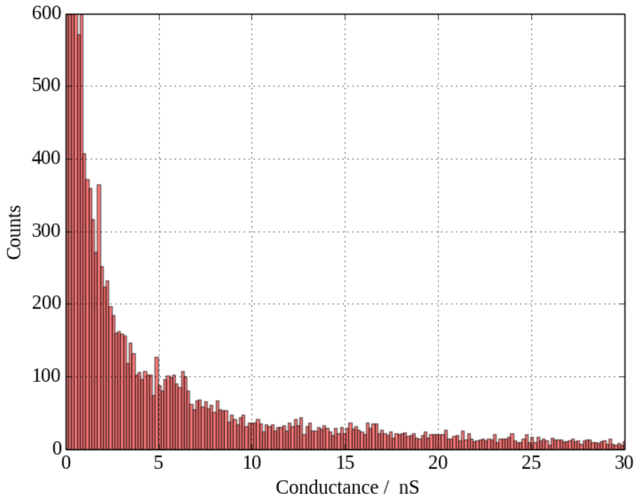

(a)

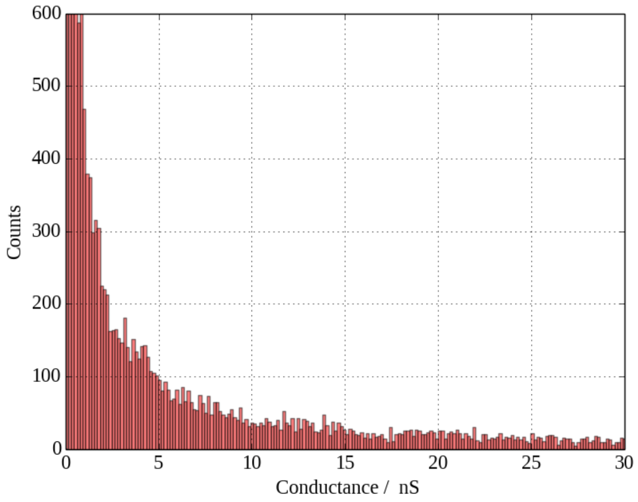

(b)

FIGURE 5.27: Conductance histograms of apo SH-LA molecules on Au(111) under ambient conditions. z-start = 7 $\AA$, z-end = -4 $\AA$, current set point = 0.05 nA, bias voltage = -0.05 V on Au(111). 49 curves were used to produce this histogram. (a) From approaching curves. (b) From retracting curves.

Figure 5.27 shows the conductance histograms for cyt b_{562} apo-H-LA on gold surface, which were obtained from I-z curves with a maximum tip displacement of 4 $\AA$ relative to the set point position in the approaching mode. No clear peak is observed in the conductance histogram. From analysis of the I-z curves, we find that the decay factor β is 1.1 ± 0.5 $\AA^{-1}$ for cyt b_{562} apoproteins.

Different apoproteins have been studied [102, 132, 142], but, to the best of our knowledge, our work provides the first investigation on the conductive properties of cyt b_{562} apoproteins. In Ref [132], Contera *et al*. were able to image pseudoazurin in both holo and apo forms with STM. and they studied the effect of the bias voltage on the proteins and on the contrast of the images. The same group studied dimeric arthrobacter globiformis amine oxidase in the holo and apo forms adsorbed onto Au (111) with STM, investigating how the voltage affects the distance between the two biomolecular units [142]. In this work, we show STM images of cyt b_{562} apoproteins and demonstrate through-protein conduction in the absence of the heme cofactor. The protein residues provide electron tunnelling pathways more favourable than electron tunnelling through the air gap, although the absence of a heme cofactor that can support charge transport through the protein leads to conductance values that are, in general, significantly smaller than those obtained for the holoprotein. This conclusion agrees with the importance of the iron oxide core in the conductance of ferritin that emerged from the study in Ref [143].

Studies on solid-state electron transport (ETp), namely, electron transport through essentially dry proteins (retaining only the tightly bound water needed to preserve the natural conformation) in a solid-state matrix [102, 129] showed that the porphyrin macrocyle itself, rather than the iron center, plays the key role in the transport. In fact, the order of magnitude of the current was not altered by the presence/absence of the iron centre, while the removal of the full prosthetic group reduced significantly the ETp efficiency. More than an order of magnitude increase in the current density was measured in Ref [129] after binding the hemin complex to human serum albumin. According to our measurements, the single-molecule conductance of cyt b_{562} proteins is definitely reduced in the absence of the cofactor, but the current through the apoprotein can still be more than appreciable. Indeed, for some I-z curves, the conductance through the long-axis apoprotein turned out to be of the same order of magnitude as the conductance through the corresponding holoprotein (cf. Figures 5.11 and 5.26). This fact also stresses the role of the molecular orientation in determining the efficiency of the conduction between tip and substrate, and thus the importance of molecular engineering for the implementation of efficient electronic components based on conduction through biomolecules.

5.3.4 I-z Hysteresis

The conductance curves which were obtained from our experimental I-z data and were presented in sections 5.3.1, 2, 3 all show hysteresis between the approaching and retracting curves. For comparison, the conductance measurements were also performed on the Au (111) surface in the absence of protein molecules.

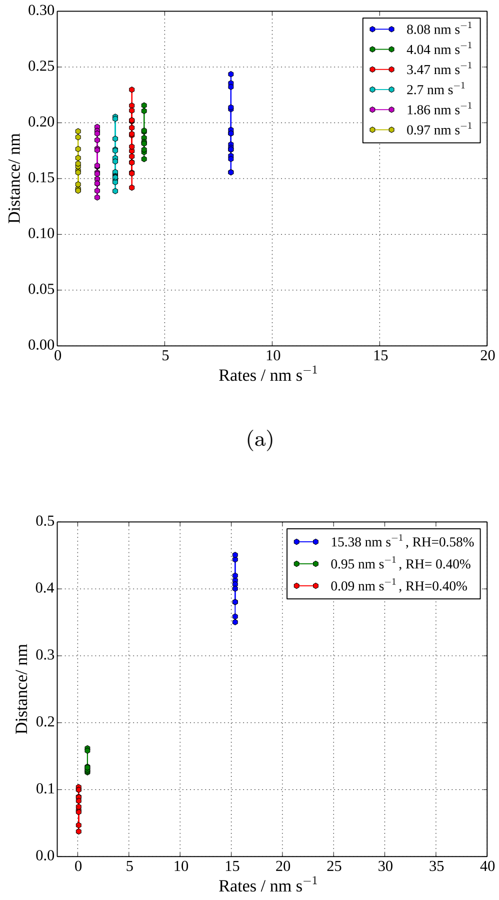

(a)

(b)

FIGURE 5.28: Hysteresis for different tip sweep rates on Au(111) surface. The hysteresis was quantified as the maximum distance between the approaching and retracting curves. (a) Ambient RH. (b) Low RH.

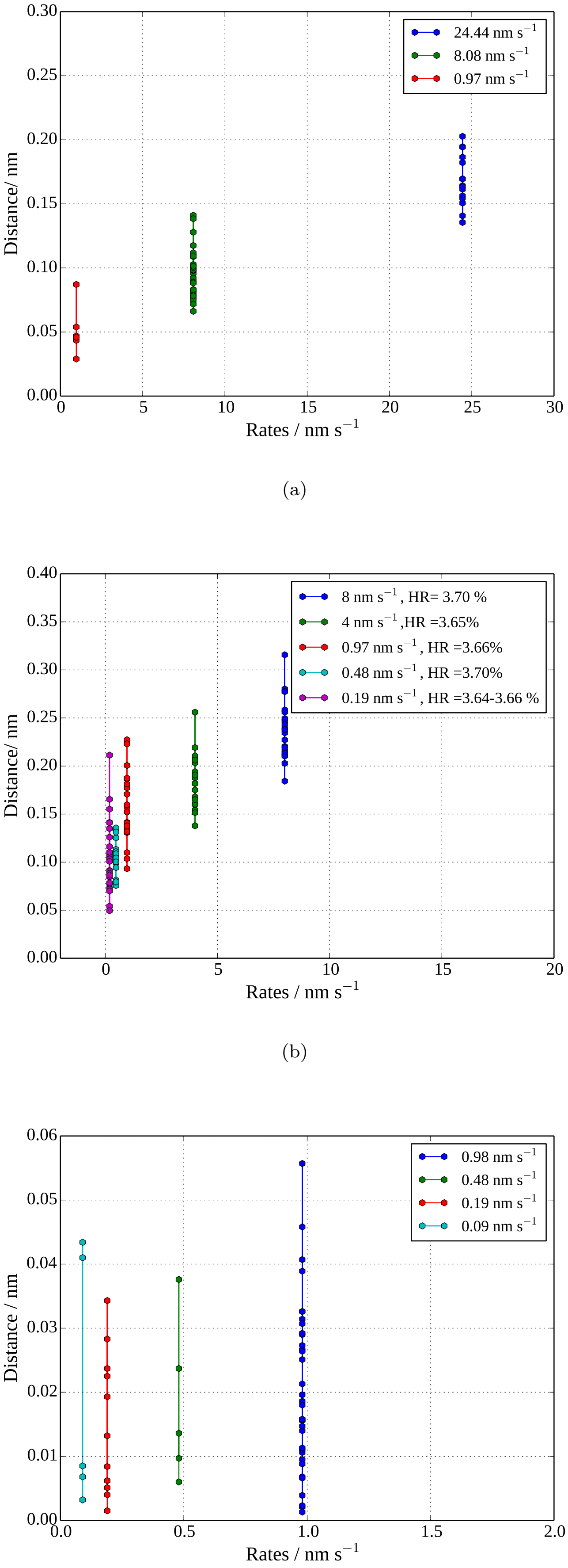

(c)

FIGURE 5.29: Hysteresis at different tip sweep rates for cyt b_{562} on Au(111). (a) SH-SA (b) SH-LA under low RH. (c) SH-LA under high RH

Through most of the hysteresis cycle, hysteresis appears as a shift between the retracting curve, which was measured while the tip was retracted from the surface, and the approaching curve, which was measured while the tip was approached to the surface. The maximum distance of the I-z curves (which is achieved approximately in the middle of the hysteresis cycle) can be considered as a measure of the hysteresis. We investigated the occurrence of hysteresis in the presence and in the absence of proteins, under high and low humidity levels. Moreover, we studied the dependence of the hysteresis on the rate of data acquisition. Figure 5.28 shows that the hysteresis increases with increasing tip sweep rate. This trend is observed at both ambient conditions and low RH, below 2%. Figure 5.29 illustrates the hysteresis as a function of the tip sweep rate for different variants of cyt b_{562} and under different conditions of humidity. Figure 5.30 shows the hysteresis for different apoproteins and holoproteins and on Au(111). The effect of humidity and temperature on hysteresis is shown in Figure 5.31. We again observe an increase in hysteresis with increasing sweep rate. This fact may be ascribed to the reduced capability of the molecular system to equilibrate (achieving a given average conformation) at each z during the tip sweep for increasing sweep rate (see also discussion in section 5.3.1). In support of this explanation. Figure 5.30 shows less hysteresis for the long-axis molecules, which could be explained by a reduced conformational freedom in the presence of two thiol groups that can anchor the molecule. However, the occurrence of hysteresis in the absence of proteins lead us to think that other mechanisms can contribute to produce hysteresis: for example, an intrinsic asymmetry of the STM system in the approaching and retracting modes. However, the hysteresis observed on bare gold samples mostly lack of features frequently observed in the hysteresis cycles of molecules on gold .

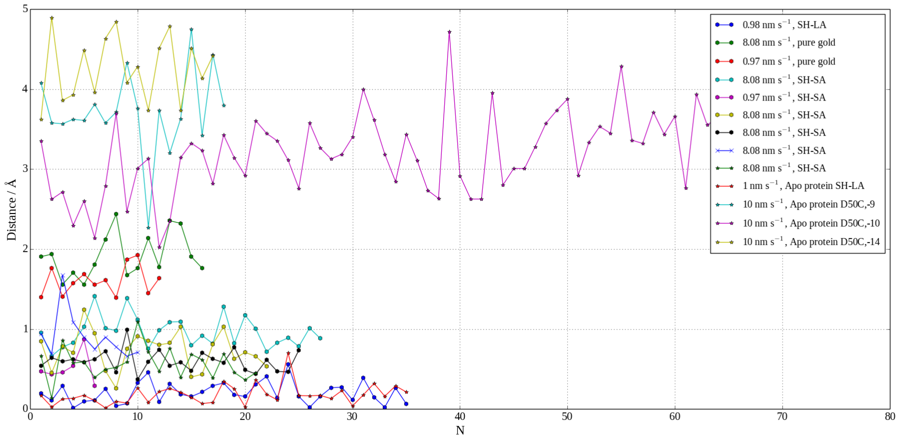

FIGURE 5.30: Hysteresis in sets of I-z curves of different apo and holo cyt b_{562} molecules on Au(111) at high RH. N identifies the selected curves.

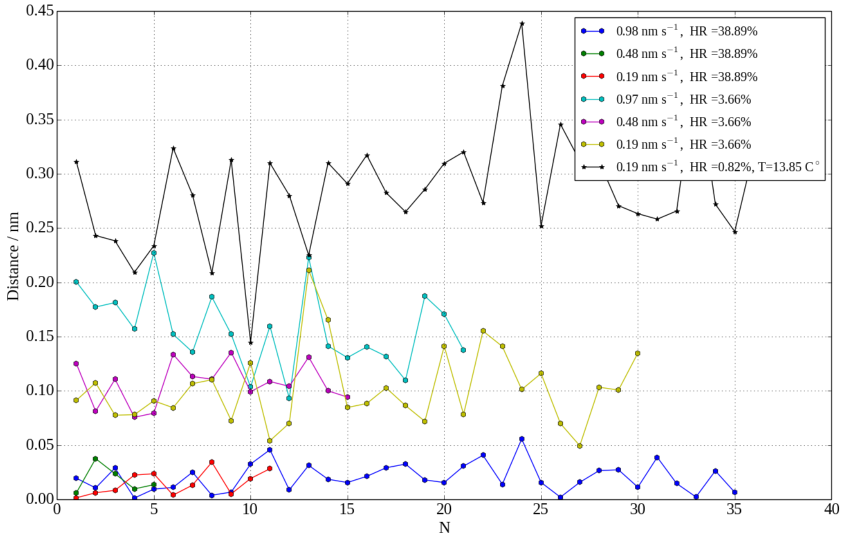

FIGURE 5.31: (a) Hysteresis at different sweep rates for N I-z curves on cyt b_{562} SH-LA under high, low RH (high RH = 38.89%, low RH = 3.66%), high T = ambient (not measured), low T = 13.85 °C.

5.4 STM Imaging of cytb$_{562}$ Proteins Using the Environmental Cell

In these experiments, the imaging of cytb$_{562}$ proteins on Au(111) was performed using the home-built STM in combination with the environmental system, to perform the imaging both under ambient and other conditions of humidity and temperature, and thus to study the effect of these environmental conditions on the height of protein molecules from STM images.

5.4.1 Sample Preparation

The gold bead was annealed following the same method which is described in section 5.2.1, then the bead was imaged using STM in the absence of the protein sample, then incubated by immersion for 5 minutes in a protein solution of cyt b$_{562}$AZF or cyt b$_{562}$ SH-LA of concentration 10 nM and 0.05 μM, respectively. After that, the sample was immersed in deionised water to remove excess protein, and finally dried with nitrogen gas. All the measurements and imaging were performed with the home-built STM system. The imaging and measurements were obtained in ambient conditions as well as under different conditions of humidity and temperature.

5.4.2 Results and Discussion

5.4.2.1 Cyt b$_{562}$ SH-LA, double thiol

Cyt b$_{562}$ SH-LA with two thiols on gold bead was imaged by the Home-built STM to study the effect of humidity and temperature on the height measurements. During all these experiments the STM was placed inside the environmental chamber to control the environmental conditions while taking the data. The employed concentration was 0.05 μM, and the incubation time was 5 minutes. Figure 5.32

shows STM images that were taken under different humidity levels and temperatures. Then, we performed a statistical analysis using many molecules from different STM images, taken under different humidity and temperature conditions. By means of this analysis, we obtained the plots for the heights of individual molecules in Figures 5.33 and 5.34.

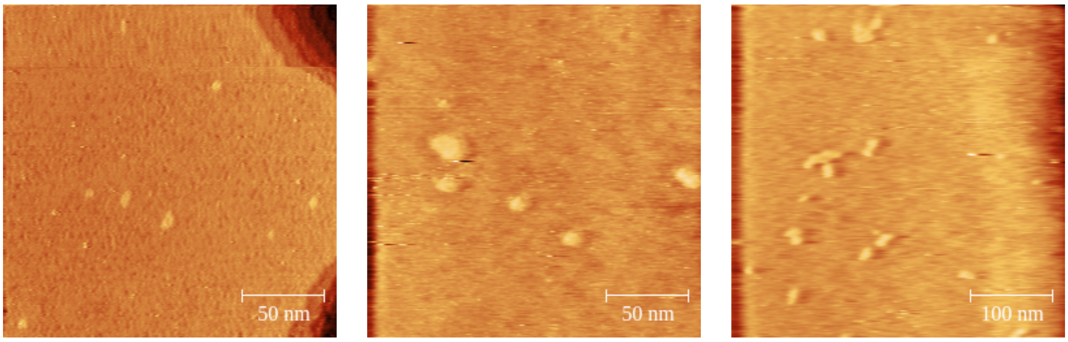

(a) (b) (c)

FIGURE 5.32: STM imaging of cyt b_{562} cysteine,cysteine SH-LA on Au(111). Current set point = 0.05 nA, bias voltage = -0.05 V. (a) T = 23.55 °C, RH = 46.52%, z-range = -69.5-67.5 nm. (b) T = 23.56 °C, RH = 1.16%,z-range = 0-2.9 nm. (c) T = 13.88 °C, RH = 0.95%, z-range = 0-7.4 nm.

According to the data shown in Figure 5.33, on the average the height is bigger at lower RH, which again points to the occurrence of a little less compact molecular conformations at low humidity. However, previous works show that water plays an important role in forming STM images of proteins under ambient conditions [144] [145] Figure 5.34 shows the height of molecules as a function of temperature for individual cyt b_{562} SH-LA molecules on gold bead. The average height is smaller at higher temperature. Thermal orientation motion might be responsible for this behaviour. At higher temperatures the amplitude of the molecular thermal motion increases. This means that the molecule can more easily take conformations that deviate from the vertical to the substrate despite the constrains imposed by the two thiols. In other words, at higher temperatures, the two constrains are expected to be less effective and there is higher probability that the tip touches the molecule while it is at more tilted conformations on the surface. This will explain the smaller height at higher temperature.

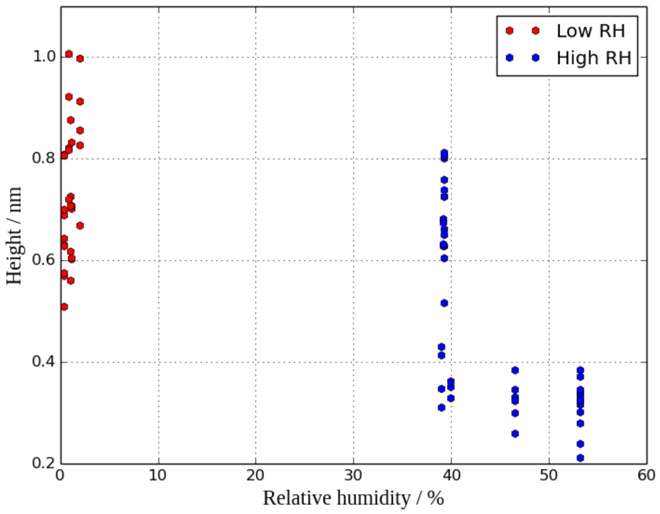

FIGURE 5.33: Apparent height of molecules as a function of relative humidity, from STM imaging of cyt b_{562} SH-LA on Au(111), at T (range = 23.54- 23.59) °C, high RH (range = 36.94-53.18)%, low RH (range = 0.39 to 2.24)%.

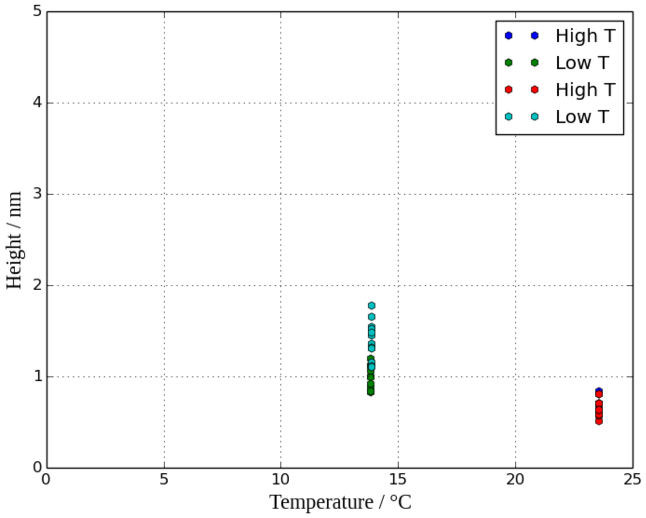

FIGURE 5.34: Apparent height of molecules as a function of temperature, from STM imaging of cyt b_{562} SH-LA molecules on Au(111). Current set point = 0.05 nA, bias voltage = -0.05 V, low T = 13.83 °C and 13.88 °C, high T range = 23.56-23.59 °C, RH = 0.39% to 2.24%.

5.4.2.2 Cyt b_{562} p-azidophenylalanine (azF), thiol

In these experiments, we investigated cyt b_{562} SH-LA with thiol at one end and azF at the other end. A gold bead was the substrate. Imaging was performed using the home-built STM system. Figure 5.35 shows the STM images produced under different conditions of relative humidity and temperature. There are clear differences among the images, especially for the image which was performed under low humidity and low temperature (Figure 5.35c).

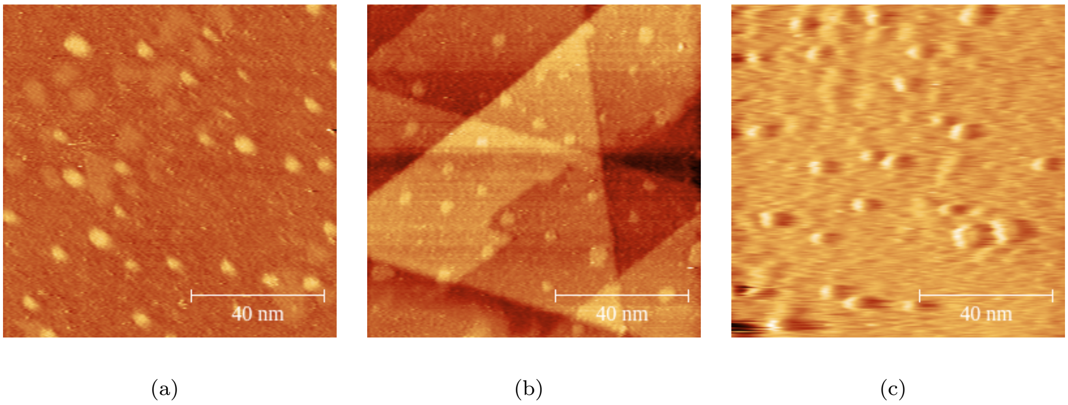

Figure 5.35: STM imaging of Cyt b_{562} AZF,cysteine SH-LA on Au(111). Current set point = 0.05 nA, bias voltage = -0.05 V. (a) High T (20.46 C°), high RH (45.56%), (b) high T (20.46 °C), low RH (0.98%), (c) Low T (10.26 °C), low RH (1.99%).

Figures 5.36 and 5.37 show the height of molecules versus the bias voltage for different values of relative humidity and temperature. We do not see effects of the bias voltage on the heights of the proteins over the explored voltage range. At low humidity the protein molecules look a little higher than at ambient humidity, again in agreement with the other experimental data examined above. In Figure 5.37 we observe a significantly larger height at lower temperature, for which the long-axis molecules appear to be more prevalently oriented vertically to the surface (less orientation variability at lower temperature), similarly to what we observed for the proteins with two thiols.

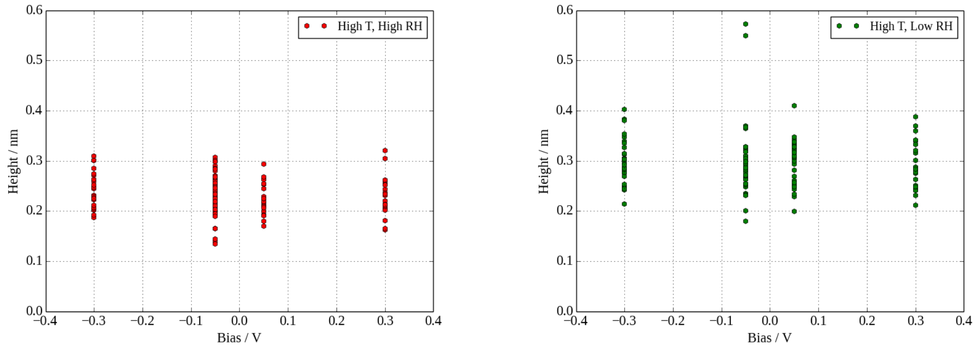

(a) (b)

FIGURE 5.36: Apparent height of molecules versus bias for STM imaging of Cyt b_{562} cysteine,cysteine SH-LA on Au(111). Current set point = 0.05 nA, bias voltage = -0.3, -0.05, 0.05, 0.3 V. (a) High T (about 20.5 °C), high RH (about 45%), (b) high T (about 20.4 °C), low RH (about 1%).

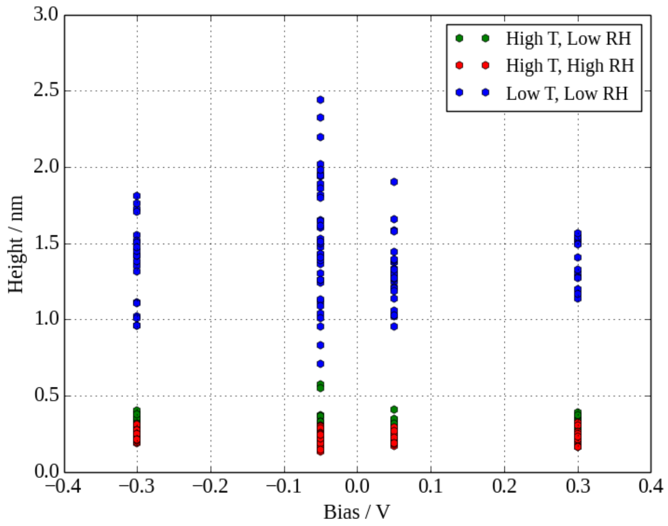

FIGURE 5.37: Apparent height of molecules as a function of bias for different temperatures and humidities, from STM imaging of cyt b_{562} azF, cystein SH-LA molecules on Au(111), Current set point = 0.05 nA, bias voltage = -0.3, -0.05, 0.05, 0.3 V. High T(about 20.5 °C), high RH (about 45%). High T (about 20.4 °C), low RH (about 1%). Low T (about 10.3 °C), low RH (about 2%).

5.5 Conclusions

In this chapter, we studied the charge conduction through differently engineered cyt b_{562} proteins in holo and apo forms attached to Au(111), at different humidity and temperature. Non-ambient conditions were accessible thanks to the use of an environmental cell. The use of different proteins, as well as of different environmental conditions, improved our understanding of the conductive properties that depend on the protein and their distinction from the properties that depend on the environmental influence. A common and important motif of our experimental procedure was that we conducted sample preparation tests prior to conductance measurements, with the aim to select protein concentrations leading to distributions of well-separated molecules on the gold surface. This testing can enable single-molecule measurements, despite the size of the tip. Compared to previous studies, in this work the I-z data were collected during both the tip retraction and approach to the functionalized substrate. The resulting I-z cycles highlighted the occurrence of hysteresis and enabled our study of this nonlinear response of the samples to the changing of tip position. Hysteresis was observed in almost all I-z cycles, as widely reported in this chapter.

The conductance curves show short plateaus which may be related to z ranges of through-molecule conduction, where the biomolecules remain in contact with both electrodes, being only moderately compressed or elongated. In fact, the beta factor values over these z ranges turned out to be compatible with typical values [138] in proteins, thus determining weak dependence of the conductance on z compared to the rapid increase at shorter tip approaches (where the conduction mechanism can also change; see Section 2.4.1) and to the rapid decrease at larger tip distances (where the junction is broken and the beta decay factor increases significantly because of the contribution of the air gap). Some I-z cycles show similar features in the approach and retraction, but generally these features appear over different z ranges and can be different because of the hysteretic behavior. The fraction of I-z cycles with step-like features was about in the range 15 to 20% for the different variants of holoproteins and apoproteins studied, while this fraction was between

0 and 5% for bare gold, which supports our actual measurement of molecular conduction.

The step-like features in the curves of the conductance versus the tip-substrate distance are expected to appear as peaks in the conductance histograms. Plotting these histograms from selected I-z sets of data, we found weak peaks for some samples but no peak for some other molecular species. The smearing of these peaks is a consequence of the fact that the plateaus in the I-z (or conductance-z) curves occurred around different conductance values. This is the case even for different sets of I-z data on the same molecule, due to the fluctuating character of the molecular bridge.

We saw signatures of orientational constraints imposed by the presence of anchoring groups on opposite sides of the LA molecules. For example, the average AFM heights of the SH-SA and SH-LA variants HOLO cyt b562 on Au(111) were in the ranges 2-2.5 nm and 4-5 nm, respectively, (see Section 5.3.1) thus confirming the success of the protein engineering in orienting the biomolecules with either the short or long axis prevalently perpendicular to the substrate. According to our current data and interpretation, protein engineering seems to play an important role in determining the hysteretic response of the molecular system, by limiting the orientation freedom and producing preferential molecular configurations between substrate and tip.

We provided the first investigation of cyt b_{562} apoproteins, showing that these proteins can still assist conduction between the tip and the substrate, despite the absence of the redox cofactor which plays a very important role in charge transfer processes and, in particular, in those at the molecule-substrate interface. The conduction measured between tip and substrate is clearly larger in the presence of the cofactor. Yet, the fact that the cyt b_{562} SH-LA apoprotein can achieve conductance values similar to those of the corresponding holoprotein supports the role of molecular engineering in determining preferential molecular orientations and efficient conduction in molecular junctions. Further experimental and theoretical-computational investigations will hopefully help us to clarify this picture. Our study of the current as a function of the tip-substrate distance in correspondence to individual molecules, under different conditions of humidity and temperature, allowed us to gain deeper understanding on how the effects of these environmental parameters on the structural properties of the biomolecules cause changes in the current.

The comparison of the conductance curves for the cyt b_{562} SH-LA holoprotein under different humidity conditions show that at low humidity the conductance can vary over a wider range and generally takes lower values than in ambient humidity conditions. The conductance turned out to be consistently reduced at very low humidity (RH around 1%) and relatively low temperature (about 14 °C). The beta decay factors are also a little smaller at low humidity than in ambient conditions. The hysteresis shown by the conductance as a function of the substrate-tip distance in the tip approaching and retracting modes increases with low humidity.

The low conductance at very low humidity seems to agree with the fact that biomolecules require some solvent for their normal biological activity. In fact, this activity involves charge transfer processes, in particular in biomolecules with redox centres, and these processes are less efficient in the absence of water, and especially in the absence of structured water in the protein . This needs to be considered in order to implement and optimize the performance of biomolecular materials and devices for electronic applications. Importantly, performing measurements, on single molecules, of the conductance as a function of the tip position along both the approach and retraction runs, we were able to observe hysteresis and other non-linear charge transport effects, some of which can be ascribed to molecular properties and their sensitivity to the environmental conditions of humidity and temperature.

Chapter 6

Oligothiophenes

6.1 Introduction

In this chapter, we present some initial studies of electrical conductance through a type of oligothiophenes molecules, T3-SAc, under ambient conditions and other conditions of humidity and temperature. Oligothiophene molecules are good candidates for molecular electronics applications. Observed effects of environmental humidity and temperature on their electronic properties [146–148], and thus on their conductance, may be exploited for sensing applications. Our work aims to contribute extra knowledge of how the electronic transport through these molecules is affected by humidity and temperature, with relevance to future nanoelectronic applications.

6.2 Oligothiophenes

Oligothiophenes are used in high- technology applications. Their electronic properties can be tuned by functionalizing the oligothiphene backbone [149]. Different molecular wires have been studied to gain knowledge about their behaviour when they are deposited on substrates such as Au(111), and also to understand how environmental conditions can affect their electronic properties [133, 146–148, 150].

The oligothiophene which is studied in this work includes three thiophene units terminated on either side by alkylthiol. Morover, there is one methylene unit between the sulfur contact and the conjugated thiophene rings as can be seen in the structural diagram of Figure 6.1. Molecular wires including different numbers of thiophenes were studied, and it was found that the length of the side-chain can only affect slightly the molecular conduction, while the humidity in the surrounding environment results in increasing the conductance and changing the ET behaviour from activationless to thermally activated [151].

Conductance measurements of molecular wires under different temperatures are vital to obtain information about the mechanism of charge transfer [152]. Also, the conductance of oligothiphene molecular wires is sensitive to the humidity. It was demonstrated that the conductance of oligothiophene decreases when the moisture from the surrounding environment around the molecules is removed. Therefore, it is important to study different oligothiophene molecular wires under different humidity and temperature conditions and provide comparison with conductance measurements at ambient conditions. In this work T3-SAc was studied.

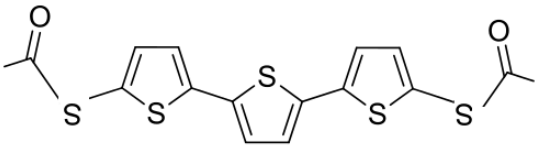

FIGURE 6.1: Structural diagram of the oligothiophenes (T3-SAc) which is studied in this work .

6.3 Oligothiophenes Monolayers Preparation

The preparation procedure consisted of two stages: the first stage involved the annealing of 5×5 mm gold on glass samples from Arrandee. The rough gold surface required to be annealed in order to be used as a substrate for the oligothiophene molecules. Butane flame annealing was used to obtain Au(111) terraces with of about 300 nm. In the flame annealing process, the sample was heated until it glowed dark red and was kept glowing for 10 s, moving it in and out of the flame. The annealing was performed in a dark room to be able to observe the sample glowing. This is important because annealing the sample for longer or shorter time than necessary would result in producing a bent sample or a rough surface. After the heating, the sample was allowed to cool down for 30 s. The whole procedure was repeated three times to get the desired Au(111) surface. Imaging the sample with AFM and STM showed Au(111) terraces of about 300 nm in diameter separated by rough boundaries. The sample was hence ready for the deposition of the molecular wires.

The second stage of the sample preparation was the adsorption of the molecular wires onto the gold samples. We began with the preparation of the oligothiophene solution of concentration 0.1 mM from the oligothiophene powder which we received from University of Liverpool. The T3-SAc powder was dissolved using ethanol until the desired 0.1 mM concentration was achieved. Then, the prepared gold slices on glass samples were immersed in the solution for 90 s. The immersion was followed by rinsing with ethanol. Finally, the samples were dried with nitrogen ready for STM measurements. For the I-z measurements, the home-built STM system was used, adopting the same kind of procedure as for similar measurements on other molecules described in section 5.2.3. The set point current was 6 nA and the bias voltage 0.3 V and the data were obtained at constant speed (40 nm s^{-1}). The measurements were carried out under three different sets of environmental conditions: ambient conditions; low humidity and room temperature; low humidity (purging nitrogen gas for 24 hours) and temperature. The environmental conditions other than ambient ones were achieved by using the home-built STM in combination with the home-built environmental system.

6.4 Results and Discussion

6.4.1 I-z Measurements of conductance through the T3-SAc molecule

The T3-SAc molecular wire on Au(111) was studied. The conductance versus tip-substrate distance (z) curves taken in ambient conditions are shown in Figure 6.2 (RH around 30%, T = 20.5 °C). Figure 6.4 shows the results of the measurements at low RH and ambient temperature (RH of 1-1.6% , T = 20.5 °C), and Figure 6.6 the results for both low humidity (RH = 1.8%) and temperature (T = 6.7 °C). We were able to obtain around 3000 conductance curves in each case. The data were used to produce the conductance histograms in Figures 6.3, 6.5 and 6.7, respectively. According to our data, the current decays exponentially with z, but reaches a plateau at sufficiently large values of z. For thiophenes, similarly to DNA [1, 153], a transition from coherent tunnelling to charge hopping was found for sufficiently long molecules [154]. When charge hopping is the charge transport mechanism at play, the conductance decreases as the inverse molecular length [1], which appears as a small dependence on the molecular length on a logarithm scale (or even independence on the length, if a relatively wide conductance range is showed). However, a single molecular species with given length was used in our experiments, which does not allow us to explain the conductance plateaus in Figure 6.2 (as well as those in Figures 6.4 and 6.6) in terms of a change in charge transport mechanism.

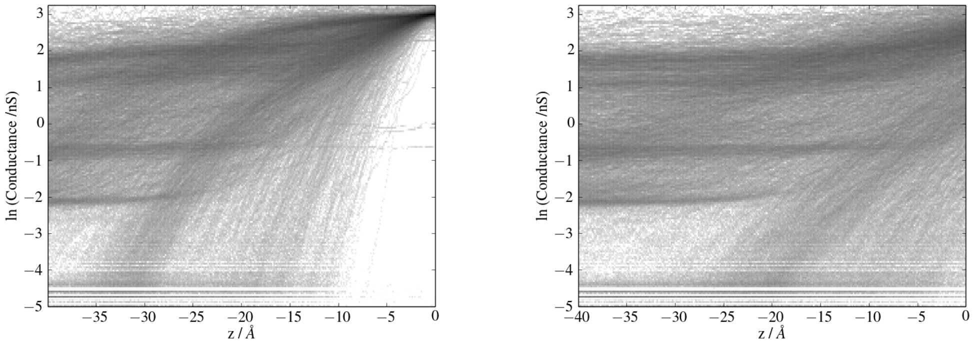

(a)

(b)

Figure 6.2: Conductance curves of T3-SAc on Au(111) under ambient conditions (T = 20.5 °C, RH around 30%), current set point = 6 nA, bias voltage = 0.3 V. (a) Retracting curves. (b) Approaching curves.

Figure 6.3 shows the conductance histograms for the approaching and retracting modes curves in Figure 6.2. All 3060 curves were used to produce the histograms. Sharp peaks are observed around 0.5 nS for both retracting and approaching curves, while modest (and yet appreciable) peaks were observed at about 3-4 nS. The first peak can easily be attributed to the observed conductance plateaus, and we do not attribute a specific physical meaning to this peak based on our current level of understanding. The other peak may instead be related to tip-to-substrate conduction that involves the thiophene molecules for a significant fraction of the tip-substrate gap.

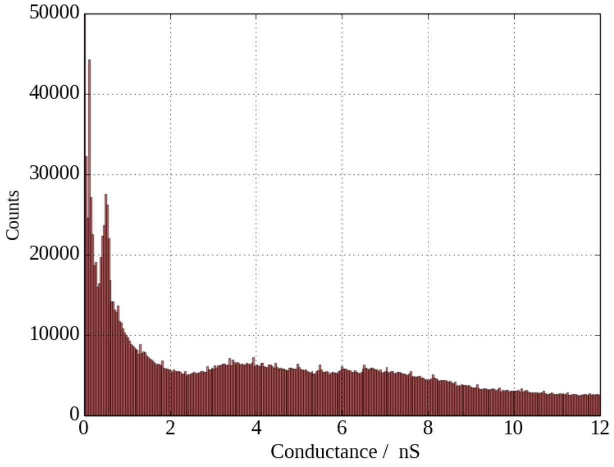

(a)

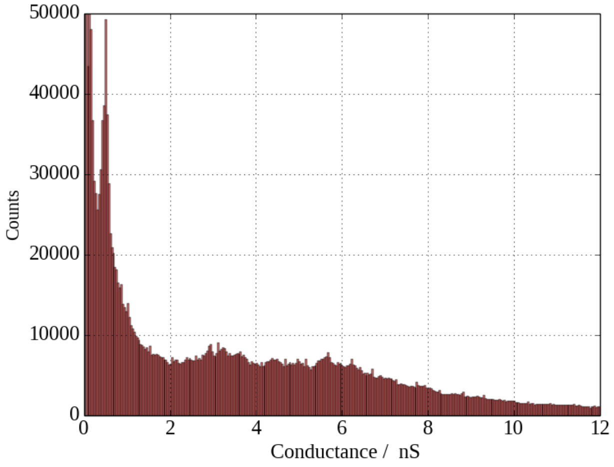

(b)

FIGURE 6.3: Conductance histograms of T3-SAc on Au(111) in ambient conditions (T = 20.5 °C, RH around 30%), current set point = 6 nA, bias voltage = 0.3 V, (3060 curves without selection). (a) Retracting curves. (b) Approaching curves

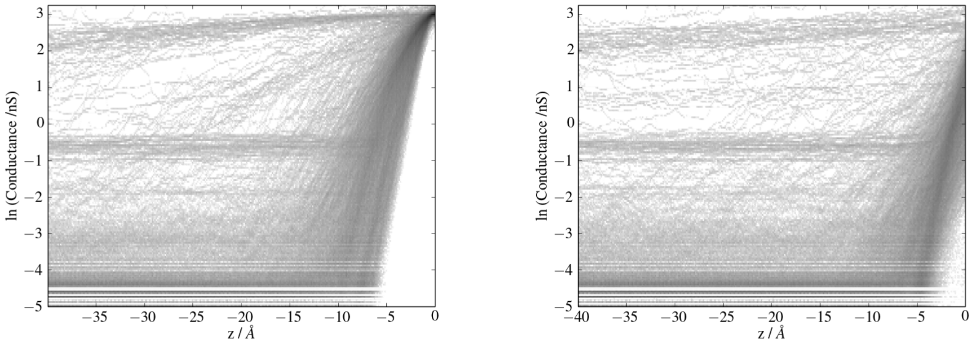

(a)

(b)

FIGURE 6.4: Conductance curves of T3-SAc on A(111) under low RH conditions (T = 20.5 °C, RH around 1-1.6%), current set point = 6 nA, bias voltage = 0.3 V. (a) Retracting curves. (b) Approaching curves.

In Figure 6.4 (low humidity), the retraction and approach conductance curves appear to be a little more symmetric, with respect to each other, compared to those in Figure 6.2. The pertinent conductance histograms in Figure 6.5 show only the conductance peak at 0.5 nS. On the whole, the comparison of Figures 6.3 and 6.5 shows reduced conductance at lower humidity, in agreement with previous findings [146, 151].

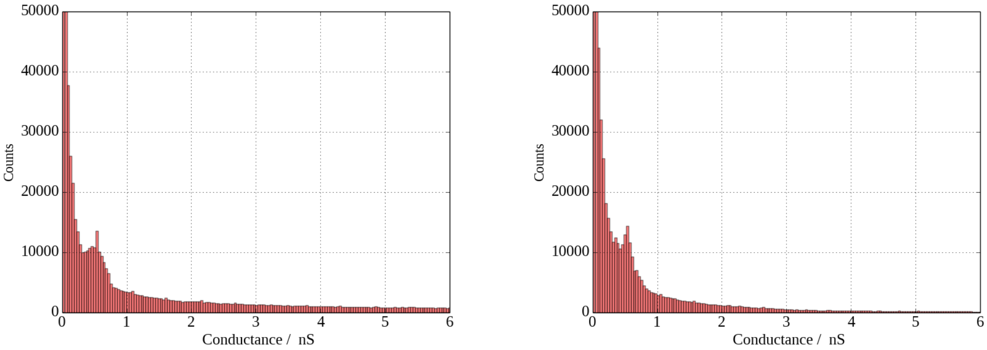

(a)

(b)

FIGURE 6.5: Conductance histograms of T3-SAc on Au(111) under low humidity conditions (T = 20.5 °C, RH around 1-1.6%), current set point = 6 nA, bias voltage = 0.3 V, (2964 curves without selection). (a) Retracting curves. (b) Approaching curves.

The conductance histograms in Figure 6.7 (low humidity and low temperature), in addition to the peak at small conductance,show weak peaks between 2 and 3 nS and around 4 nS. Perhaps, the low temperature (which amounts to less thermal motion) contributes to restore some structural features of the molecular layer that would otherwise be lost because of the low humidity.

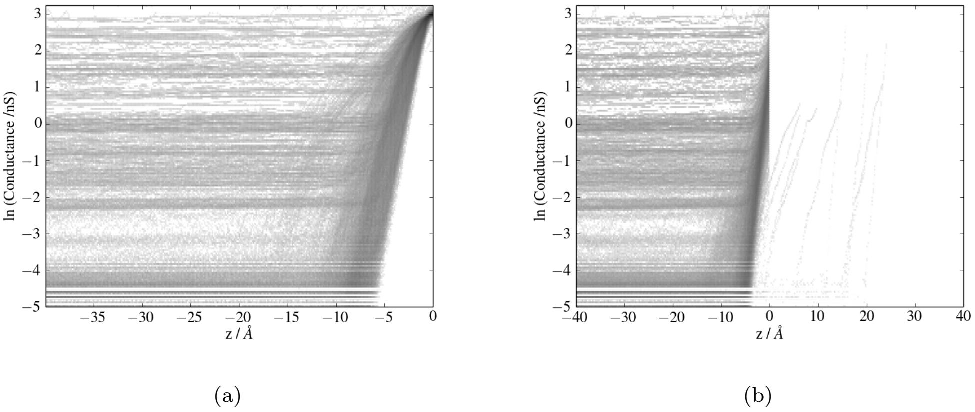

(a)

(b)

FIGURE 6.6: Conductance curves of T3-SAc on A(111) under low RH and low temperature conditions (T = 6.7 °C, RH around 1.8%), current set point = 6 nA, bias voltage = 0.3 V. (a) Retracting curves. (b) Approaching curves.

The employed oligothiophene molecule, the relatively small temperature range explored and the use of two temperatures only do not allow us to explore connections with the work by Lee et al.[155] on the temperature crossover behaviour of conductance in a single oligothiophene molecule. Further investigation is desirable, also with regard to the concomitant effects of relative humidity and temperature changes on the conductance of thiophene molecules.

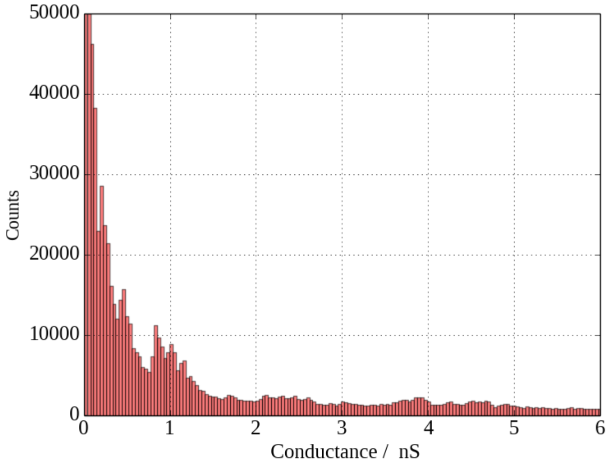

(a)

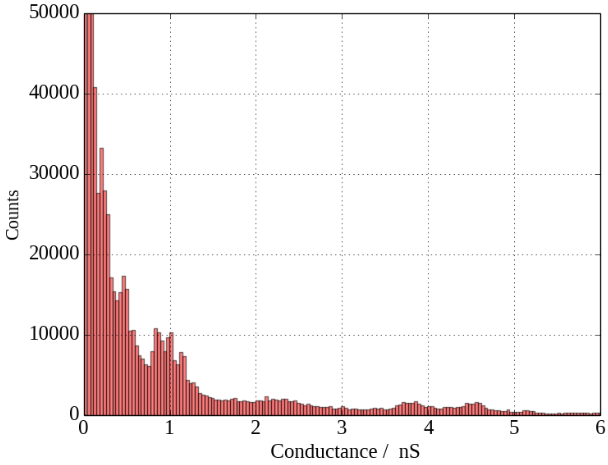

(b)

FIGURE 6.7: Conductance histograms of T3-SAC on Au(111) under low humidity and low temperature conditions (T = 6.7 °C, RH around 1.8%), current set point = 6 nA, bias voltage = 0.3 V, (3272 curves without selection). (a) Retracting curves. (b) Approaching curves.

6.5 Conclusions

In this chapter the conduction of one type of oligothiophene with three thiophene rings (T3-SAc) was investigated in ambient conditions, under low humidity, and under low humidity and temperature. High humidity/low temperature conditions were not explored because we cannot achieve low temperature without driving the system to low humidity first to avoid condensation. The higher thiophene conductance at higher humidity agrees with the previous report that water molecules can interact with the thiophene rings, shifting the electron transport resonances and considerably increasing the conductance [146]. Our measurements for simultaneously decreased humidity and temperature suggest some interplay of the humidity and temperature conditions in determining the molecular conductance, with the possibility that, for low relative humidity, through- thiophene conduction is partly improved at low temperatures. However, this possibility is here proposed on the basis of slight differences between the conductance histograms of Figures 6.5 and 6.7, and thus needs further investigation to be validated or dismissed.

Chapter 7

Conclusions

In the past decade, molecular electronics has evolved towards research areas of interest to Environmental Science, as well as Medicine, which are even more demanding than standard electronics in some regards. For example, this is the case for environmental sensors [15] and biosensors [156], where the molecule is in contact with an unnatural substrate partner and may also be exposed to environmental variables such as humidity and temperature. This study aims to contribute to

(a) understand the current difficulties and limitations in preparing and controlling the electrical properties of heterogeneous interfaces between proteins and conductive materials such as gold and graphene. (b) advance our current knowledge on the structural and electrical properties of biomolecules adsorbed on conductive substrates and exposed to changing humidity and temperature.

The first critical step in point (a) is finding an efficient method to functionalize substrates. We developed two efficient approaches to link protein molecules to graphene. One method consisted in non-covalent bonding through pyrene and was successfully applied to TEM proteins [5]. The other approach consisted in exposing to UV irradiation biomolecules that were engineered by insertion of phenyl azide compound, thus transforming this compound in the reactive nitrene radical (by loss of a N_2 group) to be used for anchoring to graphene. The efficiency and robustness of the approach were tested on three molecular species: cyt b_{562} , TEM beta-lactamases and sfGFP. Samples obtained using pyrene were imaged by AFM, although they were mostly invisible by STM (but both imaging techniques showed the anchoring of cyt b_{562} species). The UV-based method was validated by AFM imaging, as well as by Raman spectroscopy and resistance measurements. Measuring the sheet resistance of samples with sfGFP on graphene, we noticed a dramatic and reversible decrease in resistance under UV irradiation, which paves the way to using the sfGFP anchored to graphene by our method as a photoinduced molecular electric switch.

Differently engineered cyt b_{562} protein molecules on Au(111) were studied for in-depth examination of molecular conduction under different anchoring and environmental conditions. By repeated sample preparation (by immersion) using different protein concentrations and imaging of the samples, we established a suitable range of protein concentrations (0.025 to 0.5 μM) for obtaining functionalized surfaces with sufficiently low protein density to enable single-molecule conductance measurements.

In contrast with most of the available literature, the I-z data for each sample were collected during both tip approach and retraction from the functionalized substrate. Thanks to this choice, we found out that hysteresis is a general feature of the I-z cycles at high enough tip speeds. Plateaus in the I-z curves that are peculiar of conduction through macromolecules, and the similarity of these features in the approach and retraction curves, suggest that the origin of hysteresis may lie in the fact that, for fast tip sweeps, the molecular bridge may sample different regions of its conformational space during the tip approach and retraction. However, the observation of hysteresis by moving the tip on bare gold suggests that intrinsic asymmetry of the STM setup may also contribute to the observed hysteresis.

The step-like features in the I-z curves can be interpreted as the achievement of through-protein conduction after closing the gap between the approaching tip and the molecule. The fraction of I-z curves with such features was approximately in the range 15 to 20% for the different variants of cyt b_{562} holo- and apo-proteins studied, while this fraction was at most 5% for bare Au(111). The significant difference between these two ranges supports the fact that we were actually measuring molecular conduction.

The plateaus in the I-z curves are expected to appear as peaks in conductance histograms. However, when gathering together data from a number of I-z curves, we obtained weak peaks for some samples and no peak for some other molecular species. In fact, the plateaus in different I-z curves occur at a range of different currents, thus leading to smearing of the peaks in the histograms.

Deeper understanding of the connection between SPM images, I-z data and structural properties of the protein bridge can be gained by studying differently engineered proteins of the same kind and apoproteins. Our data seem to point to reduced conformational freedom of LA cyt b_{562}, due to its anchoring through both thiols to substrate and tip. The fact that the LA apoprotein can sometimes achieve conductance values typical of the corresponding holoprotein suggests a major role of the protein configuration in the STM setup in determining such conductance values and stresses the importance of molecular engineering to achieve better control of the functionalized surface properties in the future. In general, our investigation of cyt b_{562} apoproteins shows that these proteins can still support current, although the conductance is, on the average, significantly less than in the presence of the redox cofactor.

A home-built environmental cell in combination with STM was here used to study the conductance of differently engineered cyt b_{562} proteins on Au(111), under different humidity and temperature conditions. We found that the conductance of cyt b_{562} is smaller at lower relative humidity and further decreased when also temperature is reduced. Measuring the conductance as a function of the tip-substrate distance in both tip approaching and retracting modes revealed the occurrence of hysteresis. The engineered cyt b_{562} with two thiols in the long axis led to less hysteresis in the conductance and larger protein height on gold (from AFM) compared to the protein with thiols in the short axis. Our results stress the importance of protein engineering to control the electrical properties of functionalized surfaces.

The use of a home-built environmental cell enabled our measurements of molecular conduction at low humidity/ambient temperature and low humidity/low temperature (compared to ambient conditions), while measurements at ambient humidity/low temperature were hindered by condensation of the humidity in the environment. We observed that the conductance of cyt b_{562} is reduced by lowering the relative humidity and further decreased by also lowering the temperature. In the present research project, the investigation of humidity and temperature effects on the conduction through oligothiophene molecules was also started.

7.1 Future Directions

In the future, it would be desirable to use the environmental cell for systematic imaging and conductance study of holoprotein and apoprotein molecules under suitable ranges of humidity and temperature. The study of molecular conduction at temperatures higher than common ambient conditions would also be desirable, because temperature may increase above ambient conditions depending on the operating electronic device [157], and the conductive behaviour of the biomolecules at relatively high temperatures should thus be investigated.

An important direction for continuing and extending the present work would be the study of molecular conduction on graphene (and of the effect of functionalization on the conductance through the graphene sheet). In particular, the here observed UV-induced conductance switching should be investigated and related to the electronic properties of sfGFP by means of combined experimental and theoretical work. For example, experimentally, the first step would be the study of the conductance switching at the wavelengths of maximum absorption for sfGFP204.

As discussed above, this study shows that the conductance in the STM setup decreases by lowering humidity. This might be correlated with the fact that the functional charge-transfer activity of redox proteins generally takes place in the presence of some aqueous environment. Future experimental and computational studies addressing this point would be desirable. Ultimately, the first working transistors based on Shockley's idea used electrolytes, and the idea of using aqueous solutions as the gate medium is back in very recent research on water-gated organic transistors [158]. Thus, the work presented in this dissertation and its possible future extensions seem to be timely and of broad scientific interest.

Bibliography

[1] A Nitzan. *Chemical Dynamics in Condensed Phases: Relaxation, Transfer and Reactions in Condensed Molecular Systems.* Oxford University Press. Oxford, 2006.

[2] A. Migliore, S. Corni, R. Di Felice, and E. Molinari. First-principles density-functional theory calculations of electron-transfer rates in azurin dimers. *Journal of Chemical Physics*, 124(6), 2006.

[3] R.J. Hamers and D.F. Padowitz. Methods of Tunneling Spectroscopy with the STM, 1993.

[4] Eduardo A. Della Pia, J. Emyr MacDonald, Martin Elliott, and D. Dafydd Jones. Direct binding of a redox protein for single-molecule electron transfer measurements. *Small*, 8(15):2341–2344, 2012.

[5] Andrew M. Hartley, Athraa J. Zaki, Adam R. McGarrity, Cecile Robert-Ansart, Andriy V. Moskalenko, Gareth F. Jones, Monica F. Craciun, Saverio Russo, Martin Elliott, J. Emyr Macdonald, and D. Dafydd Jones. Functional modulation and directed assembly of an enzyme through designed non-natural post-translation modification. *Chem. Sci.*, 6:3712–3717, 2015.

[6] Andrew M Hartley. Using a reprogrammed genetic code to modulate protein activity by novel post-translational control A thesis submitted to Cardiff University for the. (September), 2014.

[7] Torsten Sendler, Katharina Luka-Guth, Matthias Wieser, Lokamani, Jannic Wolf, Manfred Helm, Sibylle Gemming, Jochen Kerbusch, Elke Scheer,

Thomas Huhn, and Artur Erbe. Light-Induced Switching of Tunable Single-Molecule Junctions. *Advanced Science*, 2:1500017, 2015.

[8] Chuancheng Jia, Agostino Migliore, Na Xin, Shaoyun Huang, Jinying Wang, Qi Yang, Shuopei Wang, Hongliang Chen, Duoming Wang, Boyong Feng, Zhirong Liu, Guangyu Zhang, Da-Hui Qu, He Tian, Mark A Ratner, H Q Xu, Abraham Nitzan, and Xuefeng Guo. Covalently bonded single-molecule junctions with stable and reversible photoswitched conductivity. *Science*, 352(6292):1443–1445, 2016.

[9] Chen Li, Miaoyin Liu, Neil G Pschirer, Martin Baumgarten, and Klaus Muellen. Polyphenylene-Based Materials for Organic Photovoltaics. *Chemical Reviews (Washington, DC, United States)*, 110(Copyright (C) 2011 American Chemical Society (ACS). All Rights Reserved.):6817–6855, 2010.

[10] Luyao Lu, Tianyue Zheng, Qinghe Wu, Alexander M. Schneider, Donglin Zhao, and Luping Yu. Recent Advances in Bulk Heterojunction Polymer Solar Cells. *Chemical Reviews*, 115(23):12666–12731, 2015.

[11] Lianjun Zheng, Nicholas F. Polizzi, Adarsh R. Dave, Agostino Migliore, and David N. Beratan. Where Is the Electronic Oscillator Strength? Mapping Oscillator Strength across Molecular Absorption Spectra. *The Journal of Physical Chemistry A*, 120(11):1933–1943, 2016.

[12] Michael Galperin and Abraham Nitzan. Molecular optoelectronics: the interaction of molecular conduction junctions with light. *Physical Chemistry Chemical Physics*, 14(26):9421, 2012.

[13] Wei Du, Tao Wang, Hong-Son Chu, Lin Wu, Rongrong Liu, Song Sun, Wee Kee Phua, Lejia Wang, Nikodem Tomczak, and Christian A. Nijhuis. On-chip molecular electronic plasmon sources based on self-assembled monolayer tunnel junctions. *Nature Photonics*, 10(4):274–280, 2016.

[14] Matthew T. Meredith and Shelley D. Minteer. Biofuel Cells: Enhanced Enzymatic Bioelectrocatalysis. *Annual Review of Analytical Chemistry*, 5(1):157–179, 2012.

[15] Ron Naaman. Molecular controlled nano-devices. *Physical Chemistry Chemical Physics*, 13(29):13153–13161, 2011.

[16] Audrey Sassolas, Lo??c J. Blum, and B??atrice D. Leca-Bouvier. Immobilization strategies to develop enzymatic biosensors. *Biotechnology Advances*, 30(3):489–511, 2012.

[17] Agostino Migliore, Ron Naaman, and David N Beratan. Sensing of molecules using quantum dynamics. *Proceedings of the National Academy of Sciences*, 112(19):E2419–E2428, 2015.

[18] Daniel T. Simon, Erik O. Gabrielsson, Klas Tybrandt, and Magnus Berggren. Organic Bioelectronics: Bridging the Signaling Gap between Biology and Technology. *Chemical Reviews*, page acs.chemrev.6b00146, 2016.

[19] Stefano Sanvito. Molecular spintronics. *Chemical Society Reviews*, 40(6):3336, 2011.

[20] Ron Naaman and David H Waldeck. Spintronics and Chirality: Spin Selectivity in Electron Transport Through Chiral Molecules. *Annual review of physical chemistry*, 66(January):263–281, 2015.

[21] S Yamamoto, S Nakazawa, K Sugisaki, K Sato, K Toyota, D Shiomi, and T Takui. Adiabatic quantum computing with spin qubits hosted by molecules. *Physical Chemistry Chemical Physics*, 17(4):2742–2749, 2015.

[22] Baghali G. Mathapa and Vesselin N. Paunov. Fabrication of viable cyborg cells with cyclodextrin functionality. *Biomater. Sci.*, 2(2):212–219, 2014.

[23] Mark Ratner. A brief history of molecular electronics. *Nature Nanotechnology*, 8(6):378–381, 2013.

[24] Hylke B Akkerman, Paul W M Blom, Dago M de Leeuw, and Bert de Boer. Towards molecular electronics with large-area molecular junctions. *Nature*, 441(7089):69–72, 2006.

[25] Fang Chen, Joshua Hihath, Zhifeng Huang, Xiulan Li, and N.J. Tao. Measurement of Single-Molecule Conductance. *Annual Review of Physical Chemistry*, 58(1):535–564, 2007.

[26] Lanlan Sun, Yuri A Diaz-Fernandez, Tina A Gschneidtner, Fredrik Westerlund, Samuel Lara-Avila, and Kasper Moth-Poulsen. Single-molecule electronics: from chemical design to functional devices. *Chem. Soc. Rev. Chem. Soc. Rev*, 43(43):7378–7411, 2014.

[27] Julio A. Camarero. Recent developments in the site-specific immobilization of proteins onto solid supports. *Biopolymers - Peptide Science Section*, 90(3):450–458, 2008.

[28] Eduardo Antonio and Della Pia. cytochrome b 562 bonded to metallic electrodes. (March), 2011.

[29] Maryam Raeeszadeh-Sarmazdeh, Ranganath Parthasarathy, and Eric T. Boder. Site-specific immobilization of protein layers on gold surfaces via orthogonal sortases. *Colloids and Surfaces B: Biointerfaces*, 128:457–463, 2015.

[30] Eduardo Antonio Della Pia, Qijin Chi, J Emyr Macdonald, Jens Ulstrup, D Dafydd Jones, and Martin Elliott. Fast electron transfer through a single molecule natively structured redox protein. *Nanoscale*, 4(22):7106–13, 2012.

[31] D. Dafydd Jones and Paul D. Barker. Controlling self-assembly by linking protein folding, DNA binding, and the redox chemistry of heme. *Angewandte Chemie - International Edition*, 44(39):6337–6341, 2005.

[32] Guest Editor, Pablo Etchegoin, Anja Kranich, Hendrik Naumann, Fernando P Molina-heredia, Justin Moore, T Randall Lee, Sophie Lecomte, Miguel A De, Peter Hildebrandt, Daniel H Murgida, Phys Chem, Nicolás G Tognalli, Pablo Scodeller, Victoria Flexer, Alejandra Ricci, Mario Tagliazucchi, Ernesto J Calvo, Seth Michael Morton, Ebo Ewusi-annan, Lasse Jensen, Juan Soto, Paulo Ribeiro-claro, and Juan Carlos Otero. Quo vadis

surface-enhanced Raman scattering? *Physical Chemistry Chemical Physics*, 11(34):7348, 2009.

[33] Wayne R Edwards, Abigail J Williams, Josephine L Morris, Amy J Baldwin, Rudolf K Allemann, and D Dafydd Jones. Regulation of β-lactamase activity by remote binding of heme: Functional coupling of unrelated proteins through domain insertion. *Biochemistry*, 49(31):6541–6549, 2010.

[34] Sowmya Viswanathan, Tharangattu N. Narayanan, Kiana Aran, Kathryn D. Fink, Jacobo Paredes, Pulickel M. Ajayan, Slawomir Filipek, Przemyslaw Miszta, H. Cumhur Tekin, Fatih Inci, Utkan Demirci, Pingzuo Li, Kirill I. Bolotin, Dorian Liepmann, and V. Renugopalakrishanan. Graphene-protein field effect biosensors: Glucose sensing. *Materials Today*, 18(9):513–522, 2015.

[35] Jingquan Liu, Zhen Liu, Colin J. Barrow, and Wenrong Yang. Molecularly engineered graphene surfaces for sensing applications: A review. *Analytica Chimica Acta*, 859:1–19, 2015.

[36] M Weissbluth. *Atoms and Molecules.* Academic Press, New York, 1978.

[37] R. a. Marcus. On the Theory of Oxidation-Reduction Reactions Involving Electron Transfer. I. *The Journal of Chemical Physics*, 24(5):966, 1956.

[38] D DeVault. *Quantum-mechanical tunneling in biological systems*, volume second edi. Cambridge University Press, Cambridge, 1984.

[39] R. A. Marcus and Norman Sutin. Electron transfers in chemistry and biology. *BBA Reviews On Bioenergetics*, 811(3):265–322, 1985.

[40] Rudolph A. Marcus. Electron transfer reactions in chemistry. Theory and experiment, 1993.

[41] David W Small, Dmitry V Matyushov, and Gregory a Voth. The theory of electron transfer reactions: what may be missing? *J. Am. Chem. Soc.*, 125(5):7470–7478, 2003.

[42] Agostino Migliore, Nicholas F Polizzi, Michael J Therien, and David N Beratan. The Biochemistry and Theory of Proton Coupled Electron Transfer. *Chem.Rev.*, 114:3381–3465, 2014.

[43] A M Kuznetsov and J Ulstrup. *Electron Transfer in Chemistry and Biology.* John Wiley and Sons, New York, 1999.

[44] R A Marcus. Chemical and Electrochemical Electron-Transfer Theory. *Annu. Rev. Phys. Chem.*, 15:155–196, 1964.

[45] Christopher E D Chidsey, New Series, and No Feb. Free Energy and Temperature Dependence of Electron Transfer at the Metal-Electrolyte Interface. *Science*, 251:919–922, 1991.

[46] Keith B. Oldham and Jan C. Myland. On the evaluation and analysis of the Marcus-Hush-Chidsey integral. *Journal of Electroanalytical Chemistry*, 655(1):65–72, 2011.

[47] Agostino Migliore and Abraham Nitzan. Nonlinear charge transport in redox molecular junctions: A marcus perspective. *ACS Nano*, 5:6669–6685, 2011.

[48] Agostino Migliore and Abraham Nitzan. On the evaluation of the Marcus-Hush-Chidsey integral. *Journal of Electroanalytical Chemistry*, 671:99–101, 2012.

[49] C.Cohen-Tannoudji B. Diu and F Laloe. *Quantum Mechanics*, volume 1. Hermann, Paris, 1977.

[50] Agostino Migliore and Abraham Nitzan. Irreversibility and hysteresis in redox molecular conduction junctions. *Journal of the American Chemical Society*, 135(25):9420–9432, 2013.

[51] Massimiliano Di Ventra. *Electrical Transport in Nanoscale Systems.* Cambridge University Press, New York,, 2008.

[52] B Alberts, A Johnson, J Lewis, M Raff, K Roberts, and P And Walter. Molecular Biology of the Cell - NCBI Bookshelf, 2007.

[53] G. Bar, L. Delineau, R. Brandsch, M. Bruch, and M. H. Whangbo. Importance of the indentation depth in tapping-mode atomic force microscopy study of compliant materials. *Applied Physics Letters*, 75(26):4198–4200, 1999.

[54] Giuseppe Maruccio, Adriana Biasco, Paolo Visconti, Alessandro Bramanti, Pier Paolo Pompa, Franco Calabi, Roberto Cingolani, Ross Rinaldi, Stefano Corni, Rosa Di Felice, Elisa Molinari, Martin P. Verbeet, and Gerard W. Canters. Towards protein field-effect transistors: Report and model of a prototype. *Advanced Materials*, 17(7):816–822, 2005.

[55] Ye Lu, Mitchell B. Lerner, Zhengqing John Qi, Joseph J. Mitala, Jong Hsien Lim, Bohdana M. Discher, and A. T. Charlie Johnson. Graphene-protein bioelectronic devices with wavelength-dependent photoresponse. *Applied Physics Letters*, 100(3):10–12, 2012.

[56] Kristoffer Famm. A jump-start for electroceuticals. *Nature*, 496:159–61, 2013.

[57] Baghali G. Mathapa and Vesselin N. Paunov. Fabrication of viable cyborg cells with cyclodextrin functionality. *Biomater. Sci.*, 2(2):212–219, 2014.

[58] Emil Paleček, Jan Tkáč, Martin Bartošík, Tomáš Bertók, Veronika Ostatná, and Jan Paleček. Electrochemistry of Nonconjugated Proteins and Glycoproteins. Toward Sensors for Biomedicine and Glycomics. *Chemical Reviews*, 115(5):2045–2108, 2015.

[59] Mohan Sarovar, Akihito Ishizaki, Graham R. Fleming, and K. Birgitta Whaley. Quantum entanglement in photosynthetic light-harvesting complexes. *Nature Physics*, 6(6):462–467, 2010.

[60] A. Ishizaki and G. R. Fleming. Quantum Coherence in Photosynthetic Light Harvesting. *Annu. Rev. Cond. Mat.*, 3(1):333–361, 2012.

[61] Timothy M Swager. Conjugated Amplifying Polymers for Optical Sensing Applications. 2013.

[62] Eduardo Antonio Delia Pia, Qijin Chi, D. Dafydd Jones, J. Emyr MacDonald, Jens Ulstrup, and Martin Elliott. Single-molecule mapping of long-range electron transport for a cytochrome b562 variant. *Nano Letters*, 11:176–182, 2011.

[63] Umberto Prisco, Carl Leung, Chrisa Xirouchaki, Celine H Jones, John K Heath, and Richard E Palmer. Residue-specific immobilization of protein molecules by size-selected clusters. *Journal of the Royal Society, Interface / the Royal Society*, 2(3):169–75, 2005.

[64] Emil Paleĉek, Jan Tkàĉ, Martin Bartoŝík, Tomáŝ Bertók, Veronika Ostatná, and Jan Paleĉek. Electrochemistry of nonconjugated proteins and glycoproteins. Toward sensors for biomedicine and glycomics. *Chemical Reviews*, 115(5):2045–2108, 2015.

[65] J J Davis, D Djuricic, K K Lo, E N Wallace, L L Wong, and H A Hill. A scanning tunnelling study of immobilised cytochrome P450cam. *Faraday Discuss*, (116):15–75, 2000.

[66] Zengxing Zhang, Helin Huang, Xiaomei Yang, and Ling Zang. Tailoring Electronic Properties of Graphene by π À π Stacking with. pages 2897–2905, 2011.

[67] Kenath Priyanka Prasad, Yun Chen, and Peng Chen. Supporting information Three-dimensional graphene - carbon nanotube hybrid for high- performance enzymatic biofuel cells. (C):1–4, 2014.

[68] Fabio Arnesano, Lucia Banci, Ivano Bertini, Jasmin Faraone-Mennella, Antonio Rosato, Paul D. Barker, and Alan R. Fersht. The solution structure of oxidized Escherichia coli cytochrome b562. *Biochemistry*, 38(27):8657–8670, 1999.

[69] M Ormö, Andrew B Cubitt, Karen Kallio, Larry a Gross, Roger Y Tsien, S J Remington, Mats Ormo, Andrew B Cubitt, Karen Kallio, Larry a Gross, Roger Y Tsien, S James Remingtont, M Ormö, Andrew B Cubitt, Karen

Kallio, Larry a Gross, Roger Y Tsien, and S J Remington. Crystal structure of the Aequorea victoria green fluorescent protein., 1996.

[70] Samuel Reddington, Peter Watson, Pierre Rizkallah, Eric Tippmann, and D Dafydd Jones. Genetically encoding phenyl azide chemistry: new uses and ideas for classical biochemistry. *Biochemical Society Transactions*, 41(5):1177–1182, 2013.

[71] Susan S. Taylor, Choel Kim, Dominico Vigil, Nina M. Haste, Jie Yang, Jian Wu, and Ganesh S. Anand. Dynamics of signaling by PKA. *Biochimica et Biophysica Acta - Proteins and Proteomics*, 1754:25–37, 2005.

[72] May C. Morris. Fluorescent biosensors - Probing protein kinase function in cancer and drug discovery. *Biochimica et Biophysica Acta - Proteins and Proteomics*, 1834(7):1387–1395, 2013.

[73] J W Chin, S W Santoro, A B Martin, D S King, L Wang, and P G Schultz. Addition of p-Azido-L-phenylalanine to the Genetic Code of Escherichia coli. *J. Am. Chem. Soc.*, 124(31):9026–9027, aug 2002.

[74] Kensaku Sakamoto, Akiko Hayashi, Ayako Sakamoto, Daisuke Kiga, Hiroshi Nakayama, Akiko Soma, Takatsugu Kobayashi, Makoto Kitabatake, Koji Takio, Kazuki Saito, Mikako Shirouzu, Ichiro Hirao, and Shigeyuki Yokoyama. Site-specific incorporation of an unnatural amino acid into proteins in mammalian cells. *Nucleic acids research*, 30(21):4692–9, 2002.

[75] Amy Grunbeck, Thomas Huber, Pallavi Sachdev, and Thomas P. Sakmar. Mapping the ligand-binding site on a G protein-coupled receptor (GPCR) using genetically encoded photocrosslinkers. *Biochemistry*, 50(17):3411–3413, 2011.

[76] Moon Hyeong Seo, Jieun Han, Zongwen Jin, Dong Won Lee, Hee Sung Park, and Hak Sung Kim. Controlled and oriented immobilization of protein by site-specific incorporation of unnatural amino acid. *Analytical Chemistry*, 83(8):2841–2845, 2011.

[77] M Hegner and H Guntherodt. Nanometer Scale Science and Technology-The impact of STM and AFM. *Nanometer Scale Science and Technology*, pages 1–20, 2001.

[78] Agostino Migliore, Stefano Corni, Rosa Di Felice, and Elisa Molinari. Water effects on electron transfer in azurin dimers. *The journal of physical chemistry. B*, 110(47):23796–23800, 2006.

[79] Agostino Migliore, Stefano Corni, Rosa Di Felice, and Elisa Molinari. Water-mediated electron transfer between protein redox centers. *Journal of Physical Chemistry B*, 111(14):3774–3781, 2007.

[80] Abraham Nitzan. and M Olecular I Nterfaces. *Annu. Rev. Phys. Chem.*, 52:681–750, 2001.

[81] P. P. Pompa, R. Chiuri, L. Manna, T. Pellegrino, L. L. Del Mercato, W. J. Parak, F. Calabi, R. Cingolani, and R. Rinaldi. Fluorescence resonance energy transfer induced by conjugation of metalloproteins to nanoparticles. *Chemical Physics Letters*, 417(4-6):351–357, 2006.

[82] Moon Bong Song, Jai M. Jang, and Chi W. Lee. Electron tunneling and electrochemical currents through interfacial water inside an STM junction. *Bulletin of the Korean Chemical Society*, 23(1):71–74, 2002.

[83] S H Pan, E W Hudson, J C Davis, and a Stm. He refrigerator based very low temperature scanning tunneling microscope. 70(2), 2001.

[84] G Binnig and H. Rohrer. Scanning tunneling microscopy. *Surface Science*, 126(126):236–244, 1982.

[85] G Binnig, C F Quate, and Ch. Gerber. Atomic force microscope. *Physical Review Letters*, 56(9):930–933, 1986.

[86] Rebecca Howland and Lisa Benatar. A Practical Guide To Scanning Probe Microscopy. page 87, 1996.

[87] Atomic Force Microscopy and Georg Fantner. Atomic Force Microscopy. pages 1–34.

[88] A K Geim and K S Novoselov. The rise of graphene. *Nature Materials*, 6(3):183–191, 2007.

[89] C. N R Rao, a. K. Sood, K. S. Subrahmanyam, and a. Govindaraj. Graphene: The new two-dimensional nanomaterial. *Angewandte Chemie - International Edition*, 48:7752–7777, 2009.

[90] A K Geim. Graphene : Status and Prospects. 324(June):1530–1534, 2009.

[91] Zhen Wah Tan, Jian-Sheng Wang, and Chee Kwan Gan. First-principles study of heat transport properties of graphene nanoribbons. *Nano letters*, 11(1):214–9, jan 2011.

[92] K S Novoselov, D Jiang, F Schedin, T J Booth, V V Khotkevich, S V Morozov, and a K Geim. Two-dimensional atomic crystals. *Proceedings of the National Academy of Sciences of the United States of America*, 102(30):10451–10453, 2005.

[93] PH Tan, WP Han, WJ Zhao, and ZH Wu. The shear mode of multilayer graphene. *Nature materials*, 11(4):294–300, 2012.

[94] Fazel Yavari and Nikhil Koratkar. Graphene-Based Chemical Sensors. *J.Phys. Chem. Lett.*, 3:1746–1753, 2012.

[95] Thomas Mueller, Fengnian Xia, and Phaedon Avouris. Graphene photodetectors for high-speed optical communications. *Nature Photonics*, 4(5):297–301, 2010.

[96] Jingquan Liu, Rui Wang, Liang Cui, Jianguo Tang, Zhen Liu, Qingshan Kong, Wenrong Yang, and Justin Gooding. Using Molecular Level Modification To Tune the Conductivity of Graphene Papers. 2012.

[97] Vamsi K. Kodali, Jan Scrimgeour, Suenne Kim, John H. Hankinson, Keith M. Carroll, Walt a. De Heer, Claire Berger, and Jennifer E. Curtis. Nonperturbative chemical modification of graphene for protein micropatterning. *Langmuir*, 27(13):863–865, 2011.

[98] Xiaohong An, Thomas W Butler, Morris Washington, Saroj K Nayak, and Swastik Kar. Optical and Sensing Properties of 1-Pyrenecarboxylic Acid-Functionalised Graphene Films Laminated on Polydimethylsiloxane Membranes. *ACS Nano*, 5(2):1003–1011, 2011.

[99] Xinran Wang, Scott Tabakman, and Hongjie Dai. Atomic Layer Deposition of Metal Oxides on Pristine and Functionalized Graphene. (Figure 3):8152–8153, 2008.

[100] Samuel C. Reddington, Eric Michael Tippmann, and Darran Dafydd Jones. Residue choice defines efficiency and influence of bioorthogonal protein modification via genetically encoded strain promoted Click chemistry. pages 1–3, 2012.

[101] Taiji Furuno. Embedding and immobilizing protein molecules into two-dimensional protein arrays for single-molecule imaging by tapping mode atomic force microscopy. *Japanese Journal of Applied Physics, Part 1: Regular Papers and Short Notes and Review Papers*, 39(11):6435–6440, 2000.

[102] D. Xu. Atomic Force Microscope Conductivity Measurements of Single Ferritin Molecules. *Dissertation for Doctor of Philosophy, Brigham Young University*, (October), 2004.

[103] Y C Guo, X F Zhou, J L Sun, M Q Li, and J Hu. Height measurement of DNA molecules with lift mode AFM. *Chinese Science Bulletin*, 49(15):1574–1577, 2004.

[104] Umberto Prisco, Carl Leung, Chrisa Xirouchaki, Celine H Jones, John K Heath, and Richard E Palmer. Residue-specific immobilization of protein molecules by size-selected clusters. *Journal of the Royal Society, Interface / the Royal Society*, 2(3):169–75, 2005.

[105] N. Lidgi-Guigui, C. Leung, and R.E. Palmer. Weak precursor state binding of protein molecules to size-selected gold nanoclusters on surfaces. *Surface Science*, 602(4):1006–1009, 2008.

[106] Na Kong, J Justin Gooding, and Jingquan Liu. Protein sensors based on reversible $\pi\pi$ stacking on basal plane HOPG electrodes. *Journal of Solid State Electrochemistry*, 18:3379–3386, 2014.

[107] Yuyan Shao, Jun Wang, Hong Wu, Jun Liu, Ilhan A. Aksay, and Yuehe Lin. Graphene based electrochemical sensors and biosensors: A review. *Electroanalysis*, 22(10):1027–1036, 2010.

[108] Yongki Choi. Single-Molecule Lysozyme Dynamics. *Science*, 319(January):319–325, 2012.

[109] Patrick C. Sims, Issa S. Moody, Yongki Choi, Chengjun Dong, Mariam Iftikhar, Brad L. Corso, O. Tolga Gul, Philip G. Collins, and Gregory A. Weiss. Electronic measurements of single-molecule catalysis by cAMP-dependent protein kinase A. *Journal of the American Chemical Society*, 135(21):7861–7868, 2013.

[110] R Hawaldar, P Merino, M R Correia, I Bdikin, J Gracio, J Mendez, J a Martin-Gago, and M K Singh. Large-area high-throughput synthesis of monolayer graphene sheet by Hot Filament Thermal Chemical Vapor Deposition. *Scientific Reports*, 2:682, 2012.

[111] Li Li Zhang, Xin Zhao, Hengxing Ji, Meryl D. Stoller, Linfei Lai, Shanthi Murali, Stephen Mcdonnell, Brandon Cleveger, Robert M. Wallace, and Rodney S. Ruoff. Nitrogen doping of graphene and its effect on quantum capacitance, and a new insight on the enhanced capacitance of N-doped carbon. *Energy and Environmental Science*, 5(11):9618, 2012.

[112] Teresa Oh. CVD graphene synthesis on copper foils and doping effect by nitric acid. *Transactions on Electrical and Electronic Materials*, 14(5):246–249, 2013.

[113] Ganjigunte R S Iyer, Jian Wang, Garth Wells, Michael P Bradley, and Ferenc Borondics. Nanoscale imaging of freestanding nitrogen doped single layer graphene. *Nanoscale*, 7:2289–2294, 2015.

[114] Jiacheng Wang, Ruguang Ma, Zhenzhen Zhou, Guanghui Liu, and Qian Liu. Magnesiothermic synthesis of sulfur-doped graphene as an efficient metal-free electrocatalyst for oxygen reduction. *Scientific reports*, 5:9304, 2015.

[115] C. Casiraghi. Doping dependence of the Raman peaks intensity of graphene close to the Dirac point. *Physical Review B - Condensed Matter and Materials Physics*, 80(23):2–4, 2009.

[116] Sandip Niyogi, Elena Bekyarova, Mikhail E Itkis, Hang Zhang, J Hicks, Mike Sprinkle, Claire Berger, Chun Ning Lau, Walt A De, Sandip Niyogi, Elena Bekyarova, Mikhail E Itkis, Hang Zhang, and Kristin Shepperd. To cite this version : Spectroscopy of Covalently Functionalized Graphene. 2014.

[117] Andrea C. Ferrari. Raman spectroscopy of graphene and graphite: Disorder, electron-phonon coupling, doping and nonadiabatic effects. *Solid State Communications*, 143(1-2):47–57, 2007.

[118] Ruitao Lv, Qing Li, Andrés R. Botello-Méndez, Takuya Hayashi, Bei Wang, Ayse Berkdemir, Qingzhen Hao, Ana Laura Elías, Rodolfo Cruz-Silva, Humberto R. Gutiérrez, Yoong Ahm Kim, Hiroyuki Muramatsu, Jun Zhu, Morinobu Endo, Humberto Terrones, Jean-Christophe Charlier, Minghu Pan, and Mauricio Terrones. Nitrogen-doped graphene: beyond single substitution and enhanced molecular sensing. *Scientific Reports*, 2:1–8, 2012.

[119] Rakesh Voggu, Barun Das, Chandra Sekhar Rout, and C. N. R. Rao. Effects of interaction of electron donor and accepter molecules on the electronic structure of graphene. page 11, 2008.

[120] S Tongay, K Berke, M Lemaitre, Z Nasrollahi, D B Tanner, a F Hebard, and B R Appleton. Stable hole doping of graphene for low electrical resistance and high optical transparency. *Nanotechnology*, 22:425701, 2011.

[121] M B Klarskov, H F Dam, D H Petersen, T M Hansen, a Löwenborg, T J Booth, M S Schmidt, R Lin, P F Nielsen, and P Bøggild. Fast and direct

measurements of the electrical properties of graphene using micro four-point probes. *Nanotechnology*, 22(44):445702, 2011.

[122] Satoru Ichinokura, Katsuaki Sugawara, Akari Takayama, Takashi Takahashi, and Shuji Hasegawa. Superconducting Calcium-Intercalated Bilayer Graphene. *ACS Nano*, 10(2):2761–2765, 2016.

[123] Iddo Heller, Sohail Chatoor, Jaan Männik, Marcel A G Zevenbergen, Cees Dekker, and Serge G. Lemay. Influence of electrolyte composition on liquid-gated carbon nanotube and graphene transistors. *Journal of the American Chemical Society*, 132(48):17149–17156, 2010.

[124] R. R. Nair, P. Blake, a. N. Grigorenko, K. S. Novoselov, T. J. Booth, T. Stauber, N. M. R. Peres, and a. K. Geim. Fine Structure Constant Defines Visual Transperency of Graphene. *Science*, 320(June):2008, 2008.

[125] Alexey M. Bogdanov, Alexander S. Mishin, Ilia V. Yampolsky, Vsevolod V. Belousov, Dmitriy M. Chudakov, Fedor V. Subach, Vladislav V. Verkhusha, Sergey Lukyanov, and Konstantin A. Lukyanov. Green fluorescent proteins are light-induced electron donors. *Nat. Chem. Biol.*, 5(7):459–461, 2010.

[126] Samuel C Reddington, Eric M Tippmann, and D Dafydd Jones. Residue choice defines efficiency and influence of bioorthogonal protein modification via genetically encoded strain promoted Click chemistry. *Chemical communications (Cambridge, England)*, 48(67):8419–21, 2012.

[127] S. Antoranz Contera, H. Iwasaki, and S. Suzuki. Ambient STM and in situ AFM study of nitrite reductase proteins adsorbed on gold and graphite: Influence of the substrate on protein interactions. *Ultramicroscopy*, 97(1-4):65–72, 2003.

[128] Zhihai Li, Manuel Smeu, Mark a. Ratner, and Eric Borguet. Effect of anchoring groups on single molecule charge transport through porphyrins. *Journal of Physical Chemistry C*, 117:14890–14898, 2013.

[129] Nadav Amdursky, Doron Ferber, Israel Pecht, Mordechai Sheves, and David Cahen. Redox activity distinguishes solid-state electron transport from solution-based electron transfer in a natural and artificial protein: cytochrome C and hemin-doped human serum albumin. *Physical chemistry chemical physics : PCCP*, 15(40):17142–9, 2013.

[130] C J Forman, N Wang, Z Y Yang, C G Mowat, S Jarvis, C Durkan, and P D Barker. Probing the location of displayed cytochrome b562 on amyloid by scanning tunnelling microscopy. *Nanotechnology*, 24:175102, 2013.

[131] Samuele Raccosta, Chiara Baldacchini, Anna Rita Bizzarri, and Salvatore Cannistraro. Conductive atomic force microscopy study of single molecule electron transport through the Azurin-gold nanoparticle system. *Applied Physics Letters*, 102(20), 2013.

[132] Sonia Antoranz Contera and Hiroshi Iwasaki. Imaging the proteins pseudoazurin and apo-pseudoazurin on gold by STM in air: Effect of the bias voltage. *Ultramicroscopy*, 91(1-4):231–243, 2002.

[133] Wolfgang Haiss, Harm Van Zalinge, Simon J Higgins, Donald Bethell, Horst Höbenreich, David J Schiffrin, and Richard J Nichols. Redox state dependence of single molecule conductivity. *Journal of the American Chemical Society*, 125(50):15294–5, 2003.

[134] Jason J Davis and H Allen O Hill. The scanning probe microscopy of metalloproteins and metalloenzymes. *Chemical communications (Cambridge, England)*, (5):393–401, 2002.

[135] Wolfgang Haiss, Richard J Nichols, Harm Van Zalinge, Simon J Higgins, Donald Bethell, and David J Schiffrin. formation of molecular wires. 2004.

[136] Xiaoyin Xiao, Bingqian Xu, and Nongjian Tao. Conductance Titration of Single-Peptide Molecules. *Journal of the American Chemical Society*, 126(17):5370–5371, 2004.

[137] Bingqian Xu, Xiaoyin Xiao, and Nongjian J. Tao. Measurements of Single-Molecule Electromechanical Properties. *Journal of the American Chemical Society*, 125(52):16164–16165, 2003.

[138] Megan L. Jones, Igor V. Kurnikov, and David N. Beratan. The nature of tunneling pathway and average packing density models for protein-mediated electron transfer. *Journal of Physical Chemistry A*, 106(10):2002–2006, 2002.

[139] Wolfgang Haiss, Changsheng Wang, Iain Grace, Andrei S Batsanov, David J Schiffrin, Simon J Higgins, Martin R Bryce, Colin J Lambert, and Richard J Nichols. Precision control of single-molecule electrical junctions. 5(December):995–1002, 2006.

[140] Lior Sepunaru, Sivan Refaely-Abramson, Robert Lovrin??i??, Yulian Gavrilov, Piyush Agrawal, Yaakov Levy, Leeor Kronik, Israel Pecht, Mordechai Sheves, and David Cahen. Electronic transport via homopeptides: The role of side chains and secondary structure. *Journal of the American Chemical Society*, 137(30):9617–9626, 2015.

[141] Xiaoyin Xiao, Bingqian Xu, and Nongjian Tao. Changes in the conductance of single peptide molecules upon metal-ion binding. *Angewandte Chemie - International Edition*, 43(45):6148–6152, 2004.

[142] Sonia Antoranz Contera, Toshihide Okajima, and Hiroshi Iwasaki. Scanning tunnelling microscopy images of the copper-containing amine oxidase from arthrobacter globiformis in the holo and apo forms adsorbed on gold under ambient conditions. *Japanese Journal of Applied Physics, Part 1: Regular Papers and Short Notes and Review Papers*, 41(6 A):3916–3921, 2002.

[143] Danny N Axford and Jason J Davis. Electron flux through apo-and holoferritin. *Nanotechnology*, 18(14):145502, 2007.

[144] Marie-Claire Parker, Martyn C. Davies, and Saul J. B. Tendler. Effect of Controlled Hydration on Scanning Tunneling Microscopy Images of Covalently Immobilized Proteins. *The Journal of Physical Chemistry*, 99(43):16155–16161, 1995.

[145] Graham J Leggett, Martyn C Davies, David E Jackson, Clive J Roberts, Saul J B Tendler, and Philip M Williams. Studies of Covalently Immobilized Protein Molecules by Scanning Tunneling Microscopy : The Role of Water in Image Contrast Formation. *Langmuir*, pages 8852–8854, 2000.

[146] E. Leary, H. Höbenreich, S. J. Higgins, H. Van Zalinge, W. Haiss, R. J. Nichols, C. M. Finch, I. Grace, C. J. Lambert, R. McGrath, and J. Smerdon. Single-molecule solvation-shell sensing. *Physical Review Letters*, 102(8):1–4, 2009.

[147] Ellis Pires. Electrical Conductivity of Single Organic Molecules in Ultra High Vacuum. (September):1–132, 2013.

[148] Andrea Vezzoli, Iain Mark Grace, Carly Brooke, Kun Wang, Colin Lambert, Bingqian Xu, Richard J. Nichols, and Simon Higgins. Gating of single molecule junction conductance by charge transfer complex formation. *Nanoscale*, pages 18949–18955, 2015.

[149] Amaresh Mishra, Chang Qi Ma, and Peter Bäuerle. Functional oligothiophenes: Molecular design for multidimensional nanoarchitectures and their applications. *Chemical Reviews*, 109(3):1141–1176, 2009.

[150] Wolfgang Haiss, Richard J Nichols, Harm Van Zalinge, Simon J Higgins, Donald Bethell, and David J Schiffrin. Formation of Molecular Wires. 2004.

[151] Andrea Vezzoli. *Environmental Effects in Molecular Electronics*. University of Liverpool, 2015.

[152] Elke Scheer. *Molecular electronics: an introduction to theory and experiment*, volume 1. World Scientific, 2010.

[153] B Giese, J Amaudrut, a K Köhler, M Spormann, and S Wessely. Direct observation of hole transfer through DNA by hopping between adenine bases and by tunnelling. *Nature*, 412(6844):318–320, 2001.

[154] Ryo Yamada, Hiroaki Kumazawa, Shoji Tanaka, and Hirokazu Tada. Electrical resistance of long oligothiophene molecules. *Applied Physics Express*, 2(2), 2009.

[155] See Kei Lee, Ryo Yamada, Shoji Tanaka, Gap Soo Chang, Yoshihiro Asai, and Hirokazu Tada. Universal temperature crossover behavior of electrical conductance in a single oligothiophene molecular wire. *ACS Nano*, 6(6):5078–5082, 2012.

[156] Anand Kumar Tatikonda, Maria Tkachev, and Ron Naaman. A highly sensitive hybrid organic-inorganic sensor for continuous monitoring of hemoglobin. *Biosensors and Bioelectronics*, 45(1):201–205, 2013.

[157] Peter Agbo, James R. Heath, and Harry B. Gray. Catalysis of dioxygen reduction by thermus thermophilus strain hb27 laccase on ketjen black electrodes. *Journal of Physical Chemistry B*, 117(2):527–534, 2013.

[158] Rafael Furlan De Oliveira, Leandro Merces, Tatiana Parra Vello, and Carlos César Bof Bufon. Water-gated phthalocyanine transistors: Operation and transduction of the peptide-enzyme interaction. *Organic Electronics: physics, materials, applications*, 31:217–226, 2016.